CFD Modeling of Cavitation for Fine Particle Flotation

by

Seyed Shaham Aldin Hosseininejad

A thesis submitted in partial fulfillment of the requirements for the degree of

Doctor of Philosophy

in

Chemical Engineering

Department of Chemical and Materials Engineering

University of Alberta

Abstract

To overcome the challenges of low recovery of fine particles in flotation processes, designing a cavitating device that can enhance the recovery has been a major topic of study. In the design of a cavitating device, the bubble/bubble interactions, bubble response to the change of local pressure, and the effect of dissolved gas in the liquid are the points of interest.

In this study, CFD is used to develop cavitation models that include the physical models related to these phenomena. From existing cavitation models, Singhal cavitation model is the only model that accounts for the effect of non-condensable gasses in the flow regime without including the bubble/bubble interactions. In this study, furthermore to the Singhal model being used to study the cavitation inception, two Lagrangian and Eulerian approaches for modeling of the bubbly flow are implemented in Ansys-Fluent to measure the bubble size distribution. The Eulerian method (PBM) implements a population balance equation to study the changes of bubble size distribution due to pressure, coalescence, breakage, gas diffusion and nucleation. The Lagrangian method (DBM) implements discrete particle tracking method to track each bubble individually, with the bubble dynamics, bubble coalescence/breakage, and gas diffusion models being implemented in three-way coupling.

For verification, each implemented model is, separately, compared to the experimental results from literature. Some challenges in the procedure of model development are investigated and solutions are found to the model application process. Then, the two developed models, with the Singhal cavitation model, are compared to the in-house experimental results of cavitation inception and the bubble size distribution in a venturi tube. Acceptable agreement between the modeling and the experimental results is observed. Finally, the Population Balance Model (PBM) and Discrete Bubble Model (DBM) are implemented in a case study of investigating the best location of the air injection into the studied venturi. The objective is to maximize the collection of upstream nuclei by the bubble injected in the middle of the flow in the venturi.

Acknowledgements

I like to take this opportunity to thank my supervisors, my friends and family who have helped me during my PhD studies at University of Alberta.

First, I would like to express my sincere gratitude to my supervisor, Dr. Robert E. Hayes, who has supported me throughout my research with his patience and knowledge. His guidance has been a tremendous help during my research and writing of the thesis.

I would also like to appreciate the help of Dr. Zhenghe Xu and Dr. Chad Liu for their immerse help in advising the right direction of the project and giving new research ideas.

I would like to thank Artin Afacan and Dr. Sean Sanders for their technical support during my experiments. My appreciation also goes to Kiana Hajebi, Fariborz Kiasi, Morteza Ghadirian and Roohi Shokri for their help and support during my research.

I would like to acknowledge the Canadian Center for Clean Coal/Carbon and Mineral Processing Technologies (C_5MPT) and Natural Science and Engineering Research Council of Canada (NSERC) and Collaborative Research and Development (CRD) co-sponsors for their financial support.

Finally, I would like to thank my family for their never-ending love, support and encouragement along the way.

Table of Contents

List of Figures

List of Tables

List of Abbreviation

ASW	Air Saturated Water
CFD	Computational Fluid Dynamics
CSW	CO_2 Saturated Water
DAF	Dissolved Air Flotation
DBG	Dual Bubble Generator
DBM	Discrete Bubble Model
DGW	DeGassed Water
FBRM	Focused Beam Reflectance Measurement
HIA	High Intensity Agitation
IAC	Interfacial Area Concentration
K-M	Keller-Miksis
NCG	Non-Condensable Gases
PBM	Population Balance Model
P-Z	Plesset-Zwick
R-P	Rayleigh-Plesset
SMD	Sauter Mean Diameter
TOL	Tolerance

Chapter 1

Introduction

1.1. Motivation

Many industrial processes, especially in the mining industry, use flotation to recover particulate matter. Flotation is a primary purification process in which bubbles of air are attached to solids or a secondary phase. This attachment causes the intended material to float in a counter current of sludge going down based on the difference of densities. The particles accumulated on top are called froth and can be collected for the next purification step. Flotation has been used for almost a century in wastewater treatment, the mining industry for purification of coal and precious metals, and in the oil sands industry.

The flotation process can be used to recover a wide range of particle sizes. Commonly, in the mineral industry, the ore is ground into hundred micron size (100-600 μm) particles to liberate valuable materials. As shown in Figure 1.1, the applicable range for particle size in the conventional flotation process to reach a high recovery is nominally 10-100 μm for three metals of copper, lead and zinc (Trahar and Warren, 1976). For coarser size particles, the recovery drops off as the particle size increases because the floating of heavier particles by air is harder. On the other hand, for fine particles, the reason of low recovery can be related to the low probability of particle/bubble collision.

In general, the flotation recovery depends on the bubble/particle collision, attachment and detachment. Yoon (1993) expressed the total collection probability as

$$P_{tot} = P_{col} P_{att} \left(1 - P_{det}\right) \tag{1.1}$$

where P_{col} is the bubble/particle collision probability, P_{att} is the bubble/particle attachment probability, P_{det} is the bubble/particle detachment probability. This equation shows that the flotation recovery is directly proportional to the bubble/particle collision and attachment probabilities, and inversely proportional to the bubble/particle detachment probability.

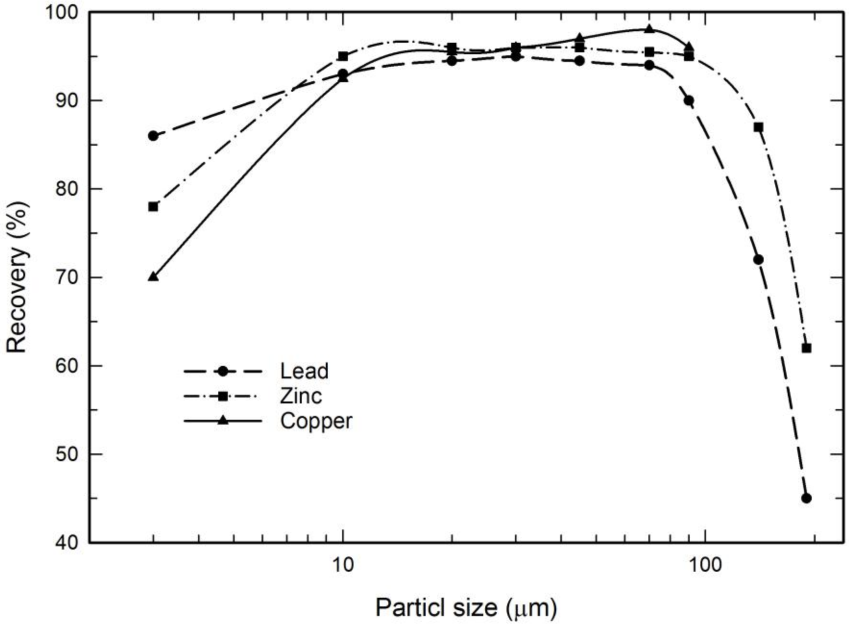

Figure 1.1 Flotation recovery versus the particle size (Trahar and Warren, 1976)

The collision efficiency of a rising bubble and falling particle can be predicted using a model developed by Weber and Paddock (1983) as

$$P_{col} = \frac{3}{2}\left(\frac{D_p}{D_b}\right)^2 \left[1 + \frac{(3/16)Re}{1 + 0.249Re^{0.56}}\right]; 0 < Re \leq 300 \tag{1.2}$$

D_p and D_b are particle and bubble diameters respectively, and Re is the Reynolds number of the bubble, defined as

$$Re = \frac{\rho_l u_{ter} D_b}{\mu_l} \tag{1.3}$$

u_{ter} is bubble terminal velocity, ρ_l and μ_l are the liquid density and viscosity.

Li (2014) plotted the collision probability versus the bubble diameter for three particle sizes i.e. 10, 50, 100 μm using the terminal rising bubble velocity proposed by Jamialahmadi et al. (1994). The graph, shown in Figure 1.2, illustrates the sharp decrease in collision probability as the particle diameter decreases. Moreover, it shows that to have higher collision probabilities the bubble radius should be smaller than 100 μm. However, the bubble size used in conventional flotation is around 500 μm (Ahmed and Jameson 1985). Therefore, low probability of bubble/particle collision is the main challenge in conventional flotation, beside other challenges such as high chemical consumption, rapid oxidation, etc. (Yoon and Luttrell, 1986; Subrahmanyan and Forsberg, 1990)

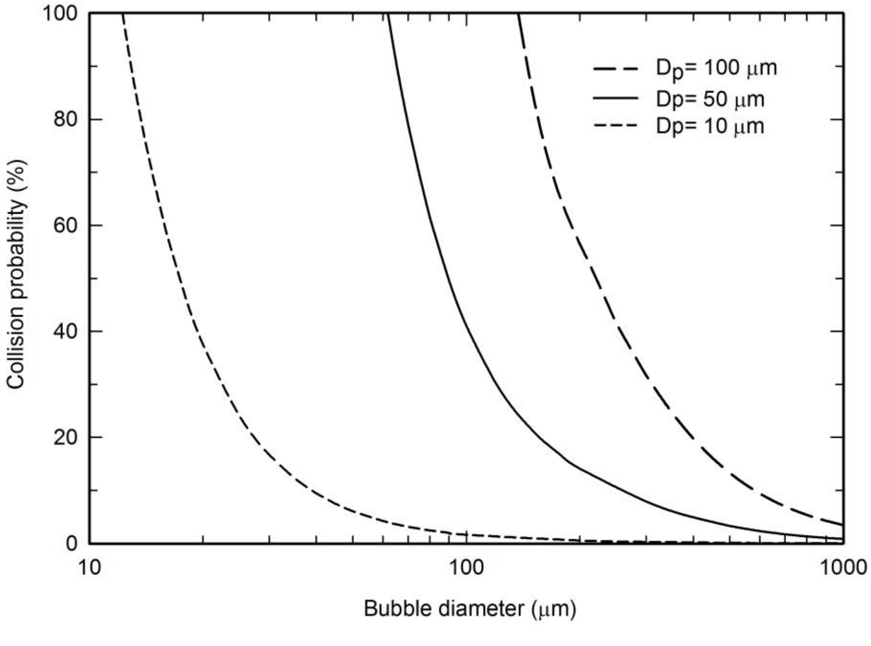

Figure 1.2 Bubble/particle collision probability function (Equation 1.2) for various bubble and particle diameters (Li, 2014).

Many studies have been conducted to enhance fine particle recovery in flotation by introducing micron size bubbles in the flotation cell to increase the possibility of particle-bubble attachment (Trahar and Warren, 1976; Miettinen et al. 2010). For example, high intensity dissipation systems have shown some promising experimental results for fine particle flotation (Warren, 1975; Finch and Hardie, 1999; Singh et al., 1997). Zhou et al. (1997) showed that by passing the feed pulp through a cavitation tube before the flotation process can improve the flotation of fine particles. Zou et al. (1997) stated that the improved flocculation is caused by in-situ bubble nucleation by hydrodynamic cavitation on the hydrophobic particles. He explained that the existence of the micron size bubbles on the surface of a solid can increase the effective contact angle of the surface as shown in Figure 1.3.

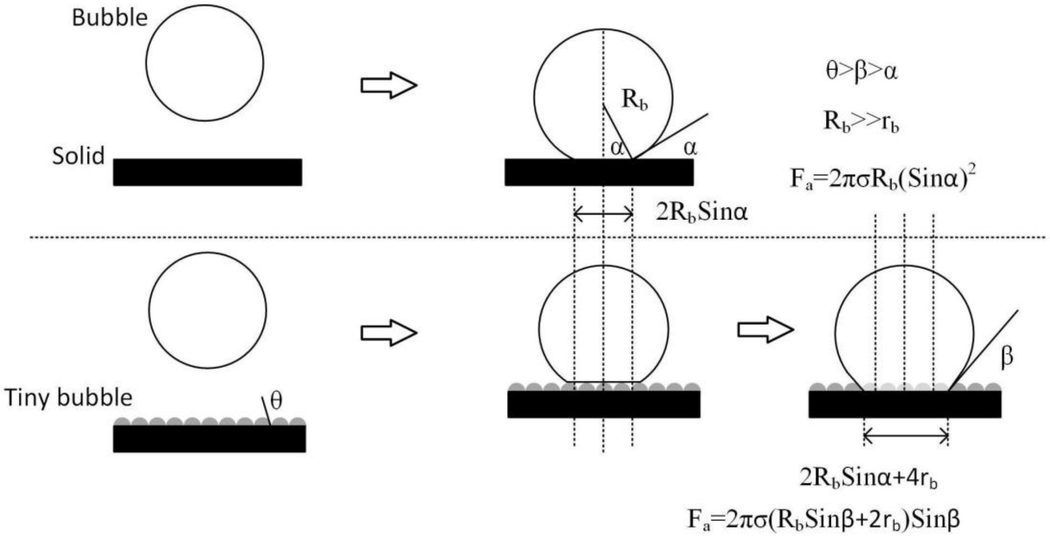

Figure 1.3 Role of tiny bubbles in enlarging contact angle (Zhou 2009)

Many studies have proposed different methods for producing micron size bubbles such as electrolysis, ultrasonic oscillation, and hydrodynamic cavitation. Producing a large amount of bubbles is challenging using ultrasonic and electrolysis methods. On the other hand, hydrodynamic cavitation has been implemented for extensive micron size bubble production in a few pilot plant and lab scale setups (Eriez, 2014; Tao et al., 2008). In both cases, using the cavitation for producing micron size bubbles enhances the recovery by 10-20 %.

The procedure of bubble production includes pumping a portion of the tailing through a venturi style cavitation tube. In this study, the mass exchange between the liquid and gas phase due to the pressure drop in liquid is called cavitation. However, it is more accurate to be called flashing or evaporation. The pressure drop can be achieved by increasing the liquid velocity, pressure oscillation by ultrasound waves, inside a vortex, etc. In a venturi, according to the momentum conservation and Bernoulli equation, by decreasing the cross section area and increasing the average velocity, the pressure decreases. The cavitation occurs when the pressure is below a certain threshold, depending on the properties of the liquid. Further studies about the cavitation are discussed in the following chapter.

1.2. Problem statement

To design a device to enhance the fine particle flotation using cavitation, a deep understanding of cavitation is required. Cavitation has been the subject of studies for over a century; however, cavitation physics is still not completely understood. The phenomenon involves a multiphase problem of mass exchange between liquid and gas phases, with mass, momentum, and heat transfer involved at a wide range of time and length scales. Because of the variety of possible cavitation inceptions and uncertainties, developing a model that predict all features of cavitation has been impossible so far. Many researchers have studied different forms of the cavitation. Developing a Computation Fluid Dynamics (CFD) model for the cavitation is a challenging problem that has been studied for more than a decade by many researchers.

1.3. Objectives

The main objective of this study was to develop a CFD model to investigate the cavitation inception and predict the bubble size distribution produced by cavitation in a venturi. Because of the complexity, in this project, we study two phase flow, and the three phase flow (including the effect of particles) was left for future studies. The bubble/particle interactions are neglected in this study, with the assumption that the nucleation site of cavitation exists on the surface of the particle, and the growth of this bubble is not affected by the existence of the particle. Therefore, different models of cavitation, bubble dynamic, bubble/bubble interaction, and bubble nucleation models are investigated, and implemented in a CFD model. Two approaches, Eulerian and Lagrangian, were implemented for modeling for cavitation and bubble size distribution. Then, the major challenges of the models were introduced and solutions to overcome those challenges were proposed. The results of the modeling were compared with literature data for each model for verification of the correct implementation, and were compared to the experimental results from in-house setup for the full model to compare the overall performance of the model. Then, the CFD model was implemented in a case study in Dual Bubble Generator (DBG), to demonstrate the capability of the developed model in design optimization of a DBG. This study is a primary step to our ultimate goal which is to develop a system that is optimized to enhance the attachment of fine particles to bigger flotation bubbles.

1.4. Thesis outline

The remainder of the thesis is organized as follows:

Chapter 2 presents an introduction and literature review on froth flotation and fine particle flotation and the role of cavitation in enhancing fine particle recovery. Then, a short introduction to cavitation and bubble behavior is presented.

Chapter 3 includes the experimental setup and the methods of measuring the bubble size distribution in a cavitated flow based on the variation of the flowrate and gas content. These measurements are implemented for verification of the developed cavitation models. The approaches implemented to measure BSD on a lab scale setup will be explained and discussed.

Chapter 4 provides details on the development of CFD model for cavitation inception prediction, and cavitated bubbly flow. Three models are introduced which include, the Singhal cavitation model for predicting cavitation inception and vapor volume fraction; Population Balance Model (PBM) for predicting cavitation inception, vapor volume fraction and Bubble Size Distribution (BSD); Discrete Bubble Model (DBM) which can track the flow of bubbles in a bubbly flow in detail. First two models, Singhal model and PBM, use Eulerian approach, and DBM uses Lagrangian approach for the bubble phase

Chapter 5 consists of two parts. First, the models that have been implemented in PBM or DBM model are individually validated with the available numerical or experimental data from the literatures. The challenges of these models, and the solution to these challenges are discussed. Then, the cavitation models explained in Chapter 4 are implemented for different experimental cases from Chapter 2. Finally, a case study of using the cavitation models in optimizing the design of DBG is shown as example.

Chapter 6 includes the summary, conclusion and future work for this study.

Chapter 2

Background and Literature Review

In this chapter, the process of flotation and challenges related to fine particle flotation are reviewed. Then, different approaches to overcome the challenge and the role of cavitation in fine particle flotation are discussed. Finally, cavitation and bubble dynamics are introduced which is a preface to the next chapter of cavitation modeling

2.1. History of froth flotation

The first concept of using the differences in surface properties for mineral separation was patented by William Haynes in 1860. In this process, the powders of sulfides were agglomerated by oil, and other minerals could be removed by washing. The first commercial flotation plant was built in 1877 to clean graphite ore and, in 1898, Francis Elmore used oil agglomeration for separating sulfides from gangue particles which is regarded as the first successful process for floating sulfides, although it was not similar to contemporary froth flotation (Fuerstenau et al, 2007).

In 1901, there was a problem on how to extract zinc from dumps at Broken Hill. Lead, silver, and zinc was dumped through the tailing. Bulk flotation was a process that revived the mine and restored prosperity, where by 1913, ten years after the start of investigation, 3 Mt of zinc concentrate was produced. Further studies resulted in approaches that changed the inflexible bulk flotation into an extraction process for individual minerals, e.g. adding some chemicals to activate or depress minerals in the flotation process. Flotation started in Canada in 1917 at the Sullican mine of the consolidated mining and smelting company (Fuerstenau et al, 2007).

In 1925, the subaeration cells were available for flotation processes. After a lag of research on flotation during World War II, three types of flotation cells were developed during the second half of the 20th century. In low-intensity cells the feed enters the cell at the collection zone at the top of the column. It flows downward, and contacts the air bubbles introduced to the column at the bottom, by a sparger. In medium-intensity cells or mechanically agitated flotation machines, a rotating mechanism is used to keep solids in suspension, and air bubbles are applied to the system by shearing under pressure. This mechanism increases the flotation rate by 1.2 to 1.5 times. High-intensity flotation consists of an external aeration mechanism where feed pulp is in intense contact with fine bubbles. This mechanism commonly uses either pressurized air or air entrained into a fluid jet. High-intensity flotation increases the flotation rate by 2-4 times (Fuerstenau et al, 2007).

2.2. Fine particle flotation

Fine particle flotation is defined as recovery of particles smaller than 10 μm in flotation process (Tao et al. 2010). As discussed in Chapter 1, the low possibility of bubble/particle collision is responsible for fine particles recovery. Some studies have been conducted to enhance fine particle recovery in flotation by increasing the possibility of particle-bubble attachment through two approaches, increasing particle sizes by aggregation or decreasing the bubble size (Trahar and Warren, 1976; Miettinen et al. 2010). These methods rely on three approaches, adding non-polar oil or chemical as flocculent in hydrophobic flotation, using high shear in flotation, and using gas nucleation.

In flocculation flotation, a non-polar oil i.e. kerosene, diesel, etc. or other chemical is added to the flotation cell to enhance the flocculation of hydrophobic particles (Song et al., 1999). In high shear flotation the aggregation of hydrophobic particles is achieved by using intensive agitation to increase the fine particles collision (Warren, 1975; Finch and Hardie, 1999; Singh et al., 1997). For higher particle recovery, the two former methods are integrated in shear flocculation flotation (Song et al., 2001). However, high dosage of flocculent and high energy input are the main barriers of economical usage of these methods for fine particle recovery.

Dissolved Air Flotation (DAF) uses the third approach to enhance the fine particle flotation. In DAF, the dissolved gas concentration is increased by injecting air at pressurized feed; then, the feed is depressurized to ambient pressure, causing the formation of gas nucleates on the surface of hydrophobic particles through the diffusion of gas to the pre-existing picobubbles on the particle (Rodrigues and Rubio, 2007; Tao, 2005). In this method, the existence of microbubbles (<100 μm) alongside the midsize and bigger bubbles enhance the fine particle recovery, as discussed previously. A problem with dissolved air flotation, at least where mineral processing is concerned, is that the volume of gas produced is far lower than with mechanical systems (Miettinen et al., 2010).

Using hydrodynamic cavitation, to nucleate micro bubbles, is a similar approach to DAF. In this method, the slurry of fine particles is passed through a cavitation tube, i.e. a contraction or venturi tube. The pressure drop in the cavitation tube causes the pre-existing or new cavities to form. Zhou et al. (1997) showed that by passing the feed pulp through a cavitation tube before the flotation process can improve the flotation of fine particles. Zou et al. (1997) stated that the improved flocculation is caused by in-situ bubble nucleation by hydrodynamic cavitation on the hydrophobic particles. Sun et al. (2006) observed cavitated bubbles formation in a high intensity agitation (HIA) cell through a high speed camera. Wu et al. (2012) has shown that using a HIA cell, nano-size bubbles can be produced. These bubbles can be stable for hours using frother. The advantage of the using hydrodynamic cavitation over DAF method is that the bubble generation rate can be controlled by the shape of cavitation tube, the velocity of the liquid, the gas dissolved concentration in the slurry and the air injected into the slurry.

In summary, a major challenge for contemporary mineral industries is the loss of precious materials with fine particle sizes (less than 20 μm) through the tailing. Using hydrodynamic cavitation to produce micron size bubbles in the slurry and flotation cell can enhance this recovery by increasing the bubble/particle collision. In next section, different types of nuclei and nucleation will be introduced and the studies for the role of cavitation in fine particle flotation will be reviewed.

2.3. Hydrodynamic cavitation

Cavitation is the formation of vapor cavities in a homogeneous liquid in the regions where the pressure drops below a certain threshold, while the temperature does not change significantly (Franc and Michel, 2006). Cavitation is compared to the boiling where the nucleation occurs due to increase in vapor pressure because of the increase in the liquid temperature. Cavitation can be the result of both the diffusive evaporation of liquid into the cavity and the expansion of Non-Condensable Gases (NCG) in the cavity. Nucleation is the stage that cavities form, which needs energy due to the formation of two interfaces in the fluid. Different forms of cavities and nucleation are discussed in the next section.

There are two steps in the cavitation process, the cavitation inception i.e. nucleation of vapor cavity and the development of the cavity formation. Cavitation can form on a solid boundary or in the body of the liquid, i.e. heterogeneous and homogeneous nucleation. The vapor cavity can be travelling isolated bubble, fixed or sheet cavities, cavitating vortices i.e. vortex cavitation. Another pattern of cavity happens when an attached cavity becomes separated and transported as a travelling bubble.

The cavitation formation depends on the geometry, flow regime, physical properties of the fluids, the local roughness of the wall, etc. Partial cavitation, supercavitation, vortex cavitation, shear cavitation and ultrasonic cavitation are the typical forms of cavitation. Partial and supercavitation are the common forms of cavitation on hydrofoil, propellers of ships or pumps and in the venturi. Vortex cavitation is the typical form of cavitation that occurs at the propellers tip vortex. Shear cavitation is the form of cavitation that occurs due to the difference in velocity of two layers of liquid resulting in large turbulent pressure fluctuations such as in submerged jets, high divergence angle venturi or orifices. Ultrasonic cavitation is the result of an oscillating pressure field by an ultrasound pressure wave. A shock wave as a result of vibration or strong fluid acceleration can result a similar form of cavitation, known as water hammer.

Cavitation, in many cases, is an undesirable phenomenon. When these cavities are brought to a high pressure region the bubbles collapse where a large amount of energy is released in a short period of time. This condition causes a pressure and temperature rise up to 100-500 atm and 1000-5000 °C. This phenomenon causes a significant damage to components, noise and loss of efficiency in devises such as pumps. Thus, there are a lot of efforts to prevent the rise of this event in the equipment. However, researches are done to take advantage of this phenomenon such as accelerated hydrolysis of fatty oils and cellulose, tumor cell disruption, wastewater treatment, etc. It can also be applicable to enhance the flotation of fine particles.

In a hydraulic system liable to cavitation, a cavitation number (*CN*) is defined as shown in Eq. 2.1, to be used as a scaling parameter in cavitation phenomena.

$$CN = \frac{p_r - p_c}{\frac{1}{2}\rho u_r^2} \tag{2.1}$$

where p_r and u_r are the reference pressure and velocity and p_c is the critical pressure that cavitation occurs i.e. liquid vapor pressure in most cases. However, extrapolating the cavitation results to full scale geometry is not straightforward. Therefore, a CFD model to predict the cavitation in different geometries is needed for better prediction of the cavitating flow characteristics.

2.4. Types of nuclei and nucleation

Nucleation is the accumulation of gas molecules to form a micron size bubble i.e. nucleus. Different nuclei in the liquid are known to be the source of cavitation formation. Free gas nuclei traveling a low pressure region can expand in size and form the traveling bubble type of cavitation. In other cases, if the pressure drops below the vapor pressure, a vapor nucleus can form, which is composed mostly of liquid vapor. However, the formation and existence of these two types of nuclei are questionable, as there is no thermodynamic equilibrium known so far. In the following section, the nuclei types and the physics of these nuclei, and the nucleation processes are discussed.

2.4.1. Free gas nuclei

Free gas nuclei, are the entrapment of the NCG, in most cases air, in the form of bubbles in the liquid. These nuclei exchange mass with the liquid through mass diffusion due to the gradient of concentration of the gas in the liquid media from the bubble surface to the bulk liquid. These nuclei can be removed from the water by degassing through boiling or the application of vacuum. The existence of these bubbles is questionable. It is generally accepted that free gas nuclei exist in water. For example, vacuum flotation is a practical demonstration of free gas nuclei existence in water. However, there is no clear evidence for the existence of the free gas nuclei (microns or sub-microns) in water.

For every bubble, the pressure inside and outside of the bubble are related according to Laplace equation

$$P_B - P_\infty = \frac{2\sigma}{R} \tag{2.2}$$

where P_B is bubble pressure, P_∞ is the far liquid pressure, σ is the liquid/gas surface tension, and R is the bubble radius. The interfacial force balances the forces of the pressure from the gas inside the bubble and the pressure from the liquid.

In under-saturated water, there is no stable point in the free energy curve; therefore, the microbubbles are thermodynamically unstable (Zhou et al. 2009). According to Henry's law, the concentration of the gas is higher than the concentration of the gas in liquid, in the cases of undersaturated and saturated. Therefore, the free gas molecules diffuse into the liquid and result in shrinkage of the bubble. By decreasing the radius, due to the effect of surface tension, the pressure inside the bubble rises, resulting in a higher gradient of concentration on the bubble interface and bulk liquid. Epstein and Plesset (1950) solved, analytically, a simplified diffusion equation with no advection term to estimate the bubble growth or disappearance rate for different saturation ratios ($f=C_i/C_s$) i.e. the ratio of the gas concentration at bulk liquid to the concentration of the gas at the bubble interface. For example, a bubble, with radius of 10 μm, will dissolve in 1.17 seconds for $f=0$ i.e. no gas dissolved in the liquid.

In supersaturated water, the bubbles can become metastable at proper saturation ratio of the liquid with the gas; however, with a small deviation, microbubbles larger than this critical radius will grow and the bubbles smaller than the critical radius will vanish in the water. Therefore, in theory, microbubbles cannot exist in pure water. There have been a few suggestions for the possibility of the existence of microbubbles. Fox and Herzfeld (1954) suggested that the existence of an organic skin on the bubble surface could be a reason for sub-microbubble stabilization. In this model, the existence of long molecules of a surfactant or other organic chemicals can prevent the mass diffusion and bubble collapse. Recent developments in nanotechnology have brought the term "nanobubbles" with the size of 300 nm into the literatures (Zhou et al. 2009). Wu et al. (2012) were able to stabilize nanobubbles, produced in an HIA cell, for many hours using appropriate surfactants.

2.4.2. Vapor cavity nuclei

This type of nucleus is generated by external energy, i.e. ultrasound, mechanical shear, and laser excitation, which reduce the local pressure of water below the vapor pressure at a specific temperature. The composition of the vapor cavity is mostly water vapor, and the lifetime depends on dissolved gas content, the presence of surfactant, and other water contamination. Apparently, vapor cavity nuclei collapse when brought to the high pressure areas, resulting in high speed water jets that are responsible for erosion on the surfaces nearby. Vapor cavity nuclei can be generated by flowing water through different size and length of nozzle tips. Increasing water flow velocity results a decrease in the static pressure to less than water vapor pressure. If non-condensable gases have enough time to diffuse into the bubble before collapse, the bubble will have longer lifetime than a regular collapse.

2.4.3. Harvey nuclei

Harvey nuclei are the cavities appearing in hydrophobic crevices, due to low wetting properties of the crevices. For example, this type of cavity can exist in suspended solids or on the walls of container. There are two basic requirements proposed for this type of gas nucleation; first, the surface should be hydrophobic, and second, gaps with conical shapes acting as an active site for gas nucleation should exist (Wilt, 1986). More researches showed that hydrophobic surfaces are necessary for gas nucleation but not sufficient for extensive bubble formation in the liquid.

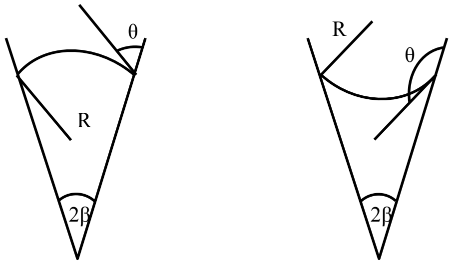

Figure 2.1 Air entrapment in a crevice of a hydrophilic (left) and hydrophobic (right) particle

The Harvey model for bubble entrapment in crevices is shown in Figure 2.1 (Harvey at al., 1944). The criterion for a stable bubble existing in a crevice is that the contact angle of the particle with liquid/air (θ) becomes $\pi/2$ larger than the crevice half angle (β), i.e.

$$\theta > \frac{\pi}{2} + \beta \tag{2.3}$$

In this case, the curvature of the bubble interface will be negative. As a result, the surface tension force will be negative, and in favor of stabilizing the bubble at an equilibrium stage.

Harvey nuclei are a source of bubble formation in many physical and biological systems. Particularly in flotation, as the particles are in erratic shapes, the Harvey nuclei are mostly formed in their crevices. Harvey nuclei cannot be removed easily due to interfacial properties of hydrophobic crevices. They can exist in porous particles such as coal in flotation process, and cause the decrease of the density for the particle, which results in non-settling of the particles.

2.4.4. Equilibrium of nucleus

For a spherical microbubble, containing gas and vapor, in equilibrium with water follows the Laplace equation shown below

$$P_\infty = P_v + P_g - \frac{2\sigma}{R} \tag{2.4}$$

where P_v and P_g are water vapor and non-condensable gases partial pressure inside the bubble respectively, P_∞ is the liquid far pressure, σ is gas/liquid surface tension, and R is the bubble radius.

Changing the liquid pressure, assuming the process is isothermal and constant gas content, the following relation is applied for equilibrium

$$P_\infty = P_v + P_{g0}\left(\frac{R_0}{R}\right)^3 - \frac{2\sigma}{R} \tag{2.5}$$

where P_{g0} and R_0 are initial equilibrium gas pressure and radius of the bubble. As shown in Figure 2.2, the curve P_∞ for different values of R, with lowering the pressure the bubble radius increases. However, there is a minimum pressure (P_c) that below this pressure, there is no equilibrium stage for the bubble. The difference of P_v-P_c is called static delay to cavitation. The value of P_c and corresponding R_c based on the initial equilibrium stage of the bubble, are calculated by

$$R_c = R_0 \sqrt{\frac{3P_{g0}}{2\sigma/R_0}} \tag{2.6}$$

$$P_c = P_v - \frac{4\sigma}{3R_c} \tag{2.7}$$

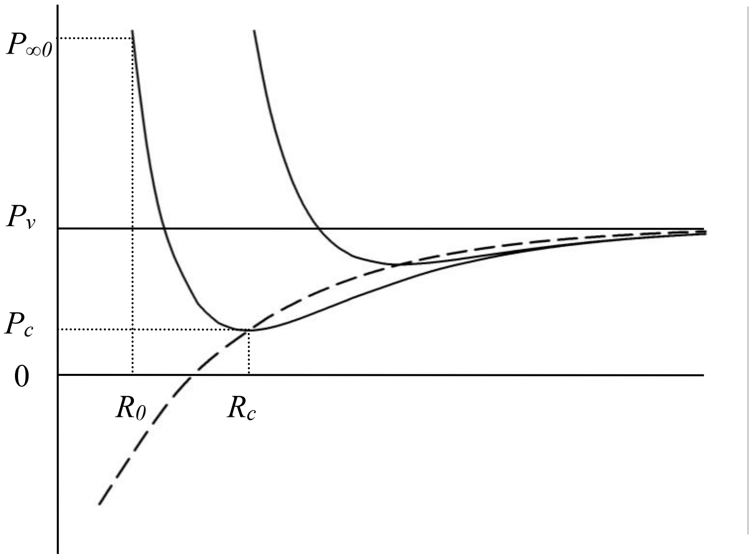

Figure 2.2 Equilibrium stages of bubbles for different liquid pressure and initial radius of the bubble

Decreasing the liquid pressure, results in expansion of the bubble to the new equilibrium stage. However, if the pressure is reduced lower than critical pressure, the bubble has no equilibrium stage, therefore, it will expand with a certain speed, known as cavitating, until the pressure is brought back over the critical pressure. At this moment the bubble would collapse and after a few rebounds it will resume its equilibrium stage at the imposed pressure. The dynamics and behavior of the bubble is modeled using the well-known bubble dynamics equation, the Rayleigh-Plesset equation.

2.4.5. Nucleation

There are two types of nucleation, homogeneous and heterogeneous nucleation.

The formation of gas or vapor nuclei in a bulk pure fluid is called *homogeneous nucleation*. In homogeneous nucleation, it needs to form very small nuclei or embryos. According to classical nucleation theory for a droplet, there is an energy barrier for the formation of new nuclei in a homogenous phase (Sigsbee and Pound, 1967; Blander and Katz, 1975; Lubetkin, 1994). The free energy of formation for a new droplet consists of a surface term and a bulk term:

$$\Delta G = \Delta G_{surface} + \Delta G_{bulk} = 4\pi r^2 \sigma - 4\pi r^3 \Delta G_v / 3 \tag{2.8}$$

where ΔG_v is the Gibbs free energy per volume of the droplet is expressed as:

$$\Delta G_v = \frac{kT}{v} \ln \lambda \tag{2.9}$$

λ is the ratio of the vapor pressure for a curvature of radius r to the vapor pressure at flat surface. The free energy curve has a maximum at a critical radius, r^*, with ΔG^*. A similar argument about the bubbles leads to a critical bubble radius which is

$$r^* = \frac{2\sigma}{p_v - p} \tag{2.10}$$

where p_v is the vapor pressure of the liquid and the p is the pressure of the liquid. The nucleation rate, i.e. the number of bubbles formed per second per cubic centimetre of solution, can be expressed in a general form:

$$J = C \exp(-\Delta G) \tag{2.11}$$

where C is a constant. Homogeneous nucleation is less practical in real systems due to the presence of impurities. In practical situations, a solid surface such as vessel walls and dust particles, provide sites for nucleation of a new phase which need less extreme condition compared to homogeneous nucleation. The formation of nuclei on the surface of a solid body is called *heterogeneous nucleation*. Harvey et al. (1944) was the first to suggest that crevices existing in solid surfaces are the potential for bubble nucleation. A reason for that might be the pre-existing gas trapped in the cavities due to the stability explained in Section 2.4.3. Many researchers have suggested that the presence of the particles in pure liquid can promote the bubble formation (Ryan et al., 1993). Even highly denucleated water contains some particle that lowers the cavitation threshold. The effect of solid surface in nucleation rate is imposed by a correction factor, $f(\theta)$, that is multiplied by the free energy term from homogeneous nucleation.

$$\Delta G^{*}_{Het} = \Delta G^{*}_{Hom} \times f(\theta) \tag{2.12}$$

where θ is the contact angle of the solid/liquid/gas interface. $f(\theta)$ is defined as

$$f(\theta) = \frac{\left(2 - 3\cos(\pi - \theta) + \cos^{3}(\pi - \theta)\right)}{4} \tag{2.13}$$

$f(\theta)$ varies from 1 for a value of 0 for θ to 0 for a value of π. Therefore, the solid surfaces with higher contact angle (hydrophobic surfaces) are more favorable positions of nucleation. Harvey et al (1944) suggested the cavities or gas pockets trapped in micron-size particles as cavitation nucleation sites, i.e. Harvey nuclei or free stream nuclei. Many of the observations of the onset of cavitation suggest free stream nuclei as the place for excitation rather than surface nuclei (Brennen, 1995). However, recent studies show that surface nuclei can have a dramatic effect on cavitation initiation. Porosity, roughness, and contact angle are the major parameters that affect the surface nucleation (Holl, 1970). Some studies have been conducted to investigate the effect of surface properties on the heterogeneous nucleation (Qi et al., 2004; Yang et al., 2003; Li 2014). However, exact modeling of these parameters has not been accomplished due to the complexity.

2.5. The role of cavitation on fine particles flotation

As described previously, low inertia of small particles do not favor the collision and attachment of fine particles to the large and small bubbles. In another explanation, cavitation process can be implemented to nucleate small bubble on fine particles which can be a bridge to particle attachment to bigger air bubbles (Zou et al., 1997). Tao et al. (2006, 2008) said that the pico-bubbles generated by hydrodynamic cavitation nucleate at the surface of hydrophobic particles, which provide ultrafine particles adhere to pico-bubble without the need of collision. They also stated that particles are less likely to detach from smaller bubbles due to their lower acceleration force and centrifugal force associated with the detachment process reducing the probability of detachment.

Zhou et al. (1997) explored the role of cavitation on fine particle flotation enhancement, passing the feed slurry through a cavitation tube before the flotation cell. It is evident that increasing slurry velocity in a cavitation tube increases the number and size of cavity bubbles. From the set of experiments, it was found that the optimum flow velocity through the nozzle (17-26 m/s) maximizes the recovery by creating bubbles at the size of particles. Zhou et al (1997) suggests two possible mechanisms for the enhancement of particle to bubble attachment as shown in Figure 2.3. In both mechanisms, the attachment of particle to bubbles is replaced by the nucleation and growth of bubble on the surface of the particle, which can be a bridge to easier attachment due to bubble/bubble interaction instead of bubble/particle interaction. The observation suggests that too high energy input could disrupt bubble particle aggregation, contradicting the benefits of hydrodynamic cavitation.

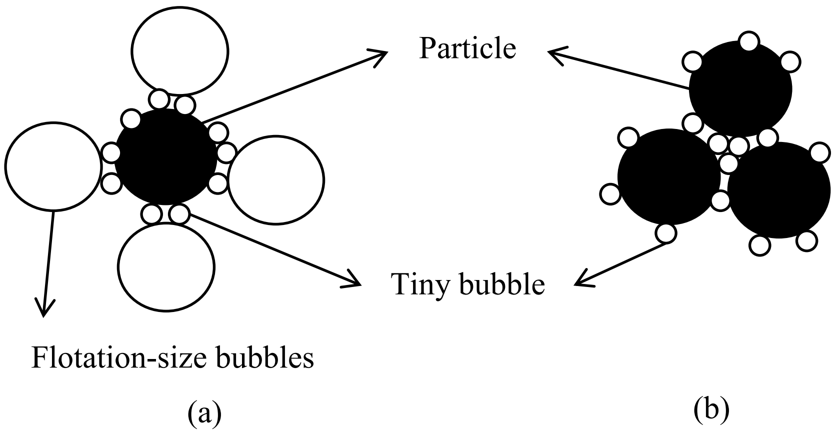

Figure 2.3 Possible mechanism for fine particle flotation by hydrodynamic cavitation, (a) Two-stage attachment; cavitated tiny bubbles attach to a mineral particle, which then attaches to a flotation-sized bubble (b) enhanced coagulation by bubble bridging. Based on a figure in Zhou et al. (1997)

The concept of a cavitation tube was further studied to improve fine coal flotation at the lab scale by CSIRO Energy Technology and Novatech Consulting in Australia (Hart et al., 2002) and Coalberg seam coal in USA (Tao et al. 2006) (Figure 2.4). The size of the bubbles produced by hydrodynamic cavitation (Picobubbles) is two orders of magnitude smaller than the microbubbles generated by static mixer i.e. ~0.9 µm. The results show 10-40 % increase in fine coal flotation recovery. The picobubbles increase the coarse particles (>0.3 mm) recovery much more than fine particles (<30 µm) (Tao et al. 2008). Creating cavitation by ultrasonic field for pre-treating coal feed slurry has been studied at a small scale. Although it is not applicable to industrial scale, more researches are designed for this application of acoustic cavitation. Bubble nucleation by cavitation can also agglomerate ultrafine particles by bubble bridging, making them appear as if they are larger particles of higher probability of attachment to the large bubbles in a flotation cell.

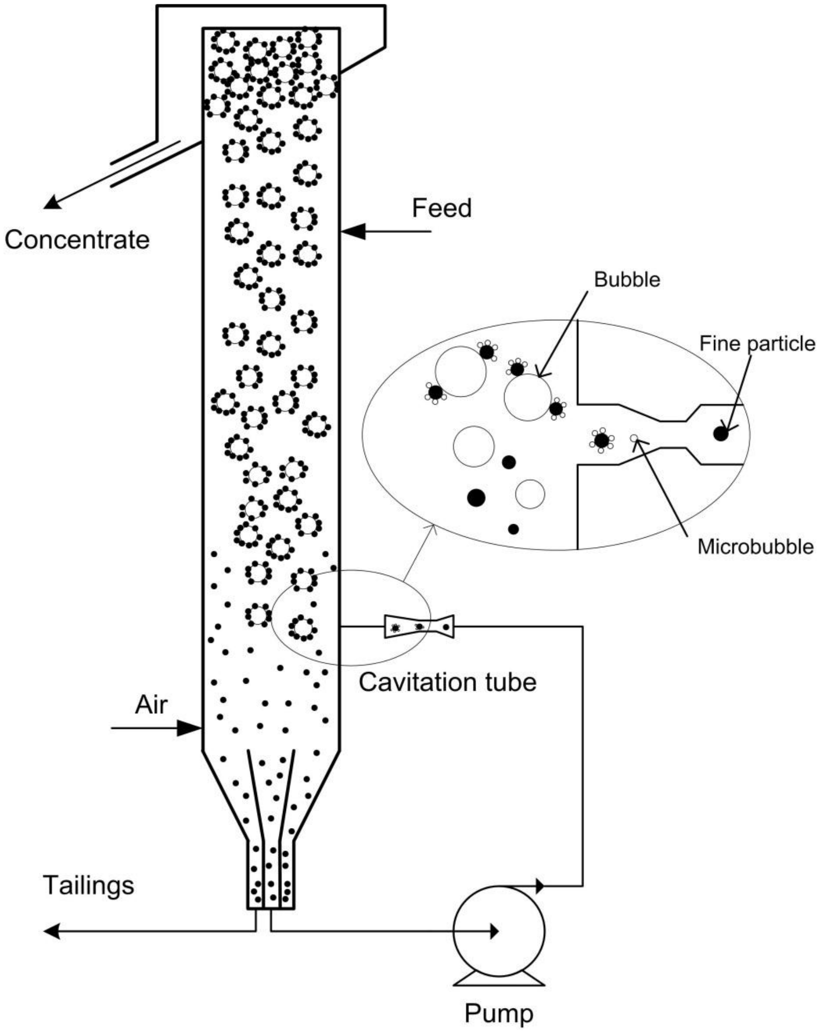

Figure 2.4 Implementing a cavitation tube in a flotation column (Tao et al. 2008)

2.6. Cavitation modeling

As discussed in Chapter 1, the ideal numerical method consists of many physical models to accurately predict the flow features such as unsteadiness, turbulence and etc. Some of the challenges in the modeling of cavitation include the multiphase flow, compressibility of the gas phase, large ratio of properties between phases, various time and length scales (Senocak and Shyy, 2004).

One of the early works on the modeling of cavitation is that by Delannoy and Kueny (1990). They employed an empirical barotropic equation for the variation of density, as a function of pressure and sound speed, in the two-phase zone. The model was applied to a 2-D geometry and compared with the experimental results in a venturi nozzle. Schmidt, Rutland and Corradini (1997, 1999) used a Homogeneous Equilibrium Model (HEM) to simulate cavitation by a continuous compressible liquid–vapor mixture. Although accounting for the compressibility was an advantage of this model, the model did not account for the turbulence and had a problem in predicting the small bubbly cavitation mode.

Beside the models based on the thermodynamic considerations, there are models that couple the Transport Equation Model (TEM) of vapor fraction with the Navier-Stokes equation for modeling of attached cavities on hydrofoils or submerged surfaces (Kubota et al., 1992; Wang et al., 2007; Senocak and Shyy, 2004). In this approach, each phase is considered an incompressible medium and the viscosity and density of the domain changes linearly from the liquid phase to the gas phase, known as the mixture model. For the gas phase, a bubble radius and number density function is assumed that is used for the calculation of vapor phase. In most of the models, the bubble number density is assumed to be constant and radii of the bubbles are estimated. These models are based on the growth of bubbles nuclei as source of cavitation. A simplified version of Rayleigh-Plesset (RP) bubble dynamics equation, known as asymptotic equation, is used for the calculation of growth and collapse. It also assumes that the cavitation source depends only on the difference of liquid pressure and vapor pressure. Therefore, the existence of non-condensable gases or contamination is neglected. Yuan et al. (2001) used k-ω turbulence model to simulate cavitation in a single-hole sharp and curved edge nozzle, which led to a steady-state solution with no transient behavior. Using a similar approximation of R-P equation, Singhal et al (2002) developed a full-cavitation model that included the effect of NCG, local turbulence on the evaporation and condensation terms. The evaporation and condensation coefficient were selected by comparing the modeling result to experimental data from cavitation over hydrofoils, submerged cylindrical bodies, and inside a sharp-edge orifice. A good agreement was found in comparing the coefficient of discharge for sharp edge orifice and pressure coefficient for all the cases.

In contrast to all of the mentioned Eulerian bubble-based models, Hsiao and Pauley (1999) used a Lagrangian frame to track the cavitating bubbles in the tip vortex of a ship propeller. The sensitivity of the flow to the cavitation inception for different cavitation numbers was studied. However, due to lack of a proper time stepping method in integration of R-P equation, the model was not able to track the bubble after the first collapse. Later, this approach was used by a few researchers for the study of cavitation (Farrel et al., 2003; Hsiao and Chahine, 2004; Giannadakis et al., 2004; Shams et al., 2011). An advantage of this approach, compared to Eulerian approaches, is that the dynamics of the bubbles can be captured accurately. Moreover, the behavior of each bubble, bubble/bubble interactions, boundary conditions, and gas diffusion can be modeled for each bubble separately. Unfortunately, in most cases bubble/bubble interaction and gas diffusion modeling in cavitation flows are neglected as a simplification.

For turbulence modeling, Raynolds Average Navier-Stokes (RANS) models can be used in cavitating flows for both approaches. Large Eddy Simulation (LES) model has the advantage of being able to capture dynamic features of the turbulent flow field more accurately, i.e. pressure and velocity profile, bubble fluctuating motions. However, it is computationally expensive, and needs a much finer grid.

Chapter 3

Experimental Investigation of Cavitation

In this chapter, we review some investigations that have been done on cavitation in contractions such as orifice and venturi, for a better understanding of the cavitation. Later, an experimental setup is explained to study the onset of cavitation in a small glass tube. Then, the methods of measuring bubble size distribution in a venturi type are investigated. The liquid is water with air and carbon dioxide as the dissolved gas. The results of each set of experiments are discussed in the related section.

3.1. Onset of cavitation in orifice

In this set of experiments, the cavitation in an orifice was investigated in a 1 inch water loop. The schematic diagram of the experimental loop is shown in Figure 3.1. The 35 m long horizontal loop was made of 25.4 mm ID copper tube. A variable speed progressive cavity pump, Moyno pump, was used to circulate water up to a maximum velocity of 6 m/s. Untreated water was pumped from a top-open 1 m^3 tank. A coriolis mass flow meter, Krohne MFM 4085K, was used to measure the volumetric flowrate and temperature. A Nikon D5 camera with macro lens was used to capture the bubbles from the cavitation immediately downstream of the orifice. A circular orifice with a hole diameter of 12.7 mm and

6 mm thickness was used to incept cavitation. Figure 3.2 shows snapshots of the flow and cavities at different Reynolds and Cavitation numbers. The cavitation number is defined as:

$$CN = \frac{p_o - p_v}{\frac{1}{2}\rho u_o^2} \tag{3.1}$$

where p_o and u_o are the outlet pressure and velocity respectively.

A summary of the observations are as following. The nucleation site in the sharp edge orifice was investigated and is shown in Figure 3.2. However, a clear picture able to show this nucleation site was not possible due to the curvature and opaqueness of the orifice. Figure 3.2-a shows no cavitating flow as a reference. Moreover, at low cavitation number, where there is no major nucleation, some bubbles downstream of the orifice are observed although no bubble was observable upstream of the flow. These bubble can be a result of cavitation for free stream nuclei existing in upstream of the orifice. At higher cavitation number, the bubble cloud is expanded from the nucleation site at the throat, and is captured in the visualization cell. In this observation, there are two regions of cloud cavities. Region I includes high concentration of microns-small size bubbles. The nature of these bubbles is predicted to be the vapor cavities formed at the nucleation site at the orifice inner surface. These bubbles are unstable and collapse as they enter the high pressure region. Region II includes bigger bubbles at lower concentration, compared to region I. These bubbles are more stable and can be carried out to the slurry tank. The bigger bubbles can be a result of coalescence of vapor cavities together and with the free stream nuclei. However, the cavitation bubbles are naturally unstable and should disappear as entering the high pressure region. The stable bubbles formed in these experiments can be justified with the diffusion of the NCG, i.e. air, dissolved in water into the formed vapor cavities and free stream nuclei. These experiments show that the role of NCG dissolved in the cavitating liquid is important and should be accounted for in cavitation inception.

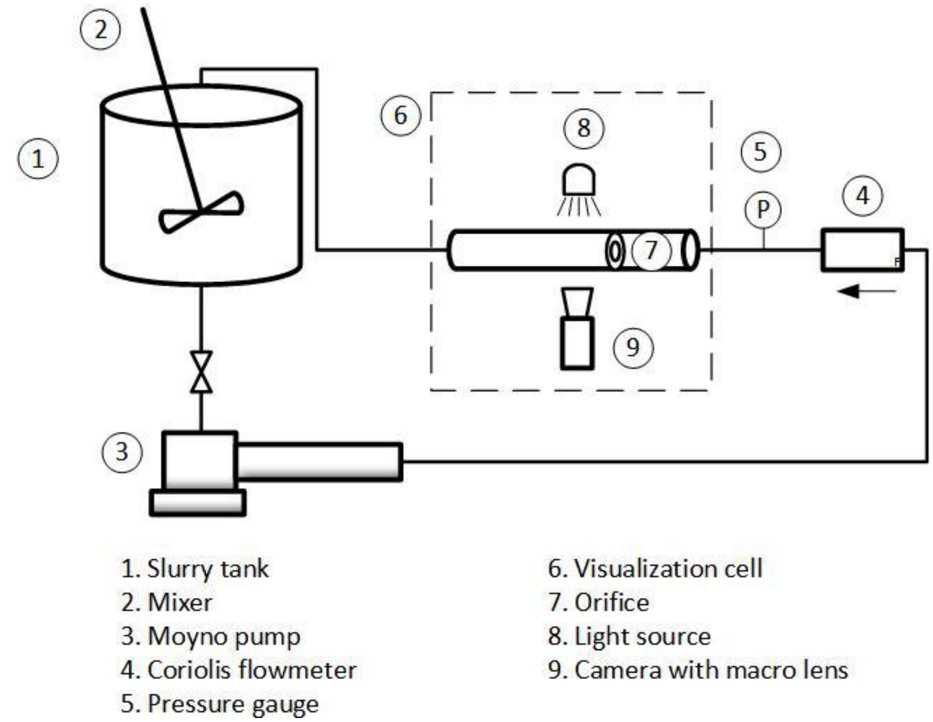

Figure 3.1 Schematic of the water loop for study of cavitation in orifice

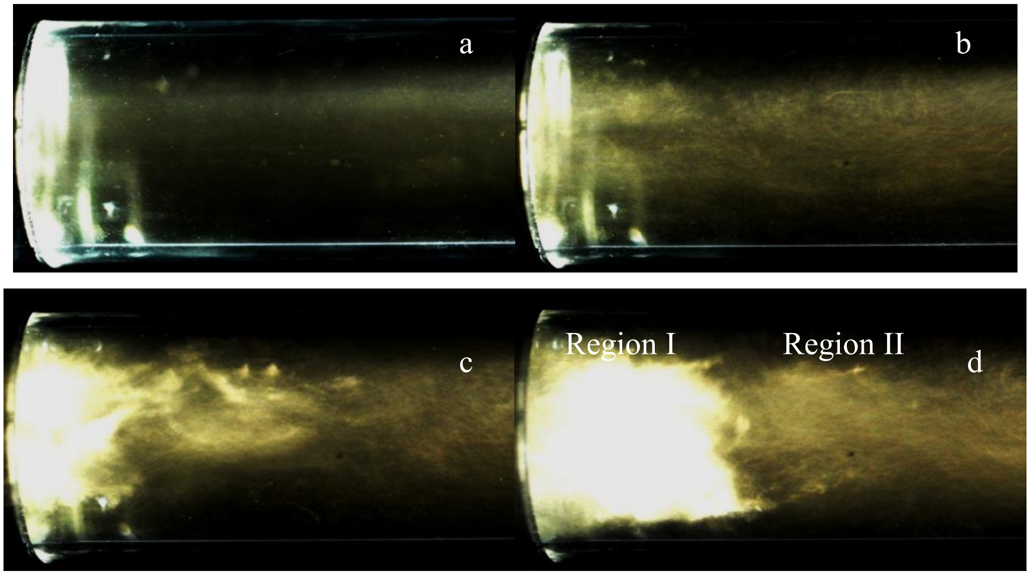

Figure 3.2 Photos of cavitation bubble cloud downstream of the orifice. Corresponding cavitation number and throat average velocities are: a) *CN*=2.1, V=10 m/s b) *CN*=1.27, V=14 m/s, c) *CN*=1.03, V=16 m/s, d) *CN*=0.84, V=18 m/s

3.2. Onset of cavitation in venturi

To study the role of gas diffusion on the cavitation inception a new setup with a small scale was designed. A venturi with dimensions shown in Figure 3.3 was made from glass. A pressurized vessel was used to remove the need for a pump for the cases where the pump causes nucleation of new bubbles due to the low pressure at the suction. This case is more possible to occur at experiments that involve high gas content in the liquid. Implementing a pressurized vessel to flow water decreases the chance of bubble nucleation before the venturi tube. A 20 L reinforced cylindrical plexiglass vessel was used as the pressure vessel. The tank was equipped with a pressure gauge to measure the pressure inside the vessel, and a needle valve that controls the flow of compressed gas to tank. A Cole-Parmer rotameter with a range of 200 to 3000 cm^3/min for water, was used to measure the flowrate. A Rosemount DP cell was used to measure the pressure drop on two sides of the venturi. No pressure measurement was applied to the throat as it would affect the cavitation inception.

To investigate the bubble nucleation, a 5 mW laser, with a 2 mm diameter pointer, was pointed at the venturi expansion section, and the light intensity was measured on the other side of the venturi using an Extech wide range light meter as shown in Figure 3.4. The existence of more bubbles on the path of the laser beam decreases the light intensity due to light diffraction by the bubbles. To capture the instantaneous bubble nucleation the laser was located 1 mm after the venturi throat.

Deionized (DI) water with resistivity of 10 MΩ was used in these experiments. To prepare Air Saturated Water (ASW) at atmospheric pressure, the water in feed tank was circulated (using a peristaltic pump) and sprayed from the top of the tank through a 1 mm nozzle. To prepare CO_2 Saturated Water (CSW), the DI water was sparged with CO_2 using a soda maker (Sodastream) device. The water becomes oversaturated with CO_2. After the supersaturated water was transferred to the tank and was sealed, the extra gas separated from the water was used to purge the air from the top of the feed tank. After a few initial purges, the tank was sealed and left overnight. The final equilibrium pressure was used to calculate the CO_2 content of the water. To DeGassed Water (DGW), DI water was heated to reach a temperature of 80 ºC and heated for 10 minutes at this temperature over electrical heater. This step would remove most of the gas dissolved in the water and speed up the degassing process. Then, it was cooled to room temperature and was sprayed from the top of the pressure vessel which was already in vacuum at pressure of 25 kPa absolute. The tank was sealed and left overnight at that pressure. For DGW a peristaltic pump was used as very high flowrates were required.

For each experiment, first, the feed tank was filled with water at controlled conditions. Then, it was pressurized with nitrogen gas to the required pressure to reach the desired Re number at the inlet of the venturi. For each batch of water in the feed tank 3-5 data points could be collected. Therefore, to study the reproducibility for different batches of water sample, 3 batches of water were prepared and used for experiments. All the data are reported in the results section.

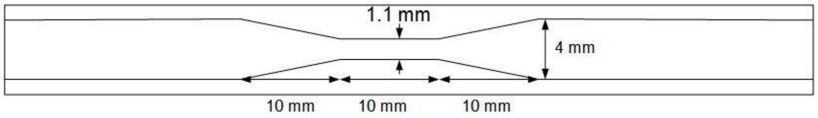

Figure 3.3 Studied venturi dimensions

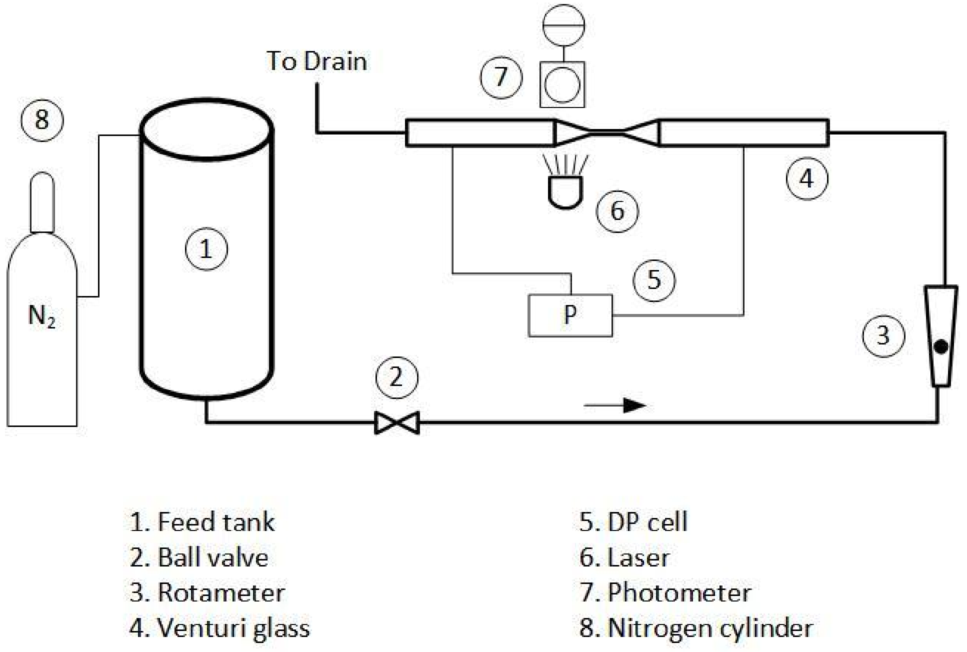

Figure 3.4 Cavitation inception detection setup

In this set of experiments, cavitation inception Re number at the inlet of the venturi was investigated. By increasing the velocity and maintaining the downstream pressure of the venturi at atmospheric pressure, the cavitation number could be reduced. At a certain Re, the pressure falls below the vapor pressure also known as onset of cavitation Re number. Figure 3.5 shows the ratio of light intensity at each experiment to the initial light intensity. Cavitation inception Re number is defined as the Re of the liquid at the inlet of the venturi (ID=4 mm), based on the flowrate of water upstream, in which the bubble nucleation starts to occur. This Re is identified from the graph in Figure 3.5. The cavitation inception was estimated based on the first point that the obstruction of light by the bubbles was detected. Each set of experiments are obtained from experiments for 3-4 batches of water samples at different times. It can be concluded that the results are reproducible.

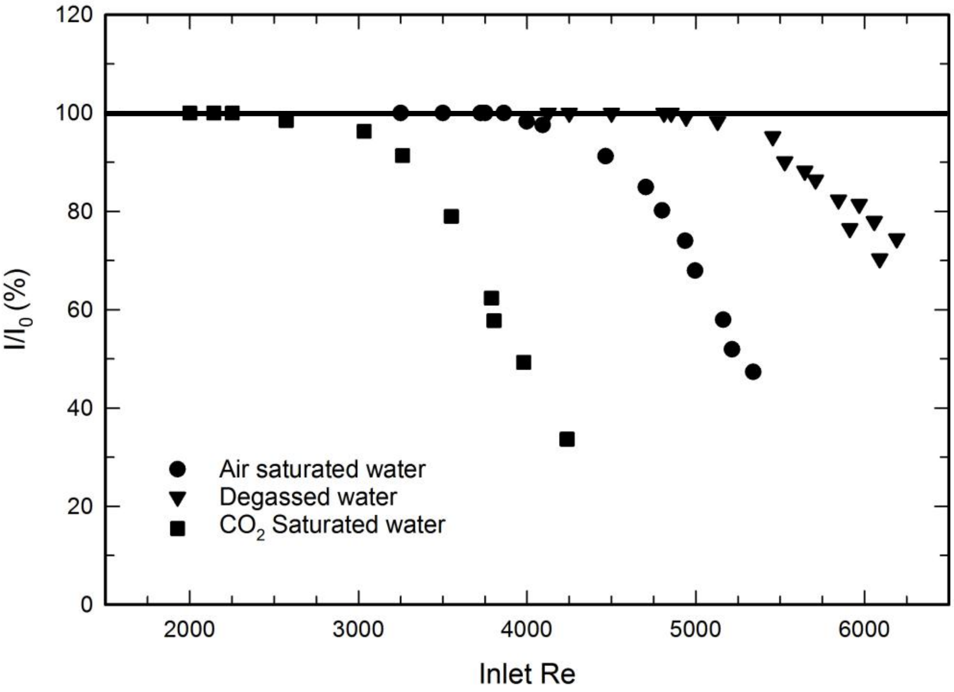

Figure 3.5 Light intensity measurement for various water conditions at different Re

Table 3.1 shows the estimated cavitation inception Re numbers extracted from the experiments. As it can be interpreted, the existence of NCG in the liquid can affect the cavitation inception significantly. Comparing the concentrations of the three samples shows that this effect is bigger for lower concentrations of dissolved gases. This means that the cavitation inception Re number varies significantly by the concentration of dissolved gases at lower concentrations.

Table 3.1 Experimental results of the cavitation inception for different gas contents

Estimated gas content (ppm)	Cavitation inception Re number
5	5200
21	4000
1500	2300

3.3. Bubble size distribution measurements

In this section, different methods of measuring bubble size distribution, which has been applied in this study, are explained. Light transmission method and conductivity measurement were investigated. Moreover, commercial devices such as Mastersizer, ABS, and FBRM were implemented. All the methods and devices will be explained here except conductivity measurements for measuring the gas holdup between the probes. In this method, the conductivity of the solution between two probes is measured. In the existence of gas in the measuring volume, the conductivity decreases due to low conductivity of the gas phase. Experimentally, it was concluded that the total gas volume fraction is too small to result in a measureable conductivity change. Therefore, this method failed to give results and it will not be discussed further.

3.3.1. Light transmission method

This method is explained in detail by Mclaughlin and Rushton (1973), Lockett and Safekourdi (1977), and Mariaux and Achard (1988). When a parallel light beam is passed through a bubble swarm, the light can attenuate by diffraction, reflection, refraction, and absorption. The undistracted light can be captured on the other side using a photometer. The ratio of the light intensity captured after passing through the bubble dispersion to the initial light intensity without the bubble on the path, can be related to the interfacial area concentration of the bubbles, which is related to the bubble volume fraction and the Sauter Mean Diameter (SMD). Many of the mentioned studies have worked on the correlation of these two parameters. The common correlation that is found is:

$$\ln\frac{I}{I_0}=\frac{K\Gamma l}{4}=\frac{K}{4}\frac{6\alpha}{D_{32}}l \tag{3.2}$$

I and I_0 are the light intensity in the presence and absence of bubble swarm. Γ is the Interfacial Area Concentration (IAC) of the bubbles, l is the length of the path that light crosses the bubble swarm. α are D_{32} are the volume fraction and SMD of bubbles. K is a constant of value 1.08 (Lockett and Safekourdi, 1977). This correlation is limited to a few conditions. First, the size of the bubbles should be very large compared to the light wavelength. It also needs to be very small compared to the cross section area of the light beam. In our experiments, a monochromatic (red~670 nm) laser with a circular area of 2 mm diameter was used. For this wavelength, the bubble size should be 10 times larger. Thus, this method is applicable to bubbles that are larger than 7 μm. Second condition is to prevent the multiple scattering of light because the theory is based on the assumption that each bubble receives undeviated radiation. This assumption has been examined experimentally, and the following condition has to be satisfied:

$$\Gamma l = 6\frac{\alpha}{D_{32}} l \leq 26 \tag{3.3}$$

The experimental setup for this method, which was similar to the setup for cavitation inception experiments, is illustrated in Figure 3.6. To improve the reliability of the results from this method, a dark painted 1 m pipe and a plate with a laser pointer size hole (shown in Figure 3.6) were implemented to eliminate the light beams that were diffracted at very small angles. Thus, only undeviated beams will reach the photometer. To test the setup, a few calibration experiments were conducted. In these experiments, glass beads of two size distribution were used at various concentrations to obtain various interfacial area concentrations. The glass beads properties are summarized in Table 3.2. The suspension was kept homogeneous using a turbine mixer at 500 rpm. The suspension was pumped through the test section. For each suspension, 10 measurements of light intensity were acquired. From the light intensity measurements, the constant in Equation 3.2, *K*, was calculated. The average value for *K* for all of the experiments is 0.98 which is very close to the literature value, 1.08.

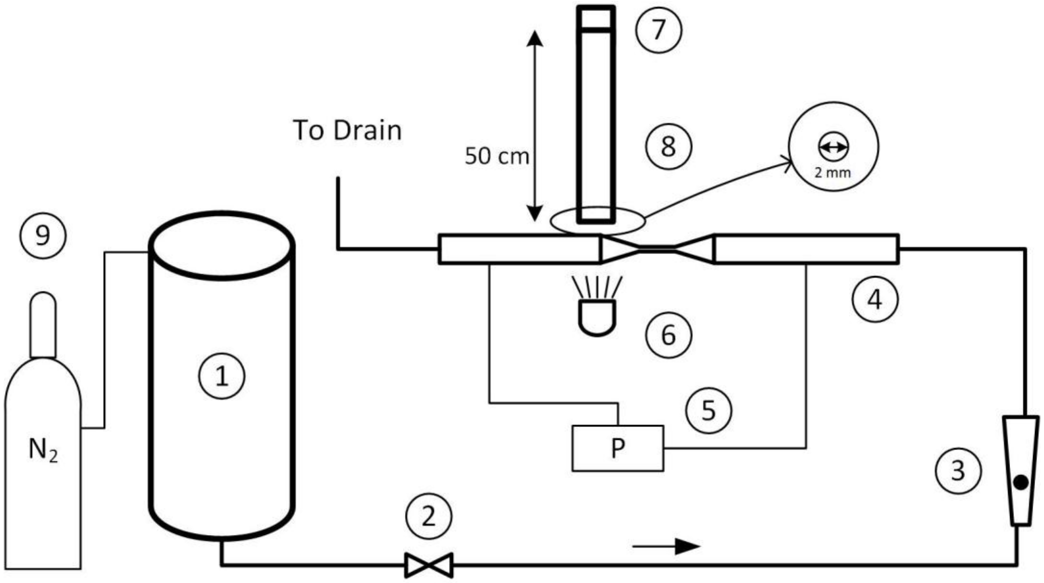

1. Feed tank
2. Ball valve
3. Rotameter
4. Venturi glass
5. DP cell
6. Laser
7. Photometer
8. Dark tube
9. Nitrogen cylinder

Figure 3.6 Schematic of the light transmission measurement setup

Table 3.2 Experimental conditions for the calibration set of experiments and the measured constant, K, values

Glass bead D_{32} (μm)	Glass bead %Vol	Constant value, K
65	1	0.78 ±0.04
65	0.2	1.06 ±0.09
65	0.1	1.07 ±0.07
65	0.02	1.28 ±0.23
90	2	0.92 ±0.06
90	1.5	0.97 ±0.03
90	1	0.75 ±0.06
90	0.15	1.00 ±0.09

The interfacial area concentration, which is related to the volume fraction and SMD, measured by this method for ASW versus the inlet Re number is shown in Figure 3.7.

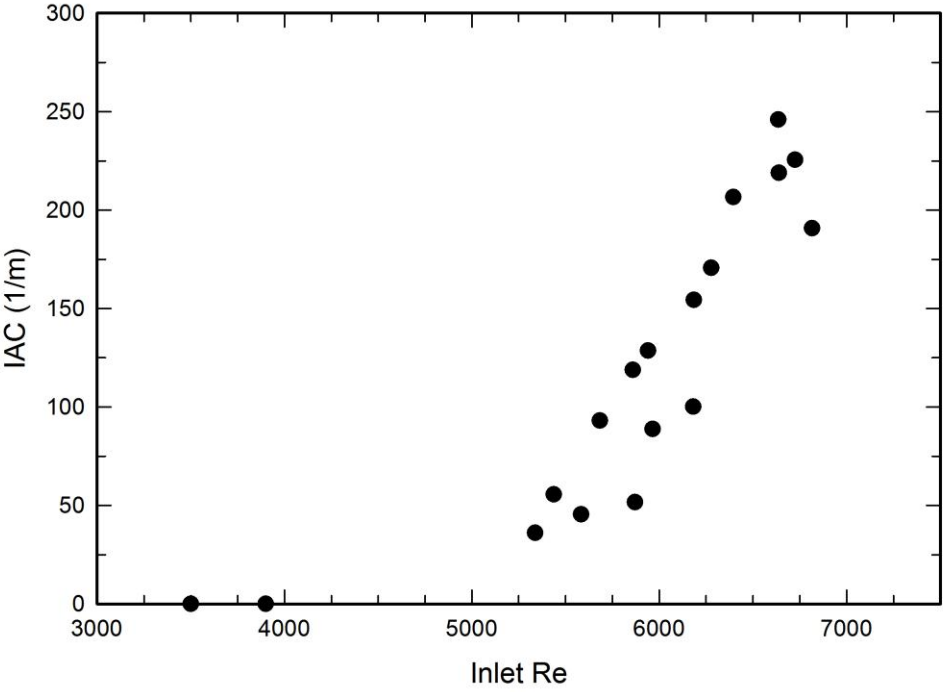

Figure 3.7 Results of IAC from light transmission measurement setup

3.3.2. Mastersizer

Mastersizer is a device to measure particle size distribution of particles based on the technique of laser diffraction. A dispersed sample passes though the measurement area, where a laser beam illuminates the particles. A series of detectors then measure the intensity of light scattered by the particles within the sample for both red and blue light wavelengths and over a wide range of angles. Mie scattering model is used to compute the size distribution and volume fraction of the dispersion with an accuracy of 1%. In our study, a Malvern Mastersizer 2000 was used to measure bubble size distribution. To do this, the downstream of the venturi was connected to the inlet port of the instrument. Consequently, the bubbly flow passed through the sampling window of the Mastersizer. The requirement for high accuracy was to provide certain number of bubbles in the measuring window resulting in a restricted range for measurement. Another disadvantage was that as the flow path through the measuring window was a complicated geometry, the bubble size might change due to bubble interaction.

Figure 3.8 shows a sample of bubble size distribution measured by Mastersizer for a flow through venturi at Re=6000. Three samples during each run is measured and the average of them was provided in a table in the report by the instrument. The D_{32} (SMD), D_{43}, and volume fraction of the sample were provided in the report. Table 3.3 shows the results of measurements with a Mastersizer. It is observed that the bubble size (SMD) and volume fraction increase with the increase in flowrate. Increasing the flowrate produces more regions lower than vapor pressure, which results in more bubble formation. Figure 3.9 shows the results from Mastersizer and light transmission method for comparison. IAC was calculated for the data from Mastersizer and were inserted into the graph shown in Figure 3.7. As it can be seen, the results are comparable, showing the accordance of these two methods of measurement.

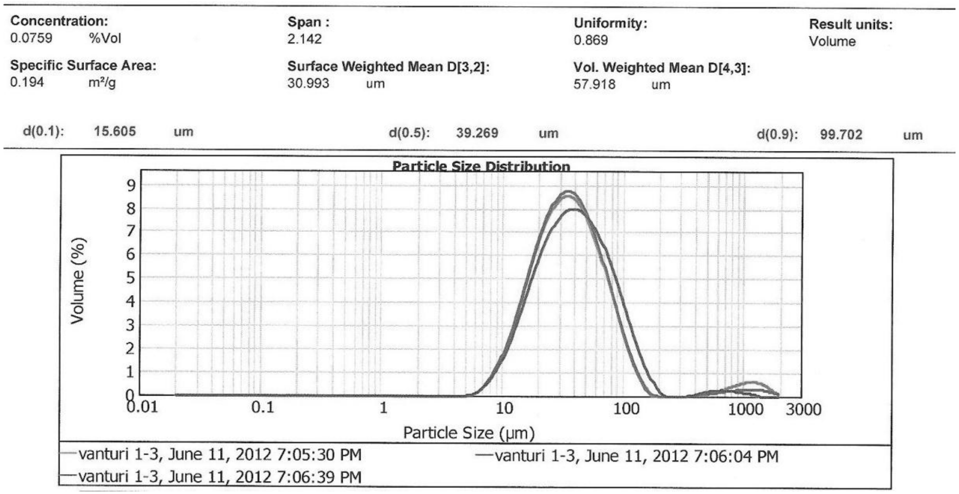

Concentration: 0.0759 %Vol
Span : 2.142
Uniformity: 0.869
Result units: Volume
Specific Surface Area: 0.194 m²/g
Surface Weighted Mean D[3,2]: 30.993 um
Vol. Weighted Mean D[4,3]: 57.918 um

d(0.1): 15.605 um
d(0.5): 39.269 um
d(0.9): 99.702 um

Figure 3.8 Sample bubble size distribution from Mastersizer for ASW at Re=6000

Table 3.3 Results of measurement from a Mastersizer

Velocity (m/s)	Gas volume fraction (%)	SMD (μm)
6000	0.08	31
6375	0.09	35
6750	0.12	39

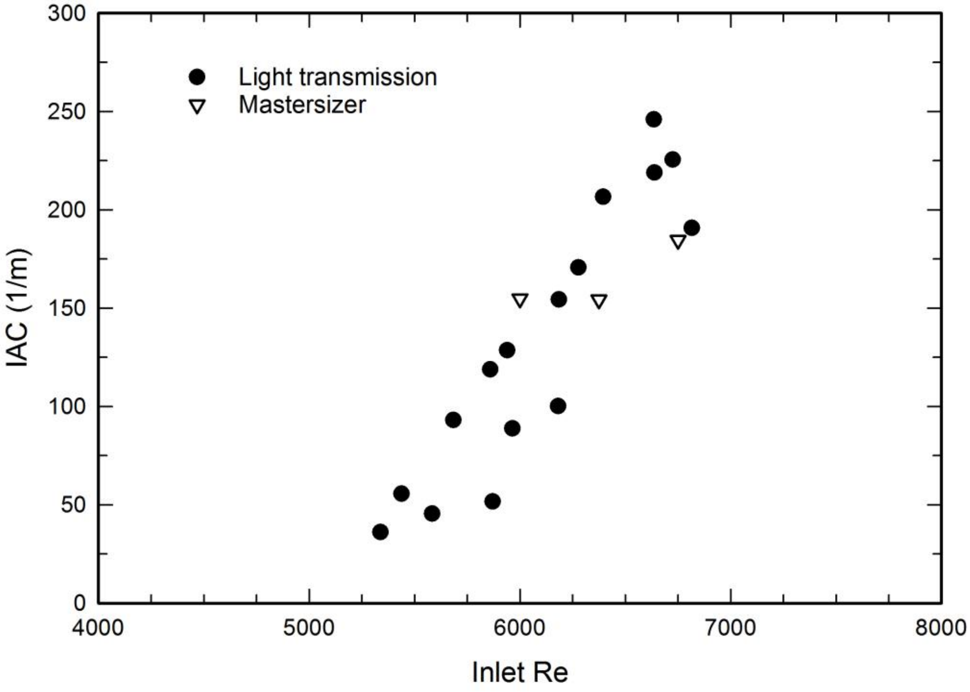

Figure 3.9 Comparison of data from light transmission method and Mastersizer

3.3.3. FBRM

Focused Beam Reflectance Measurement (FBRM), is a commercial device that is used for in-situ measurements of particle size distribution based on the reflection of light upon hitting the particles. The schematic of this instrument is shown in Figure 3.10. FBRM consists of two components, a red laser generator and a light detection probe. The laser light is emitted through a sapphire glass window at the tip of the probe. If the light is reflected due to the presence of a particle/bubble, the light reflects and can be detected. The time of light reflection is measured and related to the size of the particle/bubble. FBRM provides the chord length distribution, which is in the range of 0.5 μm to 1000 μm, and number counts (#/s). For a given particle, the chord length is known to be smaller than the diameter. However, such a difference is small and negligible for spherical particles (Kail et al., 2009). Li (2014) conducted experiments to compare the size distribution measured by FBRM with image analysis method for bubble swarm, and found reasonable agreement. For the bubble measurement using FBRM, the venturi was placed vertical in a large fish tank with the outlet 5 cm below the water level. The FBRM was positioned 2 cm above the outlet at an angle of about 45º, relative to horizon axis. This distance allowed the velocity of the bubbles in water jet drop below the FBRM velocity limit (2 m/s). The schematic of the setup is shown in Figure 3.11.

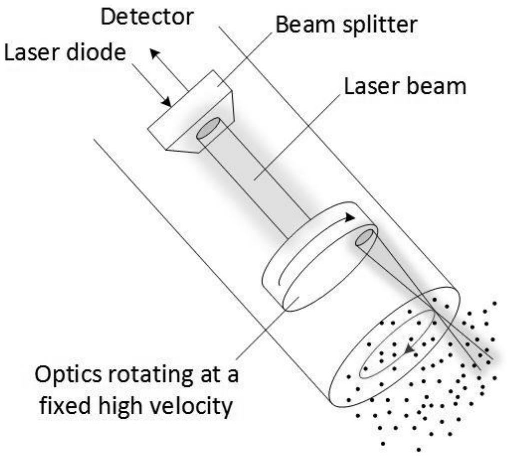

Figure 3.10 Schematic of the FBRM

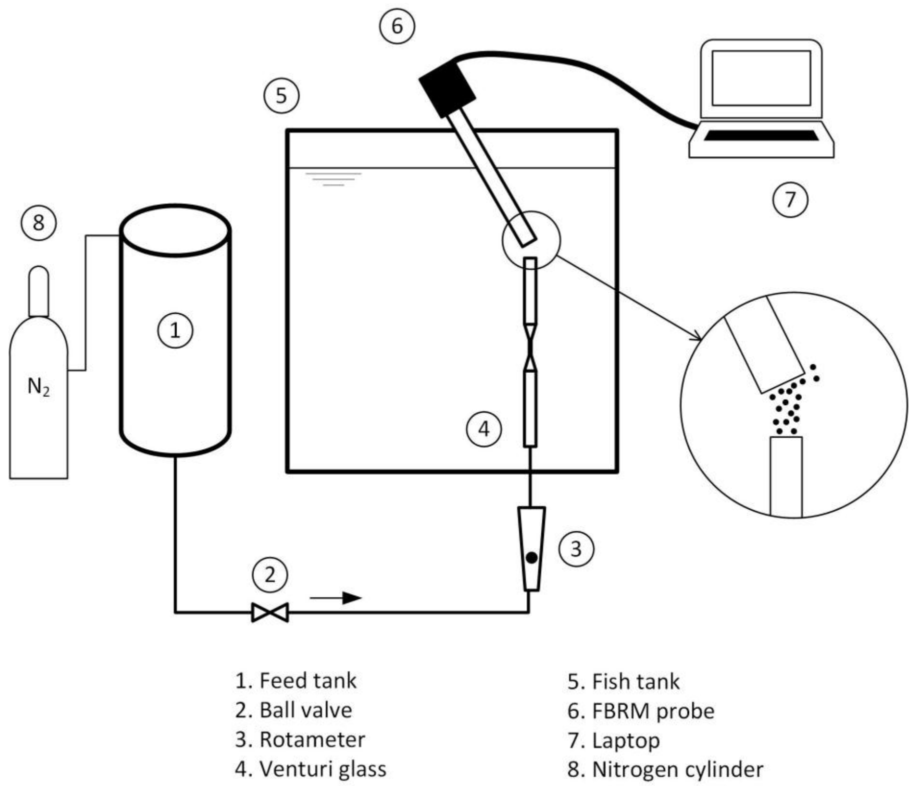

Figure 3.11 Schematic of the bubble measurement setup using FBRM

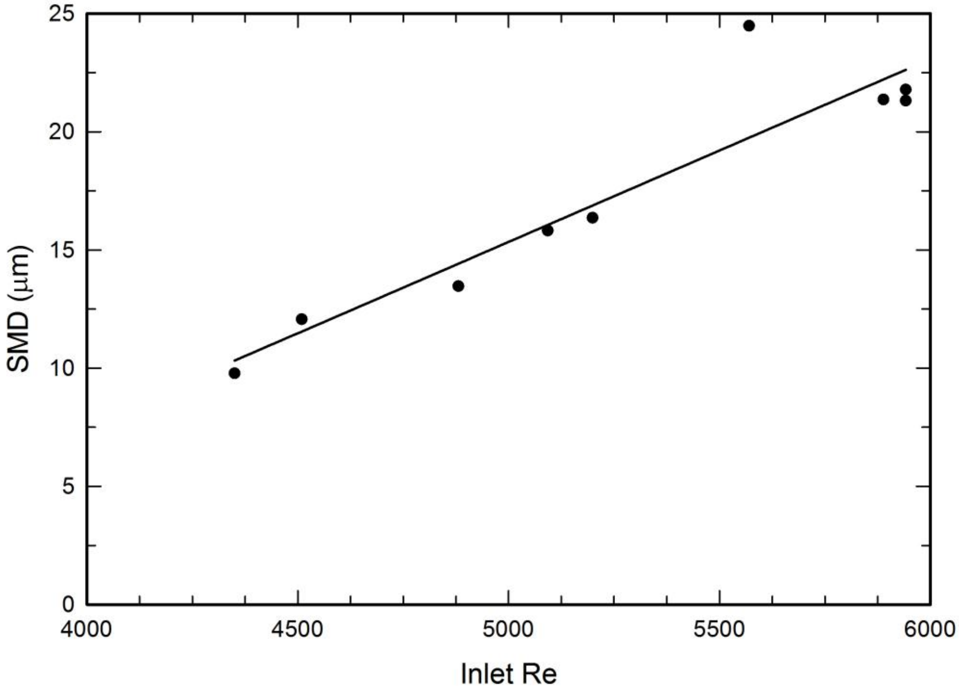

Figure 3.12 Diameter variation versus throat velocity measured FBRM for ASW

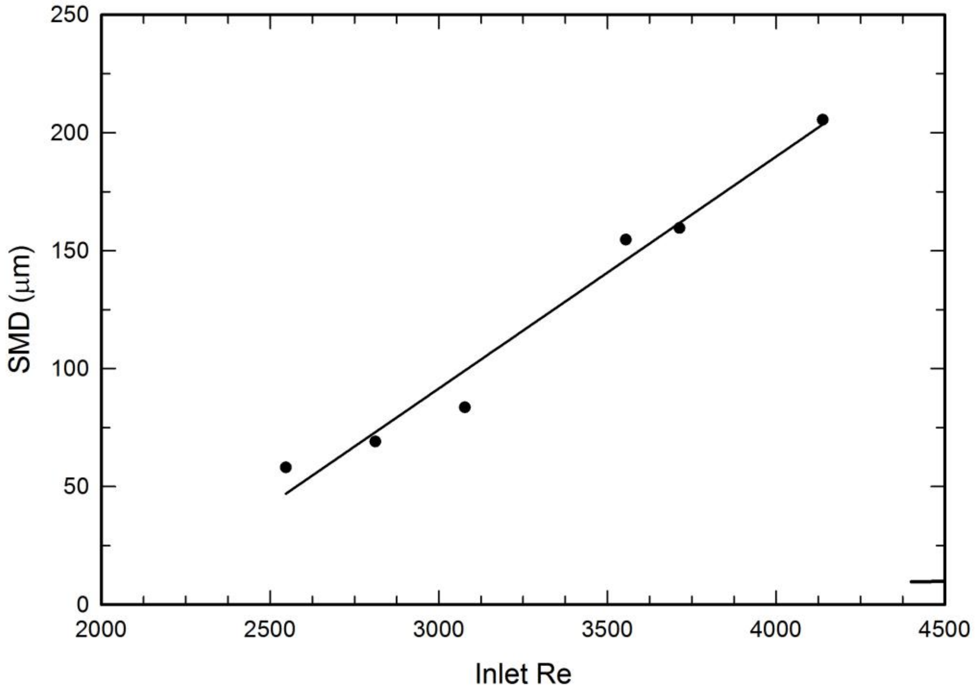

Figure 3.13 Diameter variation versus throat velocity measured FBRM for CSW

The changes of radius versus the Re number for two cases of ASW and CSW are shown in Figure 3.12 and 3.13. These results confirm the results from the Mastersizer (Figure 3.14). Moreover, it shows that the bubbles become bigger at higher concentration of dissolved gas in water. The measurements for DGW were not possible as producing required minimum number of bubbles for measurement was difficult. The stability of the bubbles in ASW and CSW cases show that the bubbles are carrying more NCG than vapor. Therefore, their lifetime was longer than vapor nuclei which form in DGW experiments. They, also, were carried down the stream for longer time, until the NCG in the bubble diffuses back into the water. It is concluded that mass transfer plays an important role in the non DGW.

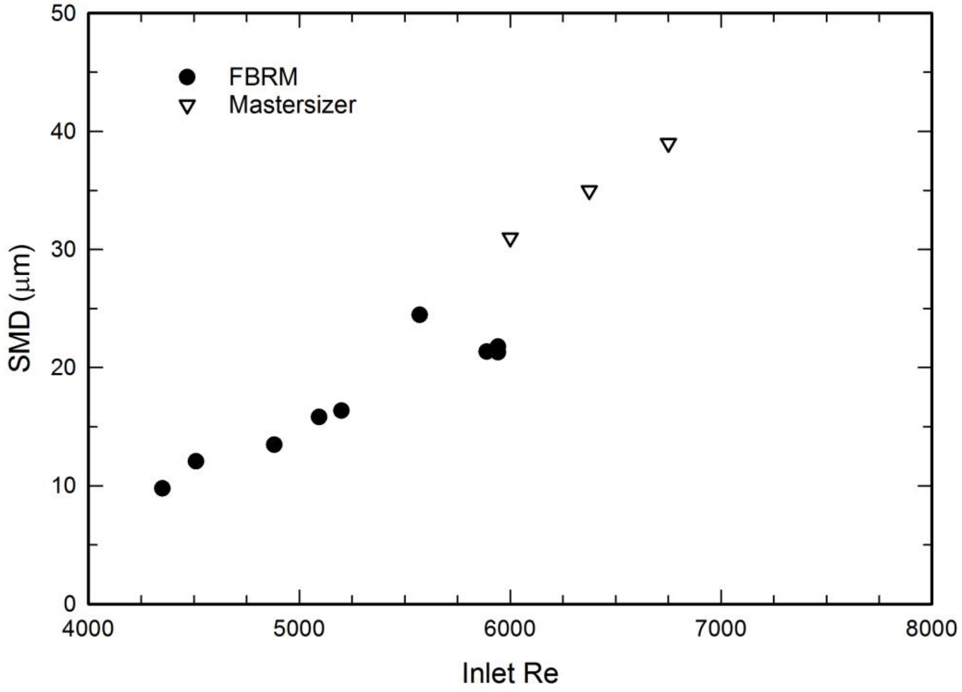

Figure 3.14 Diameter variation versus throat velocity measured FBRM and Mastersizer for ASW

3.3.4. Acoustic Bubble Spectrometer (ABS)

The ABS is a commercial acoustics based device that measures bubble size distributions and void fraction of bubbles in liquids. The device extracts the bubble population from acoustical measurements made at several frequencies. It consists of a set of two transducers/hydrophones connected to a computer. A data acquisition board controls the hydrophones' signal generation and acquisition. A software is used for setting and analyzing the signal frequency and attenuation. Signals at different frequencies are emitted from one hydrophone and are received on the other side of the bubbly flow. The attenuation and the lag time between the received signal and emitted signal are used for the calculation of the BSD and volume fraction. The instrument can provide the data in near real time. The BSD is obtained from these measurements by a solution of two Fredholm Integral

Equations of the first kind. These equations are ill-posed and challenging to solve (especially when the data has noise).[1]

A new dimensions for the venturi (Figure 3.15) was designed to be able to fit the probe (two hydrophons-blue box) (Figure 3.16) in a 6 mm ID piping. The venturi was machined from plexiglass for better accuracy of geometry. The probe was placed right after the venturi to measure the BSD of bubbles formed from cavitation. The bubbles would flow through a pipe segment through the box, and the hydrophones were placed as the pipe wall, and did not affect the flow significantly. Flanges were used to hold the venturi and ABS probes together and meanwhile the ability of changing the venturi design if required.

In all cases of cavitating flow experiments, the signals that were received were noisy and the software algorithm was not able to analyze the signals, and most of signals were dropped as unusable results. The issue was identified as the noise produced by the bubbles collapsing by the vendor. Different solutions were examined to eliminate the noise, such as locating the ABS probe at a bigger distance, from the venturi. However, the noisy signals caused the signals being dropped by the software. The issue remains and no solution was found to the problem up to date. However, if the issue is solved, ABS or acoustic systems could be the most appropriate option for the measurements of the BSD and volume fraction for the cavitating flows in venturi or other cavitation tubes.

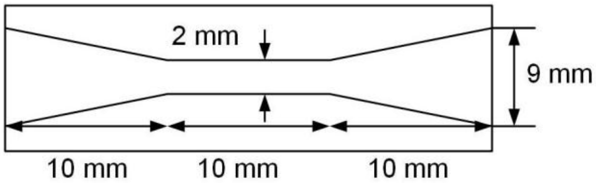

Figure 3.15 New venturi dimensions

---

[1] http://www.dynaflow-inc.com/Products/ABS/Acoustic-Bubble-Spectrometer.htm

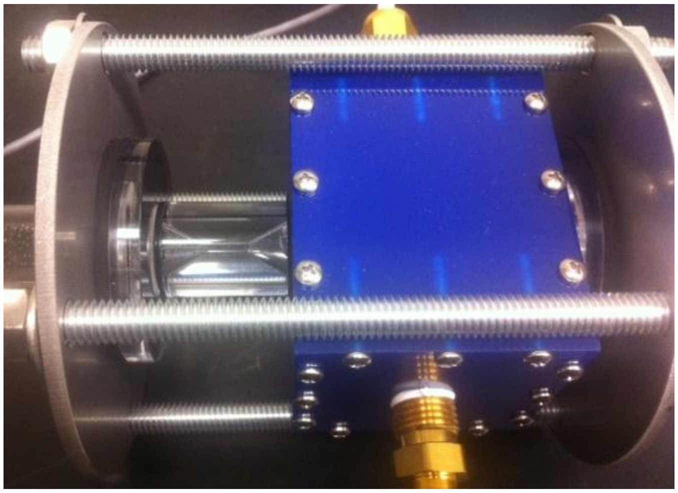

Figure 3.16 Probe box of the ABS and venturi together

3.4. Summary

In this chapter, first, a set of experiments were conducted to investigate the cavitation inception at different scales. From the preliminary experiments, it was concluded that the amount of dissolved gas in the liquid has a significant effect in the behavior of cavitation phenomena. In another set of experiments, the effect of dissolved gas on the cavitation inception in a venturi for DGW, ASW, and CSW was studied. It was found that the cavitation inception Re number in the studied venturi, decreases significantly with the increase of concentration of NCG in the liquid, i.e. cavitation occurs at lower Re number for higher gas content in the liquid. Ward et al. (1970) showed that the NCG can affect the threshold of the bubble nucleation in water, thermodynamically. He included the effect of NCG into the classical nucleation model. In the next chapter, a cavitation model is developed, and these effects are studied.

In the other set of experiments, for measuring the bubble size distribution, SMD, and void fraction, various methods and commercial devices were tested such as, light intensity measurements method, Mastersizer, FBRM. Our intention was to estimate the bubble size distribution downstream of nucleation site and the effect of dissolved gases on the nucleation rate and nuclei size. Due to difficulty of this problem, different approaches were implemented for comparison. Light transmission method provided the ratio of void fraction over SMD in the measurement volume. The advantage of this method was that it could be used close to the nucleation site. Mastersizer provided the bubble size distribution and the volume fraction of the bubbles with high accuracy (1%). However, the changes in flow pattern might result in change of size distribution originated from the venuri due to coalescence. Moreover, to gain the high accuracy, the volume fraction should be in a certain range. Therefore, it had limited usage in our experiments. FBRM, also, provided the size distribution, but it could not measure the total volume fraction or number density because it only measures the size of the bubbles passing close to its window, and counts the number of bubbles per second. Moreover, Acoustic Bubble Spectrometer (ABS), a device to measure BSD based on acoustic principles manufactured by Dynaflow Inc., was tested for in-situ measurement of BSD. However, the device was not capable of measuring the BSD because of the noise from collapsing bubbles interfering with the acoustic signals emitted from the device in the flow.

Although the SMD measurements from FBRM and Mastersizer are slightly different, the increase of SMD due to increase in velocity is consistent in both measurements. This finding is in contrast to the findings from Li (2014). This difference can be due to the different method of sampling in this study. The results of these experiments are used in chapter 5 for comparison with modeling results.

Chapter 4

Cavitation Model Development

In this chapter, all of the different models that were used in the CFD modeling are discussed. A commercial software package, Ansys (v. 16) Fluent, was used as a framework for turbulent, multiphase and population balance modeling in this study. When new models not available in Fluent were required for the cavitation modeling, User Defined Functions (UDF) were implemented for modifications. ICEM, a commercial geometry design and meshing software by ANSYS, was used for geometry and mesh construction. A structured mesh was used in this study due to its advantages such as low artificial diffusion imposed on the system, and appropriate refinement of the mesh close to the walls.

Cavitation flows, as discussed in Chapter 2, were treated as a two-phase flow including the continuous liquid phase and the dispersed gas phase in the form of bubbles or cavities. The liquid phase was modeled using the conservation equations, including mass and momentum conservation equations, followed by turbulence closure models. The gas phase was modeled with different approaches including Eulerian or Lagrangian approach. In the Eulerian approach, the bubbles' properties, usually number density and size, were solved for each cell using extra transport equations. In the Lagrangian approach, the liquid phase was solved using the Eulerian approach, and the gas phase was modeled as spherical shapes, discrete bubbles, carried by the liquid phase.

In the Lagrangian approach, the two phases can be coupled via one-way, two-way, or four-way coupling. In the Eulerian approach, the liquid and gas phase were coupled all the time using different multiphase models such as the mixture model. In the Lagrangian approach, one-way coupling includes the solution of the conservation equations for the liquid phase and the application of the effect of liquid phase on the motion of the bubbles in the gas phase. This method is suitable for the case that the effect of gas phase on the liquid phase and the interaction of components in the gas phase are negligible. Two-way coupling, extra to one-way coupling, accounts for the interaction of the gas phase bubbles on the liquid phase. In four-way coupling all the interactions of the liquid phase on the gas phase, the gas phase on the liquid phase, and the bubble-bubble interactions are considered. Each coupling mode is valid for a limited range of concentration and bubble size. In most cases, the Lagrangian approach uses one-way coupling. However, if the system requires higher order coupling, two-way or four-way coupling can be used. The computational effort increases considerably from one-way to two-way and four-way coupling.

Three models for cavitation were investigated in this study. First, Singhal cavitation model (Singhal et al., 2002) was implemented. To date, this is the only proposed model that considers the effect of Non-Condensable Gas (NCG) in the cavitation model. This model can predict the vapor volume fraction. Second, in an attempt to model the Bubble Size Distribution (BSD) alongside the cavitation, Population Balance Model (PBM) was used and the bubble interaction models i.e. coalescence, breakage, nucleation, and growth terms, of different models in literatures were implemented. Using PBM, the vapor volume fraction, BSD, and Sauter Mean Diameter (SMD) could be calculated. In the third model, Discrete Bubble Model (DBM), the bubbles were tracked in a cavitating flow using the Lagrangian approach, which is a Discrete Phase Model (DPM) in Fluent. Beside the bubble dynamics and interaction models, the bubble interaction with walls was also considered.

In the next section, the governing equations and model development for the three mentioned models are discussed.

4.1. Singhal cavitation model

The cavitation model proposed by Singhal et al. (2002) gives an estimation of the mass exchange rate between the liquid and gas phase due to cavitation using a simplified Rayleigh-Plesset equation. The flow is modeled using multiphase mixture model and a source/sink term is used in vapor phase transport equation. Mass and momentum conservations and turbulence models for the mixture and the transport equation for vapor phase volume fraction are shown below.

4.1.1. Conservation equations

The continuity and Navier-Stokes equations are used for mass and momentum conservation of the liquid phase. Although the liquid phase is assumed to be incompressible, the cavitating flow can be treated as a compressible flow by accounting for the compressibility in the gas phase. The mixture model was implemented as a multiphase model, where the properties of the gas-liquid mixture are calculated based on the volume fraction of each phase. The continuity and Navier-Stokes equations for the mixture are shown in Eq. 4.1 to 4.4.

$$\frac{\partial}{\partial t}\left(\rho_m\right)+\nabla.\left(\rho_m\vec{v}_m\right)=0 \tag{4.1}$$

$\vec{v}_m$ is the mixture velocity as, and ρ_m is the mixture density defined as:

$$\rho_m=\sum\nolimits_{k=1}^{n}\alpha_k\rho_k \tag{4.2}$$

α_k is the volume fraction of phase k.

$$
\begin{aligned}
&\frac{\partial}{\partial t}\left(\rho_m \vec{v}_m\right)+\nabla.\left(\rho_m \vec{v}_m \vec{v}_m\right)=-\nabla p \\
&\qquad +\nabla.\left(\mu_m\left(\nabla \vec{v}_m+\nabla \vec{v}_m^T-\frac{2}{3}\left(\nabla.\vec{v}_m\right) I\right)\right)+\rho_m \vec{g}+\vec{F}
\end{aligned}
\tag{4.3}
$$

μ_m is mixture viscosity and is calculated as:

$$
\mu_m=\sum\nolimits_{k=1}^{n} \alpha_k \mu_k \tag{4.4}
$$

F is the force imposed on the fluid from any external forces such as bubbles, and n is the number of phases i.e. three in this model including liquid phase, vapor phase, and NCG phase.

4.1.2. Realizable k-ε turbulence model

The *k-ε* model is one of the Reynolds Average Navier-Stokes (RANS) turbulence models based on the eddy-viscosity theory. In RANS models, the instantaneous velocity is separated into average velocity term, and velocity fluctuations:

$$
v_i=\bar{v}_i+v_i' \tag{4.5}
$$

Combining Eq. 4.3 and 4.5 the Navier-Stokes equations in Einstein notation will be:

$$
\begin{aligned}
&\frac{\partial}{\partial t}\left(\rho \bar{v}_i\right)+\frac{\partial}{\partial x_j}\left(\rho \bar{v}_i \bar{v}_j\right)=-\frac{\partial \bar{p}}{\partial x_i}+\frac{\partial}{\partial x_j}\left[\mu\left(\frac{\partial v_i}{\partial x_j}+\frac{\partial v_j}{\partial x_i}-\frac{2}{3} \delta_{ij} \frac{\partial v_l}{\partial x_l}\right)\right] \\
&\qquad +\frac{\partial}{\partial x_j}\left(-\rho \overline{v_i' v_j'}\right)+\rho \vec{g}+\vec{F}
\end{aligned}
\tag{4.6}
$$

The bar sign represents the mean value and $-\rho v_i' v_j'$ is the Reynolds Stress tensor. This stress tensor, average of random turbulent fluctuations, is needed for turbulence closure model.

In the *k-ε* model the Reynolds Stress term is written as:

$$-\rho\overline{v_i'v_j'} = \mu_t\left(\frac{\partial\overline{v_i}}{\partial x_j}+\frac{\partial\overline{v_j}}{\partial x_i}\right) \tag{4.7}$$

μ_t is turbulent viscosity, and is related to the turbulent kinetic energy, *k*, and energy dissipation rate, ε, computed as

$$\mu_t = \rho C_\mu \frac{k^2}{\varepsilon} \tag{4.8}$$

k-ε model uses two transport equations for two new variables i.e. turbulent kinetic energy (*k*) and energy dissipation rate (ε) shown in Eq. 4.8.

$$\frac{\partial}{\partial t}(\rho k)+\frac{\partial}{\partial x_j}(\rho k v_j)=\frac{\partial}{\partial x_j}\left[\left(\mu+\frac{\mu_t}{\sigma_k}\right)\frac{\partial k}{\partial x_j}\right]+2\mu_t S_{ij}S_{ij}-\rho\varepsilon \tag{4.9}$$

$$\begin{aligned}\frac{\partial}{\partial t}(\rho\varepsilon)+\frac{\partial}{\partial x_j}(\rho\varepsilon v_j)&=\frac{\partial}{\partial x_j}\left[\left(\mu+\frac{\mu_t}{\sigma_\varepsilon}\right)\frac{\partial \varepsilon}{\partial x_j}\right]\\&\quad+C_{1\varepsilon}\frac{\varepsilon}{k}\left(2\mu_t S_{ij}S_{ij}\right)-C_{2\varepsilon}\rho\frac{\varepsilon^2}{k}\end{aligned} \tag{4.10}$$

Where σ_k, σ_ε are turbulent Prandtle numbers for *k* and ε with values of 1 and 1.3 respectively, and $C_{1\varepsilon}$, $C_{2\varepsilon}$, C_μ are constants with the values of 1.44, 1.92, and 0.09.

The realizable *k-ε* model is similar to the standard *k-ε* with two modifications in the calculation of turbulent viscosity and energy dissipation rate (ε). In the realizable *k-ε* model C_μ is not constant and is computed by:

$$C_\mu = \frac{1}{A_0 + A_S\dfrac{kU^*}{\varepsilon}} \tag{4.11}$$

$$U^* = \sqrt{S_{ij}S_{ij}} \tag{4.12}$$

A_0 and A_S are model constants. The second modification is a new formula for dissipation, as follows:

$$\frac{\partial}{\partial t}(\rho\varepsilon)+\frac{\partial}{\partial x_j}(\rho\varepsilon v_j)=\frac{\partial}{\partial x_j}\left[\left(\mu+\frac{\mu_t}{\sigma_\varepsilon}\right)\frac{\partial\varepsilon}{\partial x_j}\right] \\ +\rho C_1 S_{ij}\varepsilon-\rho C_2\frac{\varepsilon^2}{k+\sqrt{\nu\varepsilon}} \tag{4.13}$$

Where σ_k, σ_ε are turbulent Prandtle numbers for k and ε with values of 1 and 1.2 respectively, and C_1 and C_2 are constants with the values of 1.44 and 1.9. These modifications improve the standard *k-ε* to give better performance in the prediction of separated flows and recirculation.

In turbulence models, wall treatment model and grid resolution near wall are key parameters for predicting a correct velocity profile in the viscous sublayer and buffer layer near the wall, and consequently in the entire domain. There are two approaches for predicting the velocity profile near the wall, i.e. near-wall model and wall functions (Eq. 4.14). In near-wall model, the turbulence model is modified to enable viscosity affected region to be resolved with a mesh up to the wall, which consequently needs a very fine mesh near the wall. In the other approach, a wall function (law of wall) is used to calculate the velocity of the first mesh in the turbulent region (y^+>30). In this study, enhanced wall treatment was implemented as a near-wall treatment model. This model switches between the two mentioned approaches based on the y^+ of the mesh.

$$v^+=\frac{1}{k}\ln y^+,\ \text{with}\ y^+=\frac{yv_\tau}{\nu},\ v^+=\frac{v}{v_\tau},\ v_\tau=\sqrt{\frac{\tau_\omega}{\rho}} \tag{4.14}$$

where τ_ω is the wall shear stress and k is Von Karman constant . If the y^+ is close to 1 (y^+<5), the model solves the viscous sublayer and buffer layer. If the y^+ is larger than 30, wall function is used to calculate the velocity for first mesh near the wall. This model uses a blended function of two function of u^+ versus y^+ for the mesh between the viscous layer and turbulent region shown below

$$v^+=e^{\Gamma}v^+_{lam}+e^{1/\Gamma}v^+_{turb} \tag{4.15}$$

In this study the y^{+} is managed to be in the range 30-40 to be in fully turbulent region unless mentioned.

4.1.3. Singhal cavitation model

In the Singhal and other cavitation models, cavitation is treated as a mass exchange between the liquid and gas phase. Therefore, a new transport equation for the vapor volume fraction is implemented to calculate the volume fraction of vapor and liquid in the domain. Cavitation models introduce estimates for source and sink terms in this transport equation as:

$$\frac{\partial}{\partial t}\left(\alpha_v \rho_v\right)+\nabla .\left(\alpha_v \rho_v \vec{v}_v\right)=R_e-R_c \tag{4.16}$$

R_e and R_c are called evaporation and condensation rates. The Rayleigh-Plesset (RP) equation is used to estimate the evaporation and condensation rates. Combining three continuity equations for liquid, vapor and mixture phase the following relationship is obtained:

$$\frac{D\rho}{Dt}=-\left(\rho_l-\rho_v\right)\frac{D\alpha}{Dt} \tag{4.17}$$

α is the vapor volume fraction and can be written as

$$\alpha=n\times\left(\frac{4}{3}\pi\Re_B^3\right) \tag{4.18}$$

where $\Re_B$ is the bubble radius. Substituting Eq. 4.18 into 4.17 yields

$$\frac{D\rho}{Dt}=-\left(\rho_l-\rho_v\right)\left(n4\pi\right)^{\frac{1}{3}}\left(3\alpha\right)^{\frac{2}{3}}\frac{D\Re_B}{Dt} \tag{4.19}$$

The Rayleigh-Plesset (R-P) equation is:

$$\Re_B\frac{D^2\Re_B}{Dt^2}+\frac{3}{2}\left(\frac{D\Re_B}{Dt}\right)^2=\left(\frac{P_B-P}{\rho_l}\right)-\frac{4\nu_l}{\Re_B}\Re_B-\frac{2\sigma}{\rho_l\Re_B} \tag{4.20}$$

where σ is surface tension, P_B is bubble pressure, and P is liquid far-field pressure. In most of cavitation models such as the Singhal model, the second derivative, viscous and surface tension terms are neglected, which is an acceptable assumption for bubble growth. Another assumption in these models is that the bubble pressure is always equal to the equilibrium vapor pressure. Therefore, the rate limiting step for bubble growth due to cavitation is the inertia and motion of the bubble wall. The remaining terms, shown below, are used to estimate the bubble radius changes.

$$\frac{D\Re_B}{Dt} = \frac{2}{3}\sqrt{\frac{P_v - P}{\rho_l}} \tag{4.21}$$

Substituting Eq. 4.21 and Eq. 4.19 into vapor phase continuity equation following equation for phase change rate is derived:

$$R_e = \frac{3\alpha}{\Re_B}.\frac{\rho_v\rho_l}{\rho}\left[\frac{2}{3}\frac{P_v - P}{\rho_l}\right]^{1/2} \tag{4.22}$$

Singhal et al (2002) used an empirical estimation for $\Re_B$ (Markatos and Singhal, 1982), as follows:

$$\Re_B = \frac{0.061\mathrm{We}\sigma}{2\rho_l v_{rel}^2} \tag{4.23}$$

with other estimations for the relative velocity, and derived the following full cavitation model for rate of evaporation and condensations:

$$R_e = C_e\frac{\sqrt{k}}{\sigma}\rho_v\rho_l\left[\frac{2}{3}\frac{P_v - P}{\rho_l}\right]^{1/2}\left(1 - f_v - f_g\right) \tag{4.24}$$

$$R_c = C_c\frac{\sqrt{k}}{\sigma}\rho_l\rho_l\left[\frac{2}{3}\frac{P - P_v}{\rho}\right]^{1/2} f_v \tag{4.25}$$

where k is turbulent kinetic energy, f_v and f_g are the mass fractions of vapor and non-condensable gases. C_e and C_c are the evaporation and condensation constants, and are valued to 0.02 and 0.01, respectively, based on various experiments conducted by Singhal et al. (2002). The corrected vapor pressure to account the effect of turbulence on the cavitation is proposed as following

$$P_v = P_{sat} + 0.195\rho k \tag{4.26}$$

The effect of NCG is reflected in the mixture density by the following equation:

$$\frac{1}{\rho} = \frac{f_v}{\rho_v} + \frac{f_g}{\rho_g} + \frac{1 - f_v - f_g}{\rho_l} \tag{4.27}$$

where ρ_g is the density of NCG and is calculated as:

$$\rho_g = \frac{MP}{RT} \tag{4.28}$$

where M is the molecular weight of the NCG, R is the ideal gas constant, and T is the temperature. Moreover, the volume fractions of NCG and liquid are modified as:

$$\alpha_g = f_g \frac{\rho}{\rho_g}, \alpha_l = 1 - \alpha_v - \alpha_g \tag{4.29}$$

4.2. Population Balance Model (PBM)

Singhal model assumes a constant diameter for the bubbles in a cell and a constant number density of bubbles per volume. To study the bubble size distribution of the domain in more detail, PBM can be implemented. In this model, a particle state vector is defined which includes a set of external coordinates $(\vec{r})$, which denote the spatial position of the bubble, and some internal coordinates (ϕ), which include different properties of the bubble, such as volume, etc. Using these coordinates, a number density function can be defined for each cell as $n(\vec{r}, \phi, t)$. The average number of bubbles in a cell of volume $dV_{\vec{x}} dV_{\phi}$ is $n(\vec{r}, \phi, t) dV_{\vec{x}} dV_{\phi}$. Therefore, the total number of bubbles per unit volume is

$$N(\vec{r},t) = \int_{\Omega_\phi} n dV_\phi \tag{4.30}$$

and the total volume fraction of all the bubbles is

$$\alpha(\vec{r},t) = \int_{\Omega_\phi} n V_{(\phi)} dV_\phi \tag{4.31}$$

where $V_{(\phi)}$ is the volume of the bubble in state of ϕ. In this model ϕ is the bubble volume.

4.2.1. Liquid/gas phase modeling

In PBM, Eulerian multiphase model is implemented, i.e. there are two mass and momentum conservation equations for each phase. The continuity equation for phase *q* is:

$$\frac{\partial}{\partial t}\left(\alpha_q \rho_q\right) + \nabla.\left(\alpha_q \rho_q \vec{v}_q\right) = 0 \tag{4.32}$$

where *q* can be either liquid or gas phase. For the gas phase, the density is calculated by the ideal gas law. Similarly the momentum equation for phase *q* is defined as:

$$\begin{aligned}\frac{\partial}{\partial t}\left(\alpha_q \rho_q \vec{v}_q\right) + \nabla.\left(\alpha_q \rho_q \vec{v}_q \vec{v}_q\right) &= -\alpha_q \nabla p \\ &+\nabla.\left(\alpha_q \mu_q \left(\nabla \vec{v}_q + \nabla \vec{v}_q^T - \frac{2}{3}\left(\nabla.\vec{v}_q\right) I\right)\right) \\ &+\alpha_q \rho_q \vec{g} + \left(\vec{F}_{drag,q} + \vec{F}_{lift,q} + \vec{F}_{wl,q} + \vec{F}_{vm,q} + \vec{F}_{td,q}\right)\end{aligned} \tag{4.33}$$

Where $\vec{F}_{drag,q}$ is the drag force, $\vec{F}_{lift,q}$ is the lift force, $\vec{F}_{wl,q}$ is the wall lubrication force, $\vec{F}_{vm,q}$ is the virtual mass force, and $\vec{F}_{td,q}$ is the turbulent dispersion force.

The drag force is calculated as:

$$F_{drag,q} = \frac{3}{4} C_D \alpha_g \rho_l \frac{1}{d_b} \left| v_l - v_g \right| \left(v_l - v_g \right) \quad (4.34)$$

C_D is drag coefficient and is estimated by Schiller and Naumann (1933) model

$$C_D = \begin{cases} 24\left(1 + 0.15\,\mathrm{Re}^{0.687}\right) / \mathrm{Re} & \mathrm{Re} \le 1000 \\ 0.44 & \mathrm{Re} > 1000 \end{cases} \quad (4.35)$$

where Re, is bubble Reynolds number and defined as:

$$\mathrm{Re} = \frac{\rho_l \left| v_l - v_g \right| d_b}{\mu_l} \quad (4.36)$$

Lift Force is calculated as:

$$F_{lift,q} = -C_l \alpha_q \rho_l \left(\vec{v}_l - \vec{v}_g \right) \times \left(\nabla \times \vec{v}_l \right) \quad (4.37)$$

C_l is lift coefficient and has a value of -0.2 unless mentioned.

Wall lubrication force is due to the pressure gradient effect on the bubbles close to the wall, and is modeled by Antal et al. (1991) as:

$$F_{wb,q} = C_{wl} \alpha_q \rho_l \left| \left(\vec{v}_l - \vec{v}_g \right) . \vec{n}_w \right|^2 \vec{n}_w \quad (4.38)$$

where $\vec{n}_w$ is the unit normal pointing away from wall, and C_{wl} is wall lubrication coefficient equal to:

$$C_{wl} = \max\left(0, \frac{-0.01}{d_b} + \frac{0.05}{y_w} \right) \quad (4.39)$$

where d_b is bubble diameter and y_w is the distance to the nearest wall.

Turbulent dispersion force is calculated by Lopez de Bertodano (1998) model as:

$$F_{td,q} = -C_{TD} k_l \rho_l \nabla \alpha_g \quad (4.40)$$

where k_l is the turbulent kinetic energy of the liquid phase, and C_{TD} is constant with a value of 0.1.

The virtual mass force is defined as:

$$F_{lift,q} = 0.5\alpha_g \rho_l \left(\frac{d_l \vec{v}_l}{dt} - \frac{d_g \vec{v}_g}{dt} \right) \tag{4.41}$$

where $\frac{d_q}{dt}$ denotes the phase material time derivative as

$$\frac{d_q \phi}{dt} = \frac{\partial(\phi)}{\partial t} + \left(\vec{v}_q . \nabla\right)\phi \tag{4.42}$$

The k-ε turbulence model is defined for each phase (q) separately as

$$\begin{aligned} \frac{\partial}{\partial t}\left(\alpha_q \rho_q k_q\right) + \frac{\partial}{\partial x_j}\left(\alpha_q \rho_q k_q v_{qj}\right) = \frac{\partial}{\partial x_j}\left[\alpha_q \left(\mu_q + \frac{\mu_{tq}}{\sigma_k} \right) \frac{\partial k_q}{\partial x_j} \right] \\ +2\alpha_q \mu_{tq} S_{ij} S_{ij} - \alpha_q \rho_q \varepsilon_q \end{aligned} \tag{4.43}$$

$$\begin{aligned} \frac{\partial}{\partial t}\left(\alpha_q \rho_q \varepsilon_q\right) + \frac{\partial}{\partial x_j}\left(\alpha_q \rho_q \varepsilon_q v_{qj}\right) = \frac{\partial}{\partial x_j}\left[\alpha_q \left(\mu_q + \frac{\mu_{tq}}{\sigma_\varepsilon} \right) \frac{\partial \varepsilon_q}{\partial x_j} \right] \\ +\rho_q C_1 S_{ij} \varepsilon_q - \rho_q C_2 \frac{\varepsilon_q^2}{k_q + \sqrt{\nu \varepsilon_q}} \end{aligned} \tag{4.44}$$

4.2.2. Population balance equation

For the bubble number density function, $n\left(V,t\right)$, a transport equation is defined as follows:

$$\begin{aligned} \frac{\partial}{\partial t}\left[n(V,t)\right] + \nabla . \left[n(V,t)\,\vec{v}\right] + \nabla_V . \left[G_V n(V,t)\right] = \\ B_{Co} - D_{Co} + B_{Br} - D_{Br} \end{aligned} \tag{4.45}$$

where B_{Co} is the birth rate of bubbles through coalescence, D_{Co} is the death rate by coalescence, D_{Br} is the death rate of bubbles through breakage, B_{Br} is the birth rate by breakage, and $\nabla_V.\left[G_V n\left(V,t\right)\right]$ is the growth term. G_V is the growth rate based on the bubble volume (m^3/s) defined as:

$$G_V = \frac{\partial V}{\partial t} \tag{4.46}$$

The bubble growth due to cavitation and mass diffusion can be implemented as growth term. The boundary conditions for this equation are:

$$n\left(V,t=0\right)=n_V;\mathrm{n}\left(V=0,t\right)G_V=n_0' \tag{4.47}$$

where n'_0 is the nucleation rate (1/m^3/s).

When two bubbles of volume $V\text{-}V'$ and V'¸ collide to form a bubble of volume V, it results in coalescence (Figure 4.1-a). The bubble birth rate through coalescence is expressed as:

$$B_{Co} = \frac{1}{2}\int_0^V a(V-V')n(V-V',t)n(V',t)dV' \tag{4.48}$$

The coalescence rate, $a(V\text{-}V',V')$ [1/m^{3}s], the rate of bubble coalescence due to collision between bubbles of volume $V\text{-}V'$ and V' to form a bubble of volume V is often expressed as the product of the frequency of collision between bubbles of volume $V\text{-}V'$ and V', and the coalescence probability between bubbles of volume $V\text{-}V'$ and V'.

The bubble death rate (Figure 4.1-b) through coalescence is expressed as:

$$D_{Co} = \int_0^\infty a(V,V')n(V,t)n(V',t)dV' \tag{4.49}$$

Breakage occurs as a result of shear or other forces applied to individual bubbles. These forces are the result of the nature of the flow field surrounding a bubble. The birth rate due to breakage (Figure 4.1-c) can be given as:

$$B_{Br} = \int_{\Omega_V} bg(V')\beta(V\,|\,V')n(V,t)dV' \tag{4.50}$$

where *b* is the number of bubbles generated by a breakage event, and the breakage rate *g(V')* is the breakage frequency of bubbles with volume *V'*¸ per unit time (1/m3/s). The Probability Density Function (PDF), *β(V|V')*, gives the probability of the bubbles breaking from volume *V'*¸ to a bubble of volume *V*.

The death rate due to breakage (Figure 4.1-d) is given as:

$$D_{Br} = g(V)n(V,t) \tag{4.51}$$

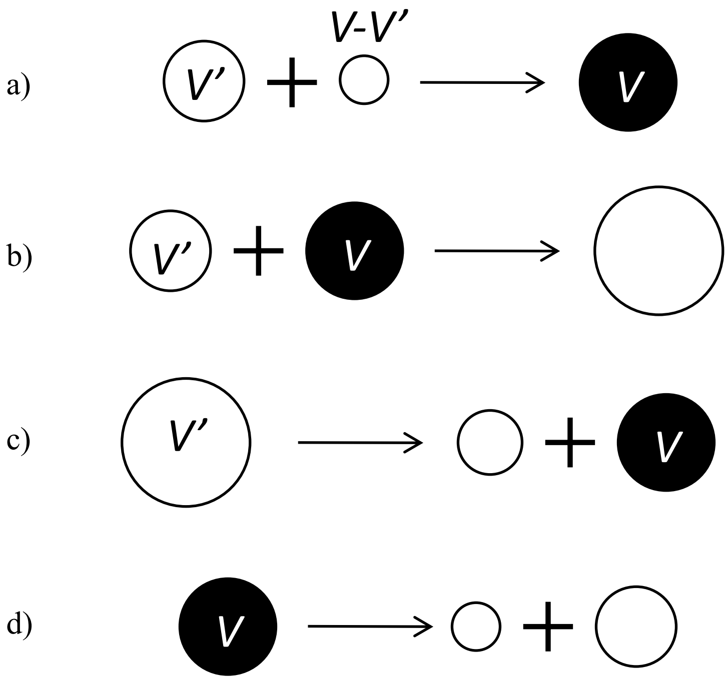

Figure 4.1 Bubbles coalescence and breakage a) birth through coalescence, b) death through coalescence, c) birth through breakage, d) death through breakage

4.2.3. Coalescence models

In general, coalescence rate of bubbles of size d_i and d_j can be expressed as:

$$c\left(d_i, d_j\right) = \omega_c\left(d_i, d_j\right)P_{coa}\left(d_i, d_j\right) \tag{4.52}$$

where ω_c is the collision rate and P_{coa} is the coalescence probability.

The collision rate is the rate of collision between bubbles of diameters d_i and d_j in a control volume with the units of ($1/m^3$.s). Coalescence probability, also known as collision efficiency, is a dimensionless parameter and is defined as the fraction of colliding bubbles resulting in coalescence. The total rate of coalescence is multiplication of these two terms. There are many different models to predict this two terms. Prince and Blanch (1990), Luo and Svenden (1996), and Kamp et al. (2001) models are explained in this section.

In most of the coalescence models, probability of the bubble coalescence in case of bubble collision is estimated based on the Coulaloglou and Tavlarides (1976) exponential function

$$P_{coa}\left(d_i, d_j\right) = \exp(-t_{ij} / \tau_{ij}) \tag{4.53}$$

where t_{ij} is the coalescence time or drainage time defined as the time needed to drain the liquid between bubbles from an initial film thickness to a final film thickness where bubbles coalesce instantly. τ_{ij} is the contact time defined as the time that bubbles are in contact with each other i.e. the bubbles distance is less than an initial film thickness.

Prince and Blanch model: Prince and Blanch (1990) modeled bubble collision rate by considering the bubble collisions due to turbulence, buoyancy, and laminar shear. The bubble collision due to turbulence is only considered in this study, as the flows are turbulence dominated in cavitation tubes. The collision rate due to turbulence is calculated based on the gas kinetic theory and the assumption that only turbulent eddies of the same size as bubbles can cause a relative motion of the mean velocity to the bubbles. Accordingly, the collision rate can be calculated by:

$$\omega_c\left(d_i, d_j\right) = 0.089\pi n_i n_j \varepsilon^{1/3}\left(d_i + d_j\right)^2\left(d_i^{2/3} + d_j^{2/3}\right)^2 \tag{4.54}$$

where n_i and n_j are the number density of bubbles with diameter d_i and d_j respectively. ε is the dissipation rate.

They also proposed an estimation of the coalescence time and contact time of a pair of bubbles. Coalescence time is based on the thinning of the liquid film between the two bubbles and is calculated by:

$$t_{ij} = \left\{ \frac{r_{ij}^3 \rho_l}{16\sigma} \right\}^{1/2} \ln \frac{h_0}{h_f} \tag{4.55}$$

where h_0 is initial film thickness (10^{-3} for air/water system), h_f is final film thickness before coalescence (10^{-6} for air/water system), σ is surface tension and r_{ij} is defined as:

$$r_{ij} = \frac{1}{2} \left(\frac{1}{r_{bi}} + \frac{1}{r_{bj}} \right)^{-1} \tag{4.56}$$

The contact time is estimated by:

$$\tau_{ij} = \frac{r_{ij}^{2/3}}{\varepsilon^{1/3}} \tag{4.57}$$

Substituting these estimations in the Coulaloglou and Tavlarides function the coalescence probability can be calculated directly by:

$$P_{coa}\left(d_i, d_j\right) = \exp\left(-\frac{r_{ij}^{5/6} \rho_l^{1/2} \varepsilon^{1/3}}{4\sigma^{1/2}} \ln \frac{h_0}{h_f} \right) \tag{4.58}$$

Luo and Svendsen model: Luo and Svendsen (1996) proposed a similar model to Prince and Blanch for bubble coalescence due to turbulence only.

$$\omega_c\left(d_i, d_j\right) = 0.354\pi n_i n_j \varepsilon^{1/3} \left(d_i + d_j\right)^2 \left(d_i^{2/3} + d_j^{2/3}\right)^2 \tag{4.59}$$

$$P_{coa}\left(d_i, d_j\right) = \exp\left(-\frac{\left[0.75\left(1+\xi_{ij}^2\right)\left(1+\xi_{ij}^3\right)\right]^{1/2}}{\left(\frac{\rho_g}{\rho_l} + 0.5\right)^{1/2} \left(1+\xi_{ij}\right)^3} We_{ij}^{1/2} \right) \tag{4.60}$$

where ξ_{ij} is the ratio of bubble sizes (d_i/d_j), and We_{ij} is Weber number defined as

$$We_{ij} = \frac{\rho_l d_i v_{ij}^2}{\sigma} \tag{4.61}$$

where

$$v_{ij} = \left(v_i^2 + v_j^2\right)^2 \tag{4.62}$$

Kamp model: Kamp et al (2001) found estimation for the interaction and drainage time of two bubbles based on the calculation of momentary kinetic energy of bubbles and the deformation of the bubbles in a surfactant free environment as surfactants can cause the immobile interfaces due to the charge distribution (Dai et al., 2000). When two bubbles collide they start to deform and the kinetic energy is used for the deformation of the bubble from spherical shape as shown in Figure 4.2. Later, this deformation in a form of potential energy will convert to kinetic energy repelling the bubbles from each other.

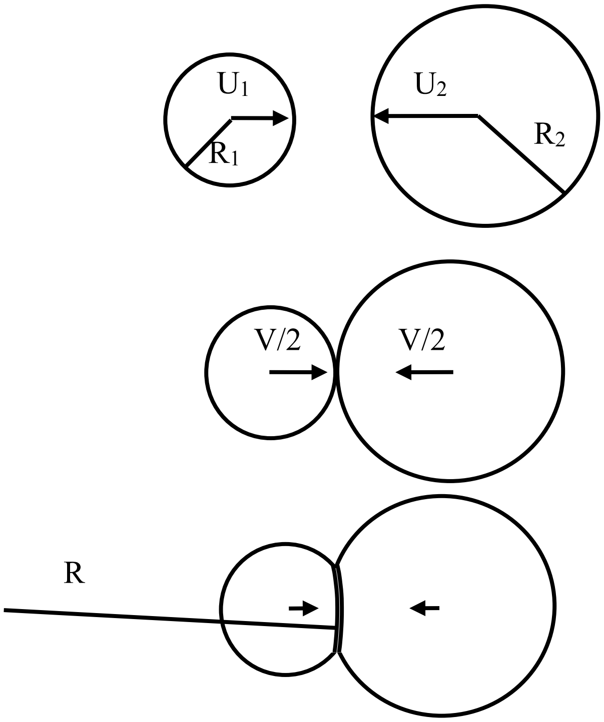

Figure 4.2 Collision of two bubbles of radius R_1 and R_2 and velocities U_1 and U_2 and formation of liquid film between the bubbles (Kamp et al., 2001)

The velocity of the bubbles is calculated based on the bubbles distance and radius, and is integrated over the displacement of the bubble from the touching point to the separation point to find the interaction time as:

$$t_i = \frac{\pi}{4}\left(\frac{\rho_L C_{vm} d_{eq}^3}{3\sigma}\right)^{1/2} \tag{4.63}$$

The drainage time, estimated by the integration of the changes of film liquid thickness over time, is:

$$t_d = \frac{\rho_L V_0 d_{eq}^2}{8\sigma} \tag{4.64}$$

Therefore, the ratio of t_d/t_i is calculated by:

$$\frac{t_d}{t_i} = \frac{k_1}{2\pi}\left(\frac{3\rho_L V_0^2 d_{eq}}{C_{vm}\sigma}\right)^{1/2} \tag{4.65}$$

where the C_{vm} is a virtual mass coefficient, ρ_L is the liquid density, V_0 is the relative velocity of the bubbles towards each other (approach velocity), and d_{eq} is the diameter of the interface between the bubbles, and is equal to:

$$d_{eq} = \frac{2d_1 d_2}{d_1 + d_2} \tag{4.66}$$

where d_1 and d_2 are the diameter of the bubbles approaching. C_{vm} is calculated as:

$$C_{vm} = \frac{L'N' - M'^2}{L' - 2M' + N'} \frac{1}{d_{eq}^3} \tag{4.67}$$

where L', M', and N' are calculated by:

$$L' = \frac{12L_0}{\pi\rho_L} = d_1^3\left(1 + \frac{3d_2^3}{\left(d_1 + 2d_2\right)^3} + \frac{3d_2^3}{\left(2d_1 + 3d_2\right)^3}\right) \tag{4.68}$$

$$M' = \frac{12M_0}{\pi\rho_L} = \frac{d_1^3 d_2^3}{\left(d_1 + d_2\right)^3}\left(\frac{251}{72}\right) \tag{4.69}$$

$$N' = \frac{12N_0}{\pi\rho_L} = d_2^3\left(1 + \frac{3d_1^3}{\left(2d_1 + d_2\right)^3} + \frac{3d_1^3}{\left(3d_1 + 2d_2\right)^3}\right) \tag{4.70}$$

The value of the constant, k_1, was estimated to be 2.5 by the data from a bubble bouncing a water/air flat surface.

In PBM modeling, as the approach velocity information is not available for each pair of bubbles, a statistical estimation should be implemented. Kamp et al. (2001) used similar estimation for the bubble turbulent motion as Prince and Blanch (1990), and Luo and Svendsen (1996) models as:

$$V_{(d_1,d_2)} = 1.25 C_t \varepsilon^{1/3}\left(d_1 + d_2\right)^{1/3} \tag{4.71}$$

where C_t is the ratio of bubble velocity fluctuations to the fluid velocity fluctuations and has been modeled as:

$$C_t^2 = \frac{9 + 43.2\nu_l l_e / d_{eq}^2 v'}{1 + 43.2\nu_l l_e / d_{eq}^2 v'} \tag{4.72}$$

where ν_l is the kinematic viscosity of the liquid, v' is the r.m.s value of the streamwise liquid velocity, l_e is turbulent length scale, and d_{eq} is calculated by Eq. (4.65). L_e/u' can be estimated as:

$$\frac{l_e}{v'} = \frac{C_\mu^{3/4}\dfrac{k^{3/2}}{\varepsilon}}{\sqrt{\dfrac{2k}{3}}} = 0.201\frac{k}{\varepsilon} \tag{4.73}$$

Therefore, the coalescence probability is calculated by:

$$P_{coa}\left(d_i, d_j\right) = \exp\left(-\frac{t_d}{t_i}\right) = \exp\left(-\frac{2.706 C_t}{\sqrt{\pi}}\left(\frac{\rho_L d_{eq}}{C_{vm}\sigma}\right)^{1/2} \varepsilon^{1/3}\left(d_1 + d_2\right)^{1/3}\right) \tag{4.74}$$

And the collision frequency is calculated as:

$$\omega_c\left(d_i,d_j\right)=1.02\sqrt{\pi}n_i n_j \varepsilon^{1/3}\left(d_i+d_j\right)^{2/3} \tag{4.75}$$

4.2.4. Breakage models

Bubble breakage can occur due to turbulence fluctuations and bubble surface instability. For large bubbles, bigger than a few millimeters the bubble cannot maintain its spherical shape and it is possible that the bubble breaks into smaller bubbles. Bubble breakage due to turbulence is more frequent in cavitation tubes, due to the small size of the bubbles and high intensity of turbulence in the flow regime.

Breakage models include two functions, breakage frequency and daughter Probability Distribution Function (PDF), to model the bubble breakage. The breakage frequency is the rate of breakage occurrence for a bubble in a turbulent flow. The daughter PDF is used to estimate the daughter bubble sizes as a result of mother bubble breakage.

The breakage model used in this study is Laakkonen model (2006), which is a model that originated from a work by Narsimhan et al. (1979) and developed by Alopaeus et al. (2002). The breakage frequency is calculated by

$$g\left(V'\right)=C_1\varepsilon^{1/3}erfc\left(\sqrt{C_2\frac{\sigma}{\rho_l\varepsilon^{2/3}d^{5/3}}+C_3\frac{\mu_l}{\sqrt{\rho_l\rho_g}\varepsilon^{2/3}d^{5/3}}}\right) \tag{4.76}$$

where ε is the liquid phase eddy dissipation, σ is the surface tension, ρ_l is the liquid density, ρ_g is the gas density, d is the parent particle diameter and μ_l is the liquid viscosity. The constants C_1,C_2, C_3 are 2.52, 0.04, and 0.01, according to the experiments by Laakkonen et al (2006) in a stirred mixer.

The daughter PDF for binary breakage is given by:

$$\beta(V,V') = \frac{30}{V'}\left(\frac{V}{V'}\right)^2 \left(1-\frac{V}{V'}\right)^2 \tag{4.77}$$

where *V* and *V'* are the daughter and parent bubble volumes, respectively.

4.2.5. Mass transfer model

In liquid with various amounts of NCG dissolved, the gas diffusion through the bubble interface can be important and effective on the cavitation inception and BSD. The growth model is used to capture the mass transfer between the bubble and the liquid due to the gas diffusion of the NCG in PBM. Modeling mass diffusion for a cavitating bubble in a flowing liquid is a very difficult subject. At each stage of bubble life, mass transfer rate is controlled dominantly by different phenomena. For example, for a single stationary bubble in infinite liquid domain, assuming small amount of gas dissolved in the liquid, the mass transfer rate for the gas is limited with the rate of gas diffusion in the liquid toward the bubble wall, and it can be assumed that the gas concentration inside the bubble is uniform. In this case, the gas diffusion can be modeled using Fick's law in one dimension to model the gas diffusion.

In another case, where a bubble, with a radius of R_b, is in flowing liquid, the mass transfer rate is limited to the rate of mass diffusion in a boundary layer around the bubble. In this case, the mass transfer can be modeled based on the Higbie penetration theory (Venneker et al., 2002). In this theory, packages of liquid from bulk are introduced to the bubble surface due to motion for a period of exposure time on the bubble. Then, they are transferred to the bulk liquid, and replaced by a new package of fresh water. The mass transfer coefficient and rate, using this theory, can be estimated as:

$$\frac{dm}{dt} = \rho\frac{dV}{dt} = k_{Diff}A\left(P_0 - P_l\right)HM_W + k_{Vap}A\left(P_v - P_l\right) \tag{4.78}$$

where k_{Diff} and k_{Vap} are the mass transfer coefficients. P_0 is the saturation pressure of the water with the NCG. P_l is the local liquid pressure. P_v is the vapor pressure. For diffusion of NCG into the bubble, k_l can be calculated as:

$$k_{Diff} = 0.301\mathrm{Sc}^{-1/2}\left(\varepsilon\nu\right)^{1/4} = 0.301\sqrt{C_{Diff}}\left(\frac{\varepsilon}{\nu}\right)^{1/4} \tag{4.79}$$

A is the bubble surface area, H is Henry constant, M_W is the gas molecular weight, ΔC is the concentration difference between the bulk liquid and the gas concentration at the bubble surface in the liquid phase, which is related to the pressure inside the bubble and saturation pressure of liquid. Sc is the Schmidt number, C_{Diff} is the gas diffusion coefficient in the liquid phase, ε is the energy dissipation rate, v is the kinematic viscosity of the liquid. In this model the motion of the bubble wall is neglected. k_{Vap} is calculated as:

$$k_{Vap} = \sqrt{\frac{M}{2\pi RT}} \tag{4.80}$$

R is universal gas constant, and T is the temperature. The derivation of the total mass transfer rate is explained in Appendix I. For vapor condensation, because of lower value of volume fraction for vapor compared to NCG, a limiting coefficient is used as:

$$k_{Vap,condensation} = k_{Vap} \times \frac{P_v}{P_0 + P_v} \tag{4.81}$$

4.2.6. Nucleation model

There are many studies that show that the classical nucleation model is unable to predict the proper rate of bubble nucleation by many orders of magnitude. This is explained as a result of existence of water impurities such as solid particles, gas cavities which decrease the free energy needed for nucleation. These impurities are hard to be removed, and they exist even in distilled waters. Very extra care is needed in cleaning the container surface and water purification. Despite the classical nucleation model, Singhal cavitation rate, which is tuned based on the experiments, can be used as a proper estimation for the nucleation rate.

Nucleation rate (1/s) is calculated from the Singhal evaporation rate as:

$$R_N = C_e \frac{\sqrt{k}}{\sigma} \rho_l \left[\frac{2}{3} \frac{P_v - P}{\rho_l} \right]^{1/2} \frac{(1 - f_v)}{\rho_b V_b^0} \tag{4.82}$$

V_b^0 is the volume of the smallest bin. In PBM, the nucleation of new bubbles was used as a boundary condition for the smallest bubbles bin.

4.2.7. Solution method

There are different methods to solve the PB equation such as Monte Carlo method, discrete method, and Method of Moment (MOM). In this study, the discrete method was implemented. In this method, the total range of bubble sizes are divided into smaller bins, and PB equation is written and solved for each size bin. This method is computationally expensive because for each bin a transport equation should be solved. To achieve a good result for bubble size distribution (BSD) the number of bins needs to be sufficiently large. In most applications, depending on the range of bubble sizes, more than 10 bins is required for this method. The advantage of this method is that the bins can be defined by users and exact size distribution will be available for each computational cell.

In Fluent, the PBE is written in terms of volume fraction of bubble size *i* as

$$\begin{aligned} &\frac{\partial}{\partial t}\left(\rho_g \alpha_i\right) + \nabla.\left(\rho_g u_i \alpha_i\right) + \frac{\partial}{\partial V}\left(\frac{G_V \rho_g \alpha_i}{V}\right) = \\ &\qquad \rho_g V_i \left(B_{Co,i} - D_{Co,i} + B_{Br,i} - D_{Br,i}\right) + 0^i V_0 n_0' \end{aligned} \tag{4.83}$$

where ρ_g is the density of the gas phase and α_i is the volume fraction of bubble size *i*, defined as

$$\alpha_i = N_i V_i \qquad i = 0, 1, ..., \mathrm{N} - 1 \tag{4.84}$$

where

$$N_i\left(t\right)=\int_{V_i}^{V_{i+1}} n\left(V,t\right)dV \tag{4.85}$$

and V_i is volume of bubble size i, and 0^i signifies that the term $\rho_g V_0 n_0$' appears in the equation only for the smallest bubble size. The change of bubble size due to pressure is accounted by a growth term as:

$$G_V=\frac{D\rho}{Dt}=\frac{\partial\rho}{\partial t}+v_i\left(\frac{\partial\rho}{\partial x_i}\right) \tag{4.86}$$

4.3. Discrete Bubble Model (DBM)

Besides the Eulerian approach for modeling the bubble size distribution, there is a Lagrangian approach i.e. Discrete Bubble Modeling (DBM). In this model, the liquid phase is solved using the transport equation for mass, momentum and turbulent models. Bubbles are assumed as a point that is tracked in the liquid domain. Each point i.e. bubble, has its own position, velocity, and as many properties as desired, such as radius, bubble pressure, gas pressure, bubble wall velocity, etc. Using this approach, the full bubble dynamics (R-P equation), bubble-bubble interaction models (coalescence, breakage), bubble-wall interactions, and gas diffusion at the bubble interface can be modeled. There are two approaches in coupling of the liquid and gas phase in this model. One-way coupling includes the effect of liquid phase on the gas phase only. On the other hand, two-way coupling also includes the effect of existence of the gas bubbles on the liquid. The downside of this approach is the time consumption of this model in two-way coupling. As the volume fraction of the liquid is small in most of the domain, one-way coupling is used. Following is a detail of the sub-models that has been used in DBM.

4.3.1. Liquid/gas phase modeling

In DBM, one-way coupling is implemented for liquid/gas interactions. Therefore, a single phase form of mass and momentum equation is solved for liquid phase and the velocity and pressure of the liquid phase is used in determining the path of the bubbles by applying related forces to bubbles.

The continuity equation for liquid phase is:

$$\frac{\partial}{\partial t}\left(\rho_l\right)+\nabla .\left(\rho_l \vec{v}_l\right)=0 \tag{4.87}$$

The momentum conservation equation is:

$$\frac{\partial}{\partial t}\left(\rho_l \vec{v}_l\right)+\nabla .\left(\rho_l \vec{v}_l \vec{v}_l\right)=-\nabla p+\nabla .\left(\mu_l\left(\nabla \vec{v}_l+\nabla \vec{v}_l^T\right)\right)+\rho_l \vec{g}+S_{DBM} \tag{4.88}$$

where S_{DBM} is the source term inserted from the gas phase. This source term is used in two-way coupling, and is set to zero in one-way coupling. The liquid density can be modified to include the effect of non-condensable gases as mentioned before.

The realizable k-ε turbulence model with enhanced wall treatment is implemented for turbulence modeling. A source term is added to the right hand side of the each equation as follows:

$$\begin{aligned}\frac{\partial}{\partial t}\left(\rho_l k_l\right)+\frac{\partial}{\partial x_j}\left(\rho_l k_l v_{lj}\right)=&\frac{\partial}{\partial x_j}\left[\left(\mu_l+\frac{\mu_{tl}}{\sigma_k}\right)\frac{\partial k_l}{\partial x_j}\right]\\&+2\mu_{tl}S_{ij}S_{ij}-\rho_l\varepsilon_l+S_{DBM}\end{aligned} \tag{4.89}$$

$$\begin{aligned}\frac{\partial}{\partial t}\left(\rho_l \varepsilon_l\right)+\frac{\partial}{\partial x_j}\left(\rho_l \varepsilon_l v_{lj}\right)=&\frac{\partial}{\partial x_j}\left[\left(\mu_l+\frac{\mu_{tl}}{\sigma_\varepsilon}\right)\frac{\partial \varepsilon_l}{\partial x_j}\right]\\&+\rho C_1 S_{ij}\varepsilon-\rho C_2\frac{\varepsilon^2}{k+\sqrt{\nu\varepsilon}}+S_{DBM}\end{aligned} \tag{4.90}$$

The bubbles are initiated in the flow domain as required, and the velocity, position and different properties of the bubble such as density, diameter, etc. are appointed to the bubble. The motion of the bubble is then calculated as:

$$\frac{d}{dt}\left(x_b\right) = v_b \tag{4.91}$$

$$m_b \frac{d}{dt}\left(v_b\right) = \vec{F}_{lb} = \vec{F}_{drag,q} + \vec{F}_{dp,q} + \vec{F}_{vm,q} \tag{4.92}$$

where $\vec{F}_{drag,q}$ is the drag force, $\vec{F}_{dp,q}$ is the pressure gradient force, and $\vec{F}_{vm,q}$ is the virtual mass force. The drag force is calculated as:

$$F_{drag,q} = \frac{1}{8} C_D \rho_l \pi d_b^2 \left|v_l - v_b\right| \left(v_l - v_b\right) \tag{4.93}$$

where C_D is drag coefficient and is calculated as:

$$C_D = \begin{cases} 24\left(1 + 0.15\,\mathrm{Re}^{0.687}\right)/\,\mathrm{Re} & \mathrm{Re} \le 1000 \\ 0.44 & \mathrm{Re} > 1000 \end{cases} \tag{4.94}$$

where Re, is bubble Reynolds number and defined as:

$$\mathrm{Re} = \frac{\rho_l \left|v_l - v_b\right| d_b}{\mu_l} \tag{4.95}$$

Pressure gradient force is calculated as:

$$F_{dp,q} = -\frac{\pi}{6} d_b^3 \nabla P \tag{4.96}$$

Virtual mass force is defined as:

$$F_{vm,q} = 0.5 \rho_l \frac{\pi}{6} d_b^3 \left(\frac{D\vec{v}_l}{Dt} - \frac{d\vec{v}_b}{dt} \right) \tag{4.97}$$

In DBM, reflect wall boundary condition is applied to the bubble when the distance of the bubble to the nearest wall is less than the bubble radius. If a bubble is touching a wall, the normal velocity of the bubble to the wall is calculated, reversed and added to the bubble velocity. Therefore the new velocity of the bubble is calculated as:

$$\vec{v}_{new} = \vec{v}_{old} + 2\left|\vec{v}_{old}.\vec{n}_{wall}\right|\vec{n}_{wall} \tag{4.98}$$

If two-way coupling (including the effect of bubbles on the liquid flow) is intended to be considered, the liquid volume fraction at each cell is calculated, and is implemented in the density and viscosity of the liquid in continuity, momentum and turbulence equations. However, in this study the flow is one-way coupled and the effect of the bubbles on the flow are neglected because in most of the region the vapor volume fraction is very small. However, the methodology, which is explained in Appendix A, can be implemented in the UDF, and is recommended for future studies

The solution of Eulerian and Lagrangian phase includes the following steps:

1. New bubbles are initiated in the domain.
2. The fluid is iterated to a converged solution at time t+ΔtE.
3. The forces on the bubbles are estimated, and time step is calculated as Δt=min(Δtmax, Δtbd, τ_b), where τ_b is bubble relaxation time, Δtbd is bubble dynamics solver time step, and Δtmax is set to 1e-7 s.
4. The bubble new position and velocity is calculated.
5. The Lagrangian steps (3-4) are repeated to reach the fluid time.
6. Steps 2-6 are repeated to the end of simulation.

4.3.2. Bubble dynamics

The dynamics of the bubble, assuming water as an incompressible liquid, can be predicted by the R-P equation as (Brennen, 1995)

$$R_B \frac{D^2 R_B}{Dt^2} + \frac{3}{2}\left(\frac{DR_B}{Dt}\right)^2 = \left(\frac{P_B - P}{\rho_l}\right) - \frac{4\nu_l}{R_B}\frac{DR_B}{Dt} - \frac{2\sigma}{\rho_l R_B} \tag{4.99}$$

However, during the bubble collapse, the bubble interface reaches very high velocity such that the liquid media needs to be treated as a compressible liquid. Therefore, in our model, we use the Keller-Miksis (K-M) equation for bubble dynamics, which is a derivation of R-P equation, as:

$$\begin{aligned}\left(1 - \frac{1}{C}\frac{DR_B}{Dt}\right)\frac{D^2 R_B}{Dt^2} + \frac{3}{2}\left(1 - \frac{1}{3C}\frac{DR_B}{Dt}\right)\left(\frac{DR_B}{Dt}\right)^2 = \\ \left(1 + \frac{1}{C}\frac{DR_B}{Dt} + \frac{R_B}{C}\frac{D}{Dt}\right)\left(\frac{P_B - P}{\rho_l} - \frac{4\nu_l}{R_B}\frac{DR_B}{Dt} - \frac{2\sigma}{\rho_l R_B}\right)\end{aligned} \tag{4.100}$$

where C is sound speed in liquid phase. K-M and R-P equations are the same during the growth and collapse of the bubble. However, K-M equation deviates from the R-P equation in bubble rebound oscillations after the first collapse.

R-P equation is known as a very stiff ODE due to sharp changes of velocity at very small time scale during the bubble collapse and rebound. As we use 4th order Runge-Kutta method to integrate the second order ODE time steps are crucial to get a converged and accurate solution. If a large time step is used the solution will diverge. A very small time step, in order of few nano-seconds or less, is required to capture the bubble collapse accurately. Using a constant time step of this order will increase the computational time significantly, and the simulation will be not possible even for a single bubble. Therefore, an adaptive time stepping method is required to march with large time steps for most of the bubble life, and use very small time step as required during the bubble extreme conditions at collapse.

In this study, we used a novel time stepping method that changes time step according to the changes of bubble radius. A function of temporal radius change is calculated at the end of each time integration as:

$$e_n = \frac{\left|R^n - R^{n-1}\right|}{\left|R^n\right|} \tag{4.101}$$

where R^n and R^{n+1} are bubble radius at time n and $n+1$. Using the value of this function at time n, $n-1$, and $n-2$, the concept of a Proportional-Integral-Derivative (PID) controller can be used to control the value of this function remain close to a specified tolerance. Therefore, next time step can be predicted as:

$$\Delta t_{n+1} = \left(\frac{e_{n-1}}{e_n}\right)^{K_P} \left(\frac{TOL}{e_n}\right)^{K_I} \left(\frac{e_{n-1}^2}{e_n e_{n-2}}\right)^{K_D} \Delta t_n \tag{4.102}$$

where K_P, K_I, K_D are the PID tuning constants and it was found that at values of 0.075, 0.175, and 0.01, respectively, the fastest solution is achieved. *TOL* is the tolerance and is set to 0.01. Lower tolerance would result on time steps to be smaller, and the computation time would increase significantly with very small variation in solution. More discussion and results for this method is available on next chapter.

4.3.3. Bubble coalescence model

In DBM model, to model bubble coalescence the Kamp model is implemented. In contrary to PBM that we need to estimate the approach velocity of the bubbles, in DBM model, the relative velocity is obtained instantaneously at the moment of collision. The approach velocity of the bubbles is the component of the relative velocity vector in the direction of a line connecting the bubbles to each other. The position vector is calculated by:

$$\vec{r}_{m,n} = \vec{X}_n - \vec{X}_m \tag{4.103}$$

Where $\vec{X}_m$ and $\vec{X}_n$ are position vectors of the two colliding bubbles. Collision occurs when the distance between the bubbles is smaller than the summation of the radius of two bubbles and the approach velocity is positive. The approach velocity is calculated as:

$$V_0 = -\frac{\vec{r}_{m,n} \cdot \left(\vec{v}_n - \vec{v}_m \right)}{\left| \vec{r}_{m,n} \right|} \tag{4.104}$$

The probability of coalescence is therefore calculated by:

$$P_c = \exp\left(-\frac{t_d}{t_i} \right) = \exp\left(-\frac{k_1}{2\pi} \left(\frac{3\rho_L V_0^2 d_{eq}}{C_{vm}\sigma} \right)^{1/2} \right) \tag{4.105}$$

Then, a uniform random number between 0 and 1 is generated. If the value of random number is less than the coalescence probability, the bubbles coalesce. Otherwise, the bubbles bounce and new velocities are calculated according to the model (Mattson and Mahesh, 2012).

In case of coalescence, the position, velocity, and radius of the new bubble resulted from the coalescence can be calculated by:

$$R_{mn} = \left(R_m^3 + R_n^3 \right)^{1/3} \tag{4.106}$$

$$\vec{v}_{mn} = \frac{\vec{v}_m R_m^3 + \vec{v}_n R_n^3}{R_{mn}^3} \tag{4.107}$$

$$\vec{X}_{mn} = \frac{\vec{X}_m R_m^3 + \vec{X}_n R_n^3}{R_{mn}^3} \tag{4.108}$$

If the bubbles collide, but the collision does not result in coalescence of the bubbles, the new velocity of the bubbles can be calculated by:

$$v_{m,N} = v_{m,N} + \frac{N' - M'}{L' - 2M' + N'} V_0 \tag{4.109}$$

$$v_{n,N} = v_{n,N} + \frac{L' - M'}{L' - 2M' + N'} V_0 \tag{4.110}$$

$$\vec{v}_m = \vec{v}_{m,T} + v_{m,N} \hat{n}_{m,n} \tag{4.111}$$

$$\vec{v}_n = \vec{v}_{n,T} + v_{n,N} \hat{n}_{m,n} \tag{4.112}$$

4.3.4. Bubble breakage model

In DBM, Martinez-Bazan et al. (1999-a,b) breakage model was used for the breakage modeling of a bubble in turbulent flow. In this model, the bubble breakage is assumed to be binary, which means only two daughter bubbles are produced as a result of the mother bubble breakage. In their experiments, no breakage other than binary breakage was observed. In this model two forces on the bubble surface are studied i.e. non-inertial forces and surface tension forces are estimated according to the following equations

The breakup occurs when the non-inertial forces dominate the surface forces, thus, the critical minimum diameter required for a bubble to breakup is as follows:

$$D_c = \left(12\sigma / \left(\beta\rho\right)\right)^{3/5} \varepsilon^{-2/5} \tag{4.113}$$

where σ is surface tension, β is a constant, ρ is liquid density, and ε is the dissipation rate.

The breakage frequency is the rate at which a bubble breaks in a certain condition. The breakage frequency is a function of the turbulence and diameter of the bubble in the flow as follows:

$$g\left(\varepsilon, D\right) = K_g \frac{\sqrt{\beta\left(\varepsilon D\right)^{2/3} - 12\sigma / \left(\rho D\right)}}{D} \tag{4.114}$$

where D is mother bubble diameter, K_g is empirical constant.

When a bubble breaks into two smaller bubbles, the minimum size of the bubble that can be produced is found as:

$$D_{\min} = \left(\frac{12\sigma}{\beta\rho D}\right)^{3/2} \varepsilon^{-1} \tag{4.115}$$

Daughter bubble size distribution is found according to the Eq. 4.114 where the maximum possibility of daughter bubble size is $D^*=0.8D_0$.

$$P(D^{*}) = \left(\frac{1}{2}\rho\beta\left(\varepsilon D_0\right)^{2/3}\right)^{2}\left[D^{*2/3} - \Lambda^{5/3}\right]\left[\left(1 - D^{*3}\right)^{2/9} - \Lambda^{5/3}\right] \quad (4.116)$$

where $\Lambda = D_c / D_0$ and $D_C = \left(12\sigma / \left(\beta\rho\right)\right)^{3/5} \varepsilon^{-2/5}$.

4.3.5. Gas diffusion

In liquid with various amounts of NCG dissolved, the gas diffusion through the bubble interface can be important and effective on the cavitation inception and BSD. Therefore, the gas diffusion model was implemented in DBM to study the effect of gas diffusion. Most studies neglect this term due to the high computational effort it requires. As explained for PBM, Higbie penetration model can be used for a bubble flowing in water. The mass transfer coefficient and rate, using this theory, can be estimated as

$$\frac{dm}{dt} = k_l A \Delta C M_W = k_l A \Delta P H M_W \quad (4.117)$$

where k_l is the mass transfer coefficient and can be calculated as

$$k_l = 0.301\mathrm{Sc}^{-1/2}\left(\varepsilon \nu\right)^{1/4} = 0.301\sqrt{C_{diff}}\left(\frac{\varepsilon}{\nu}\right)^{1/4} \quad (4.118)$$

A is the bubble surface area, H is Henry constant, M_W is the gas molecular weight, ΔC is the concentration difference between the bulk liquid and the gas concentration at the bubble surface in the liquid phase, which is related to the pressure inside the bubble and saturation pressure of liquid. Sc is the Schmidt number, ε is the energy dissipation rate, v is kinematic viscosity of the liquid.

In the previous case, the bubble wall is not moving with reference to the bubble. Another factor that can affect the rate of gas diffusion is bubble wall velocity. A stationary bubble that is imposed to an oscillating pressure field starts to oscillate around the initial radius. The variation of bubble size induces a different concentration at the bubble wall, which results in concentration gradient momentarily in the liquid. This phenomenon is known as rectified diffusion. The concentration profile around the bubble can be solved using the transport equation for the gas concentration (C) as:

$$\frac{\partial C}{\partial t} + u.\nabla \mathrm{C} = D\nabla^2 C \tag{4.119}$$

where D_g is gas diffusion coefficient of gas in the liquid. The boundary conditions for this equation are

$$\begin{aligned} &C = C_\infty \text{ for } t = t_0 \\ &C \to \infty \text{ for } r \to \infty \\ &C = C_S \text{ for } r = R \end{aligned} \tag{4.120}$$

where C_S and C_∞ are the gas concentrations in liquid at bubble surface and far from the bubble, respectively. R is the bubble radius, and r is the distance from the bubble center. As the concentration of the gas in the liquid is low, Henry law can be implemented to relate C_S to the gas pressure inside the bubble using

$$C_S = \frac{P_g}{H} \tag{4.121}$$

where H is henry coefficient at bubble temperature.

Solving the transport equation numerically, using finite difference method in one direction (radial), requires a large number of nodes for discretizing the space from R to infinity, as it requires a very fine resolution close to bubble surface. Therefore, it requires non-uniform discretization for optimum mesh structuring. Ilinskii et al. (2008) transformed the Lagrangian spherical form of the transport equation into a new form to avoid the need for discretization to a large r as

$$\xi = \frac{R_0}{r_L} \tag{4.122}$$

where r_L is the distance from the bubble in Lagrangian frame. By substituting ξ into the Lagrangian form of the transport equation

$$\frac{\partial C}{\partial t}=D\frac{\partial}{\partial s}\left[\left(3s+R^3\right)^{4/3}\frac{\partial C}{\partial s}\right] \tag{4.123}$$

where $3s=r^3-R^3=r_L^3-R_0^3$, they obtained the following equation

$$\frac{\partial C}{\partial t}=\frac{D}{R_0^2}\xi^4\frac{\partial}{\partial\xi}\left\{\left[1+\xi^3\left(\frac{R^3}{R_0^3}-1\right)\right]^{4/3}\frac{\partial C}{\partial\xi}\right\} \tag{4.124}$$

The new boundary conditions are

$$\begin{aligned}C&=C_S \text{ for } \xi=1\\ C&=C_\infty \text{ for } \xi=0\end{aligned} \tag{4.125}$$

With the new equation, a uniform discretization of ξ in the interval (0,1) can be implemented for solving the equation. The gas moles that diffuse from the liquid to the bubble or vice versa can be calculated by

$$\frac{dN}{dt}=-\frac{4\pi DR^4}{R_0^3}\frac{\partial C}{\partial\xi} \tag{4.126}$$

In another approach, the approximate solution proposed by Plesset and Zwick (1953) for the heat transfer rate at the bubble wall is converted to the mass transfer based on the similarity analogy. Therefore, the rate of gas transfer at the bubble wall can be calculated by

$$\frac{dN}{dt}=N'(t)=\frac{R^2}{2\sqrt{h}}\left[\frac{C_\infty-\frac{P_g}{H}}{\frac{1}{4\pi\sqrt{\pi D}}}-\int_0^{t-h}\frac{N'(\tau)}{\int_\tau^t R^4(y)\,dy}d\tau\right] \tag{4.127}$$

where *N'*(*t*) and *N'*(*τ*) are the net number of moles crossing the bubble surface at times *t* and *τ*, respectively. *h* is the current time step (time step of RK4 solver at each step).

In order to couple the mass transfer rate into the bubble dynamics equation, the derivative of the gas pressure inside the bubble should be calculated as a function of the rate of changes in moles of the gas in the bubble. This can be achieved by using the energy balance in the bubble with the vapor and NCG as gas component in it (Hsiao and Chahine, 2012).

$$dU = -dW + \sum_{i=v,g} n_i' h_i dt \tag{4.128}$$

where dU is the change in the internal energy

$$dU = \sum_{i=v,g} c_{v,i} d\left(n_i T_i\right) \tag{4.129}$$

dW is the work done by the control volume

$$dW = \left(p_v + p_g\right) dV_b \tag{4.130}$$

and h_i is the specific enthalpy of component i

$$h_i = \sum_{i=v,g} n_i' c_{p,i} T_l \tag{4.131}$$

c_v and c_p are the heat capacity at constant volume and pressure, respectively. by substituting the Daltons law, into energy balance equation it can be found

$$p_g' = \frac{E/p_g - Dp_g - F}{A + B/p_g^2} \tag{4.132}$$

where

$$A = \left(c_{p,g}^{Tb} - R_u\right)\frac{V_b}{R_u} \tag{4.133}$$

$$B = c_{p,v}^{T_l} T_l p_v n_g \tag{4.134}$$

$$D = c_{p,g}^{T_b} \frac{V_b'}{R_u} \tag{4.135}$$

$$E = c_{p,v}^{T_l} T_l p_v n_g' \tag{4.136}$$

$$F = \frac{c_{p,v}^{T_l}}{R_u} p_v V_b' - c_{p,g}^{T_l} T_l n_g' \qquad (4.137)$$

The latter model, does not account the effect of bubble motion in the liquid. For a bubble in cavitation flow, it is needed to account the mass transfer for both wall motion and bubble motion relative to the liquid. More discussions on the validity of the mass transfer model for oscillating bubble and comparison with experimental data are available in next chapter.

4.4. Summary

In this chapter, three CFD models for cavitation were explained in detail. First model is the cavitation model proposed by Singhal et al (2001) as the full cavitation model. This model can be used for predicting the cavitation inception in different geometries. However, it does not provide any information regarding the bubble size distribution. The two later models are, basically, for the purpose of estimating the bubble size distribution. These two models use two different approaches known as Eulerian and Lagrangian approaches. The advantage of Eulerian approach is faster computations, and also intrinsic averaging over time. On the other hand, Lagrangian approach can be more physically representative of the phenomena, as each bubble is tracked in this model, and the physics applied to each bubble depending on the size of the bubble, or other properties can be calculated accurately. Moreover, the surface tension effects are considered in this model. However, it can be computationally expensive, if the bubbles interaction with each other or on the fluid are inserted into the simulation.

Many attempts to overcome these limitations are made with different researchers such as developing different algorithms in searching of neighbor bubbles of a bubble instead of a binary search. In next chapter, some of these challenges are mentioned. The main focus of next chapter is on verification of the correct implementation of models explained in this chapter and validation of some of the models individually and in full package with available experimental data from literature or experimental results from Chapter 3.

Chapter 5

Results and Discussion

In this chapter, the models, explained in Chapter 4, are applied to some case studies to verify the correct implementation and validation of the model, and the results are discussed. The advantages and disadvantages of each model are explained, and it is shown that DBM is a model that can describe most of the physics in the cavitation phenomena. Then, this model is implemented in prediction of the bubble nuclei growth on the particle and interaction with flotation size bubbles in a dual bubble generator.

In this chapter, the first section explains the solver of bubble dynamics model (Rayleigh-Plesset equation), the challenges of solving Rayleigh-Plesset equation (R-P), and the performance of the novel adaptive time stepping method implemented in this study. The accuracy of the solver is compared to the results from literature. Then, the model is applied to some artificial pressure variations, and the results of the model from a travelling bubble in a venturi are demonstrated.

The next section includes some test cases for validation of most of the models implemented in DBM. The purpose of this section is to ensure that the model is working properly and also if there are different models available for a phenomenon, the models are compared to select a suitable model. For example, there are many models suggested in the literature for bubble coalescence such as Prince and Blanch (1990), Luo and Svendsen (1996), and Kamp et al. (2001). To compare the results of the models, an experimental result from literature was selected that only includes the phenomenon of bubble coalescence in a flowing liquid. Another example is the modeling of gas diffusion for a cavitating bubble. There are many models available for gas diffusion to the bubble in a sinusoidal oscillating pressure field a.k.a. rectified diffusion. There are two ways to model the rate of gas diffusion, explained in last chapter. A set of experiments for rectified diffusion in oscillating pressure was selected to verify the results of the models.

After verification of the models individually, the models are investigated for the prediction of the cavitation inception in the venturi from Chapter 3, at different concentration of NCG, and the results are compared. The experimental results are described in Chapter 3 of this thesis. Then, the results of latter two models, Population Balance Model (PBM) and Discrete Bubble Model (DBM), for the bubble size distribution from the cavitation are compared to the experimental results from this study.

In the last section of this chapter, the DBM and PBM are implemented for modeling a case study regarding the optimization of the design of a Dual Bubble Generator (DBG). The purpose of this section is to obtain insight into the DBG using the modeling. Better understating of the dominant physical phenomena in this device can lead to an optimized design for a desired goal.

5.1. Solver for bubble dynamics

For solving the bubble dynamics equation (Eq. 5.1), a 4th order Runge-Kutta (RK4) method is implemented for integration.

$$RR'' + \frac{3}{2}R'^2 = \left(\frac{P_B - P}{\rho_l}\right) - \frac{4\nu_l}{R}R' - \frac{2\sigma}{\rho_l R} \tag{5.1}$$

The bubbles introduced into the domain are initialized with an initial radius (R_0). The bubble is assumed to be in mechanical equilibrium with the liquid. Therefore, initial wall velocity is set to zero. The bubble pressure is the summation of the partial pressure of vapor and Non-Condensable Gases (NCG). Assuming the mechanical equilibrium, the initial gas pressure in the bubble can be calculated as:

$$P_{g0} = P_l + \frac{2\sigma}{R_0} - P_v \tag{5.2}$$

P_l is the liquid pressure at the center of the bubble, P_v is the vapor pressure, and σ is the surface tension for gas/liquid phases. The instantaneous gas pressure, can be calculated as:

$$P_g = P_{g0}\left(\frac{R_0}{R}\right)^{3k} \tag{5.3}$$

where k is 1 for isothermal process, and 1.4 for adiabatic process. During the time that the bubble is in the cavitation region, the time period of changes of the bubble radius is very small such that the process can be assumed to be adiabatic, and the heat transfer between the bubble and surrounding can be neglected. Therefore, the R-P equation can be written as:

$$RR'' + \frac{3}{2}R'^2 = \left(\frac{P_g + P_v - P_l}{\rho_l}\right) - \frac{4\nu_l}{R_B}R' - \frac{2\sigma}{\rho_l R} \tag{5.4}$$

R-P equation is a second order ODE and can be written as a set of first order ODEs and solved using the RK4 method. At each time step, the liquid pressure is calculated from the pressure at the position of the bubble and used as the input to the equation. Initial conditions for the equation are:

$$R = R_0, R' = 0 \quad \text{at}\, t = 0\text{s} \tag{5.5}$$

The R-P equation is a stiff ODE and the solution of the equation can have significant changes in very short period of time, causing the wall have a large velocity such as 100 m/s for a cavitating flow. To have a stable result, the Runge-

Kutta integration method needs very small time steps, of the order of 1e-7 s, for a bubble of 10 μm in a case of no change in pressure and radius. In case of changes in the radius, this time step needs to be smaller, such as 10e-20 s in some cavitating flows. Using a constant time step can result in very large computational time. Therefore, an adaptive time stepping method that can change time step based on the changes of the radius is required.

In the solution of stiff ODEs, the concept of PID controllers can be implemented to control the time step (Hairer and Wanner, 1991). In this approach a function of radius change (e_n) is defined as:

$$e_n = \frac{\left| R^n - R^{n-1} \right|}{R^n} \tag{5.6}$$

where R^n and R^{n-1} are the bubble radius at time steps n and $n-1$. Next time step is calculated in order to control e_n at a set point, defined as TOL using the values of e_n in three previous time steps. The new time step is calculated as

$$\Delta t_{n+1} = C_{dt} \Delta t_n = \left(\frac{e_{n-1}}{e_n} \right)^{K_P} \left(\frac{TOL}{e_n} \right)^{K_I} \left(\frac{e_{n-1}^2}{e_n e_{n-2}} \right)^{K_D} \Delta t_n \tag{5.7}$$

where K_P, K_I, and K_D are the proportional, integral and derivative constants of the controller and are optimized as 0.075, 0.175 and 0.01. A large value of TOL can cause error and divergence in the solution. A small value will increase the accuracy of calculation by using smaller time steps. However, the computational time will increase significantly for a very small change in accuracy. It was found that a value of 1e-2 for TOL can result in accurate converged solution in most cases of our interest. In order to control the time step from getting very small or very large, minimum and maximum values are set for the time step. As mentioned, the value for maximum time step is 1e-7s and minimum time step is set to 1e-25. The minimum time step is required to handle a bubble collapse when there is no rebound (P_{g0}=0).

5.1.1. Numerical verification of the solver

The variable time step was applied to a case that was studied by Alehossein and Qin (2007). They imposed a pressure profile as shown in Figure 5.1 to a bubble with initial radius (R_0) of 10 µm, initial bubble wall velocity ($[dR/dt]_0$) of zero, and initial gas pressure (P_{g0}) of 90 kPa. Fluid properties are those for water (ρ_l=996 kg/m^3, μ_l=0.0008 kg/m.s, γ=0.072 N/m, p_v=4240 pa).

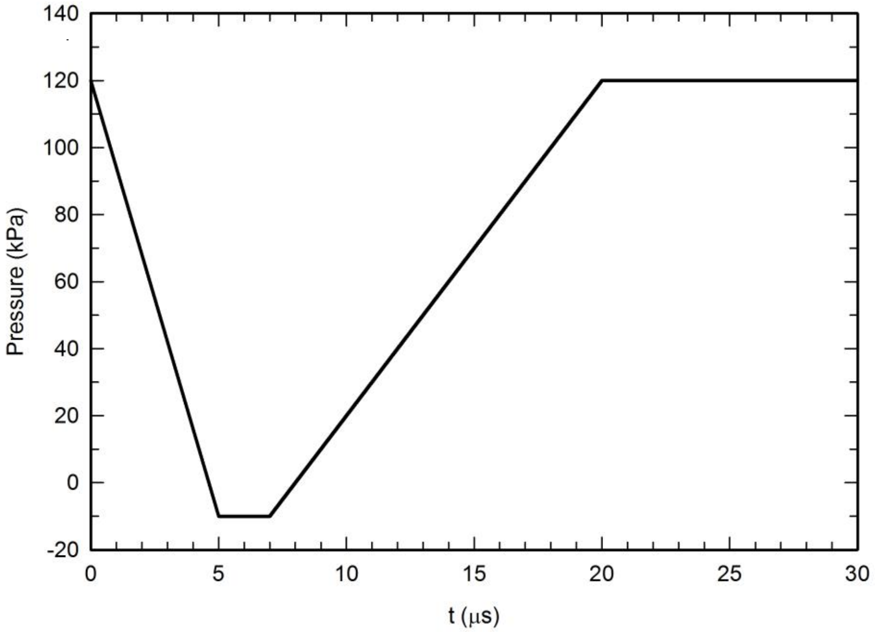

Figure 5.1 Artificial pressure profile used by Alehossein and Qin (2007)

Figure 5.2 shows the solution of RK4 solver with variable time step. The curves include the ratio of radius over initial radius (R/R_0), the ratio of time step over the initial time step, and the ratio of function e_n over *TOL*. It can be seen that at the beginning the time step is constant at maximum time step, same as initial time step, until the e_n is smaller than the tolerance. When it is bigger than the tolerance the new time step is calculated, which is less than the maximum time step. As a result of changes in the time step, the value of e_n is controlled close to the *TOL* value. When e_n becomes less than the *TOL*, the time step is increased up to the maximum value. The rate of changes in e_n and time step during the bubble collapse and rebound are shown in Figure 5.2.

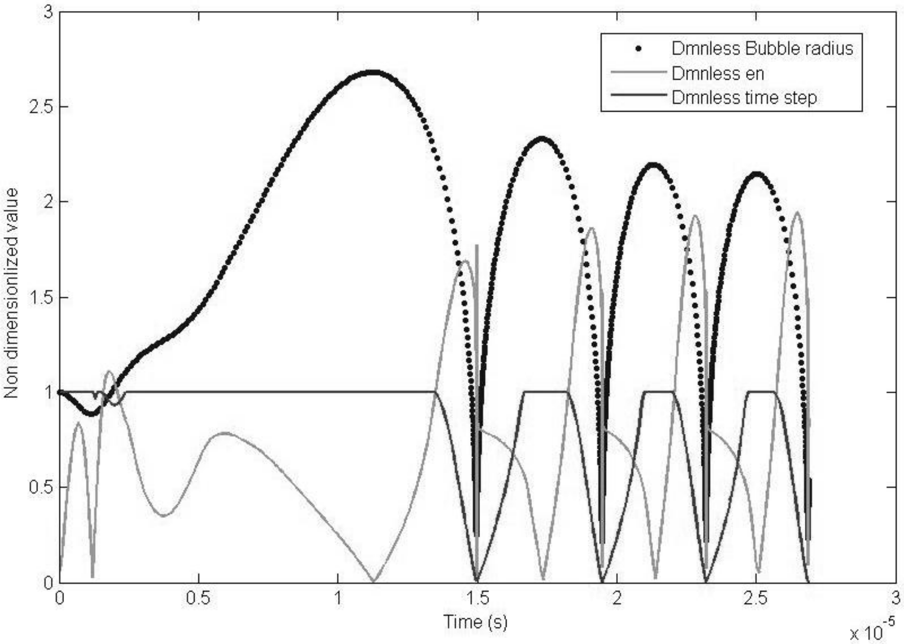

Figure 5.2 Result of RK4 solver for RP equation for Alehossein and Qin (2007) conditions

The advantages of this method, to some of the other methods in literature, are: it is a very fast method due to low number of calculations, it works explicitly and there is no need to redo the calculations in each step, the number of steps is much less compared to a constant time stepping method. Figure 5.3 shows the solution of previous example. Compared to Alehossein and Qin (2007) method, this method is more robust and requires less steps and less calculation time.

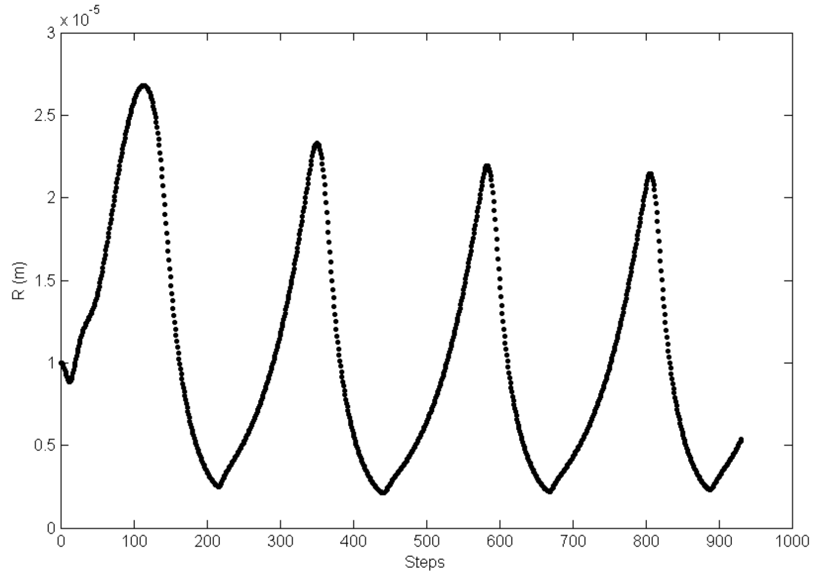

Figure 5.3 Bubble radius versus number of time steps in previous example

5.1.2. Experimental verification of the bubble dynamics

In this section, the numerical solution of Rayleigh-Plesset equation is compared to the experimental data from a bubble behavior in oscillating pressure field (Löfstedt et al., 1993). A bubble with initial radius of 4.5 μm at atmospheric pressure is imposed in an oscillating pressure field of 1.35 atm amplitude, and 26.5 kHz frequency. Liquid properties are ρ=1000 kg/m^3, μ=0.003 kg/m.s, and σ=0.03 N/m. The results of the classic R-P equation indicate that a main physical property is neglected. Therefore, the Keller-Miksis (K-M) (Eq. 5.8) which includes the compressibility of the liquid phase into the R-P equation was examined for this case.

$$\left(1-\frac{1}{C}R'\right)R''+\frac{3}{2}\left(1-\frac{1}{3C}R'\right)R'^2 = \left(1+\frac{1}{C}R'+\frac{R}{C}\frac{D}{Dt}\right)\left(\frac{P_B-P}{\rho_l}-\frac{4\nu_l}{R}R'-\frac{2\sigma}{\rho_l R}\right) \tag{5.8}$$

The results of R-P, K-M equation and experimental data are shown in Figure 5.4. By comparing the results of these two equation and experiments, it is obvious that the compressibility of the liquid is very important in the bubble dynamics.

Therefore, in this study the K-M equation was selected for modeling the bubble dynamics.

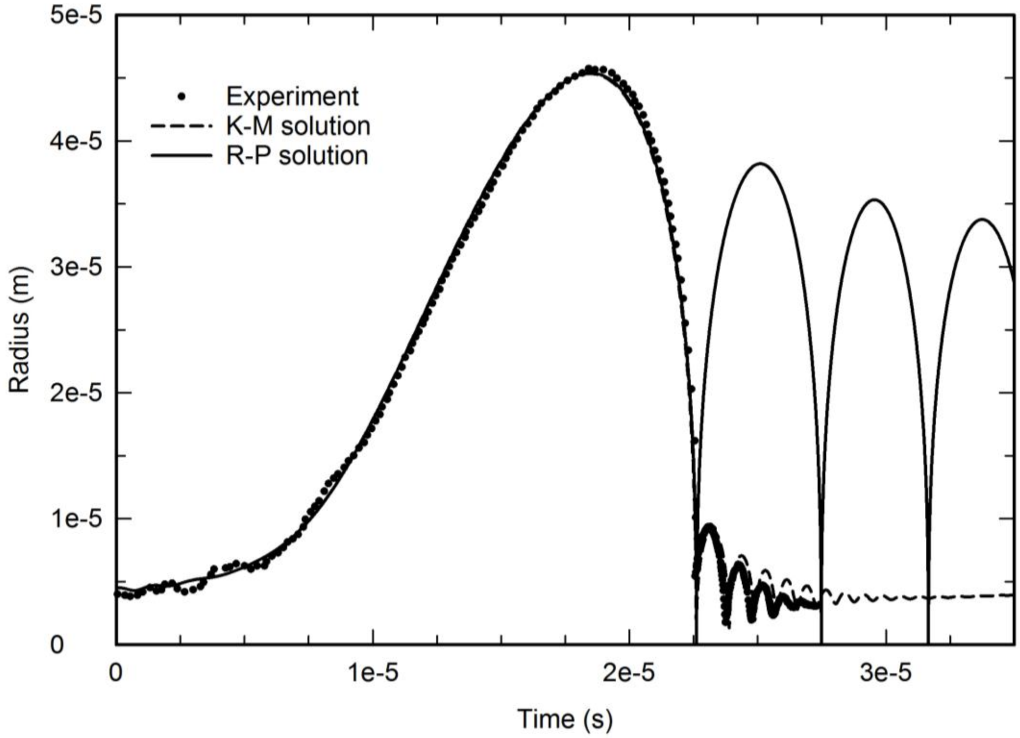

Figure 5.4 Comparison of R-P and K-M equations solution to experimental data (extracted from Figure 1 and 2, Löfstedt et al., 1993)

5.2. Solver for gas diffusion

In this section, we will discuss the solution of the gas diffusion in the liquid around a bubble using two approaches explained in previous chapter, solving the transport equation using finite difference method and solving the Plesset-Zwick equation (P-Z) which is an analytical approximate for the transport equation. The transport equation for the gas concentration (C) is

$$\frac{\partial C}{\partial t}=\frac{D}{R_0^2}\xi^4\frac{\partial}{\partial \xi}\left\{\left[1+\xi^3\left(\frac{R^3}{R_0^3}-1\right)\right]^{4/3}\frac{\partial C}{\partial \xi}\right\} \tag{5.9}$$

The boundary conditions for this equation are

$$\begin{aligned} C &= C_\infty \text{ for } t = t_0 \\ C &= C_S \text{ for } \xi = 1 \\ C &= C_\infty \text{ for } \xi = 0 \end{aligned} \tag{5.10}$$

The gas moles that diffuse from the liquid to the bubble or vice versa can be calculated by

$$\frac{dN}{dt} = -\frac{4\pi DR^4}{R_0^3}\frac{\partial C}{\partial \xi} \tag{5.11}$$

In the other approach, the P-Z equation is used for the calculation of the mass transfer rate at the bubble surface by

$$\frac{dN}{dt} = N'(t) = \frac{R^2}{2\sqrt{h}}\left[\frac{C_\infty - \frac{P_g}{H}}{\frac{1}{4\pi\sqrt{\pi D}}} - \int_0^{t-h}\frac{N'(\tau)}{\int_\tau^t R^4(y)\,dy}d\tau\right] \tag{5.12}$$

For the coupling of mass transfer rate of gas in the bubble dynamics equation, the calculated derivative of gas pressure is used in K-M equation.

Both methods are computationally expensive. First approach requires the solution of the mass transport equation in space every time step. Second approach requires the integration over all previous time steps of bubble history on each time step. Both methods were implemented and tested for the similar case as in Section 5.1.2, with assumed 100% saturation of water with air at the initial pressure ($C_i = H_{(Tamb)}P_0$).

5.2.1. Numerical verification of diffusion model

For the solution of transport equation, different number of nodes were tested, and 20 nodes was concluded as the minimum number for grid resolution. For this case, comparing the computational time for the two methods, it was found that solving the transport equation is faster than P-Z solution (almost 25 times faster). Therefore, the first approach was selected for implementation in the CFD model.

Figure 5.5 shows the comparison of the two mentioned methods for calculation of gas diffusion of an air bubble in water cavitating under the same conditions of the experimental conditions in previous section. The water is assumed at 100% saturation of air at atmospheric pressure. The physical properties and operating conditions are similar to the experiments in Section 5.1.2.

As can be observed, the bubble obtains some extra mass during the expansion. The two methods explained here have close results compared to non-diffusion case. Although the bubble diameters are not much different during the growth and collapse, the final diameter, immediately after the rebounds and oscillation, is significantly different. This difference disappears in a longer time scale due to the diffusion of the gas inside the bubble back to the liquid. The time required for the bubble to return to initial diameter is few orders of magnitudes larger than the time in this calculation. It was concluded that the gas diffusion becomes important in the cavitating bubbles.

This difference is much more for a CO_2 saturated water. Figure 5.6 shows the results of modeling for only bubble dynamics and bubble dynamics with diffusion for cases of 100% saturation of water with air and CO_2. The gas diffusion for CSW results in bubble twice the initial radius after the rebounds. The numerical method with 20 nodes is the method for gas diffusion calculations for the rest of this study.

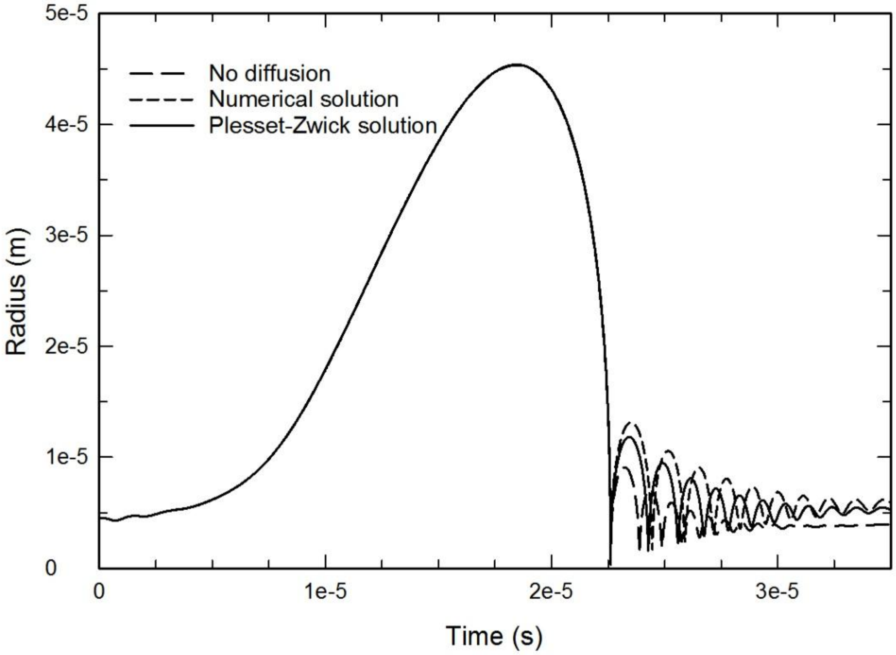

Figure 5.5 Comparison of bubble radius for M-K equation without and with considering gas diffusion for 100% saturation of air

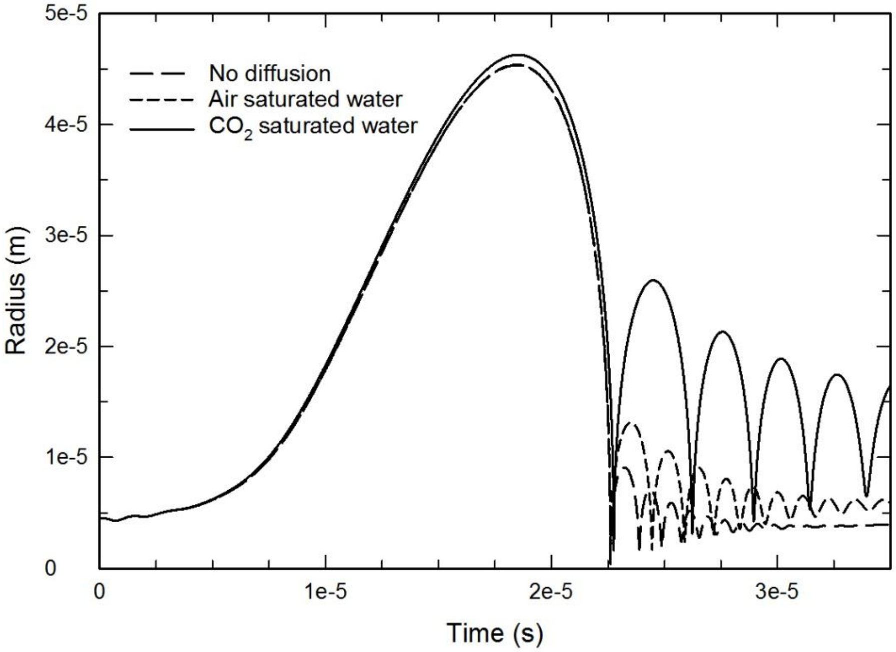

Figure 5.6 Comparison of bubble radius for M-K equation without and with considering gas diffusion for 100% saturation of air and CO_2

5.2.2. Experimental verification of diffusion model

In this section, a set of experiments from the work done by Crum (1980) is compared to the modeling results. He studied the gas diffusion rate in oscillating air bubbles in water (rectified diffusion) for different bubble sizes. He reported the growth rate of air bubble in water by rectified diffusion at 22.1 kHz at different acoustic pressure amplitudes. Depending on the operating conditions, bubbles oscillating in an imposed pressure field with a certain amplitude and frequency can expand or shrink due to rectified diffusion. The threshold acoustic pressure amplitude required to cause the bubbles grow are obtained for various initial bubble diameters at atmospheric pressure and room temperature for air-water system.

To verify our model with the experiments from Crum (1980), the same conditions used in the experiments are applied in the model. Bubbles of radius 20, 35, 50 and 65 μm are imposed to the acoustic pressure field at 22.1 kHz of frequency. The water is assumed air saturated at atmospheric pressure and room temperature. Other constant values include as: density is 1000 kg/m^3, viscosity is 0.001 Pa.s, surface tension is 0.072 N/m, diffusion coefficient is 2.4×10^{-9} m^2/s. For each bubble radius, the acoustic pressure amplitude is varied and the growth of the bubble after 0.1 seconds with respect to initial size is indicated as a measure whether the bubble would expand or shrink. Due to the difficulty of finding the exact value of the threshold acoustic pressure, the threshold is reported as an interval. It was estimated that the threshold relies between the maximum and minimum values shown in Figure 5.7. The results of the modeling are in good agreement with experimental data extracted from the Crum (1980) article.

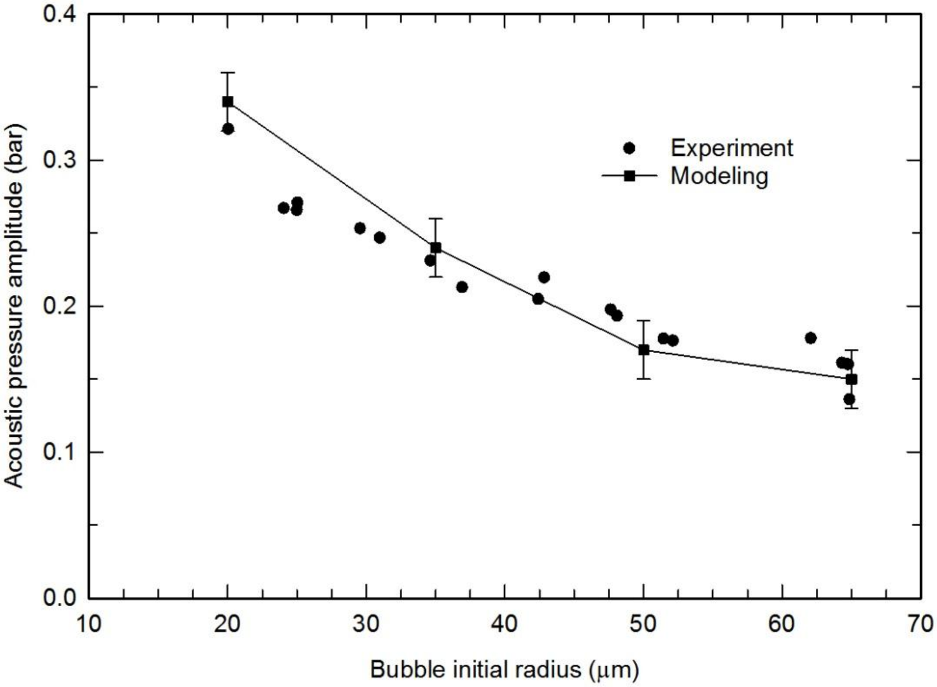

Figure 5.7 Comparison of bubble radius for M-K equation without and with considering gas diffusion for 100% saturation of air and CO_2

5.3. Coalescence modeling

Many researchers have studied the modeling of bubble coalescence in swarm of bubbles in bubble columns, mixers, etc. (Prince and Blanch, 1990; Luo and Svendsen, 1996). These models are applicable to Eulerian approaches in the modeling of the bubbly flows. Moreover, Kamp et al. (2001) model is applicable to both Lagrangian and Eulerian approaches. In this section, these models are explained briefly, and they are implemented in a case study of bubble coalescence in a circular pipe flow in microgravity. The results are compared with experimental data from Colin et al. (1991).

Colin et al. (1991) conducted a set of experiments to study the bubble coalescence in a pipe flow in microgravity, i.e. the gravity is close to zero. The experimental setup is demonstrated in Figure 5.8. Water was pumped through a straight circular pipe section. Air was injected through a nozzle to the middle of the flow. Bubble size distribution (BSD) was measured at two locations which were two meters away in the pipe section. These measurements demonstrate the changes of BSD by the bubble coalescence in the pipe due to the turbulence. One of this measurements has been used as a case study in this study. The BSDs at two locations of inlet and outlet are shown in Table 5.1.

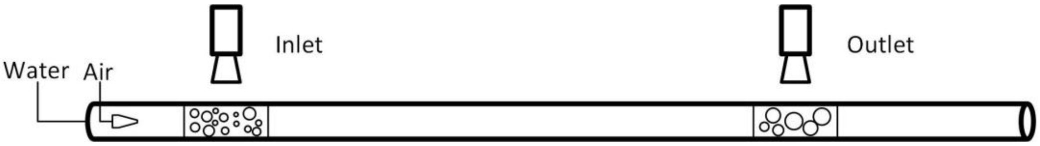

Figure 5.8 Schematic of the experimental setup used by Colin et al (1991)

Table 5.1 BSD at the inlet and outlet

Bubble diameter (mm)	Number % at the inlet	Number % at the outlet
1	2	0
2	28	14
3	42	12
4	28	13
5	0	12
6	0	8
7	0	10
8	0	8
9	0	8
10	0	4
11	0	4
12	0	4
13	0	3
14	0	0

5.3.1. Population balance modeling

To model the bubbly flow in the pipe using PBM, explained in Chapter 4, a rectangular domain was selected with axial symmetry at the center of the pipe. The pipe radius and length were 0.02 m and 2.5 m, respectively. The velocity of the gas and liquid phases were 1 and 0.9 m/s respectively, which were extracted from the article. The BSD at inlet (Table 5.1) was imposed as boundary condition for the PBM equations. Realizable k-ε turbulence model with enhanced wall treatment was used to model the turbulence. For the coalescence model, Prince, Luo, Lehr and Kamp models were implemented. Drag, lift, virtual mass, wall lubrication, and turbulent dispersion forces as explained in Chapter 4 were implemented. Breakage model and growth models are inactive in this set of modeling. The outlet BSD, to be compared to experiment, was the average of the BSD at two locations which were 2 and 2.45 m from the inlet. This method was considered because, in the experiments, the BSD is measured in a 45 cm long window in the pipe. Figure 5.9 shows the BSD at the outlet for each coalescence model compared with the experimental result. The comparison shows that the Kamp et al. coalescence model compared to other coalescence models is in best agreement with experiments.

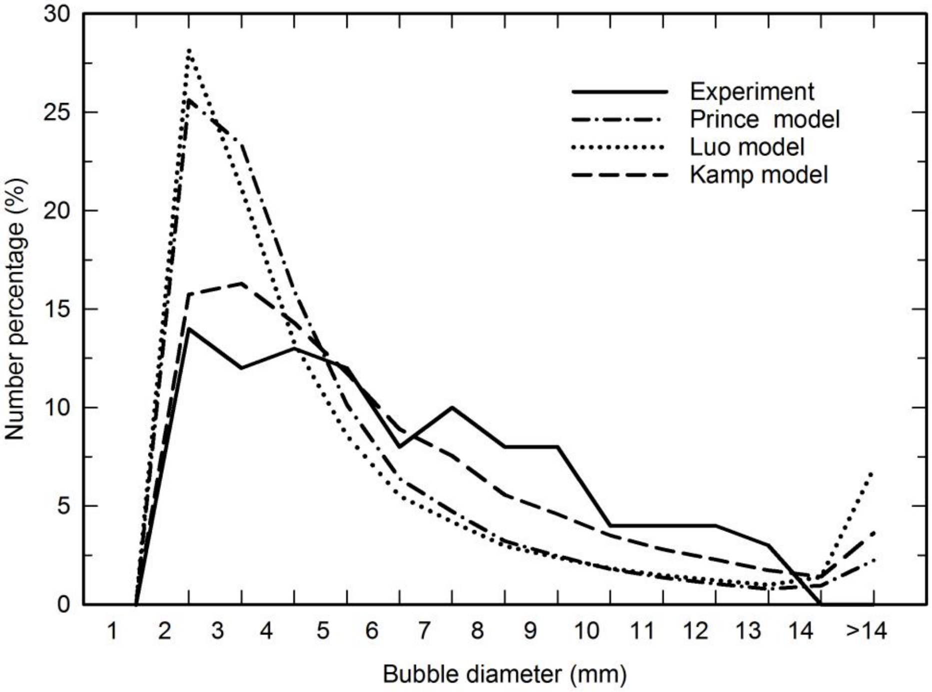

Figure 5.9 BSD at the outlet for different coalescence models and the experiments

5.3.2. Discrete bubble modeling

As shown in the last section, Kamp model for coalescence is capable of predicting the BSD better in comparison with other models. To study the behavior of Kamp model in DBM, the coalescence probability from the model is calculated for each pair of bubble that are close to each other (defined by a threshold distance). Using the coalescence probability, the result of collision, whether coalescence or no coalescence, is determined. In case of coalescence, the position, velocity, diameter, and other properties of the new bubble are appointed to the bubble based on the values of two initial bubbles. If no coalescence occurs, the bubbles collided would get new velocity based on the conservation of momentum. The equations to calculate these properties are discussed in Chapter 4.

For initial attempt, k-ε turbulence model was implemented for the flow calculations. The liquid flow would affect the motion of bubbles. Because *k-ε* model gives the average of the flow velocity during the time, the bubbles motions are not stochastic, and basically, it follows the streamlines. However, the bubbles motion, in turbulent flow, involves fluctuation in the motions of the bubbles, which are important in this case, to capture the correct interactions between the bubbles. Two methods can be implemented to capture the bubble motions. First, mentioned in the last chapter, uses an estimation for the u', fluctuation velocity of the bubble, can be generated randomly at each moment, and it can be added to the average liquid velocity. The new velocity is the velocity that is used for the bubble motion calculation. The model accounts for the duration that the velocity fluctuation can be effective for each bubble temporally. However, these fluctuations are independent spatially from each other. To have a more accurate calculation of the velocity fluctuations, second approach can be used, which includes the use of Large Eddy Simulation (LES) turbulence model. Following, a brief explanation of the mentioned approaches is presented.

Turbulent dispersion modeling

As mentioned above, in *k-ε* model, to predict the dispersion of particle due to turbulence an estimation of the instantaneous velocity and velocity fluctuations is required to be calculated from the values of *k* (turbulent kinetic energy):

$$v = \bar{v} + v' \tag{5.13}$$

$$v' = r\sqrt{2k/3} \tag{5.14}$$

r is a Gaussian distributed random number. An integral time scale to describe the time which a particle spends in turbulent motion along the particle path is calculated as:

$$T = \int_0^\infty \frac{v'_p(t)\, v'_p(t+s)}{\overline{v'^2_p}} d\tau \tag{5.15}$$

For small particles this integral time is the Lagrangian integral time and can be approximated as:

$$T_L \approx 0.15 \frac{k}{\varepsilon} \tag{5.16}$$

The eddy life-time is defined as:

$$\tau_e = -T_L \log r' \tag{5.17}$$

r' is a uniform random number between 0 and 1. Time taken by a particle to cross an eddy is defined as:

$$t_{cross} = -\tau \ln \left[1 - \left(\frac{L_e}{\tau \left| v_l - v_p \right|} \right) \right] \tag{5.18}$$

where L_e is the eddy length scale, and $|v_l - v_p|$ is the magnitude of the relative velocity. The particle is assumed to interact with the fluid phase eddy over the smaller of the eddy lifetime and the eddy crossing time. When this time is reached, a new value of the instantaneous velocity is obtained by applying a new value of *r* in Eq. 5.12.

Large Eddy Simulation (LES)

LES model implements a filtering function to solve the governing equations. The velocity components in LES are decomposed. The small scale variables are universal in nature so they can easily be modeled with a small error. Whereas the large scale variables is more geometry and flow dependent so they should directly be resolved to minimize the solution error as it is done in LES model. A flow variable φ can be defined as sum of filtered (large scale or resolved) and sub-grid (modeled) part, as shown by equation below:

$$\varphi=\overline{\varphi}+\varphi' \tag{5.19}$$

The large scale part is obtained by the volume averaging procedure:

$$\overline{\varphi}\left(x,t\right)=\int_{Vol}G\left(x-r,t-\tau\right)\varphi\left(r,\tau\right)d\tau dr \tag{5.20}$$

where *G* is the filter function. In the filtered Navier-Stoke's equation:

$$\frac{\partial}{\partial t}\left(\rho\overline{v_i}\right)+\frac{\partial}{\partial x_i}\left(\rho\overline{v_iv_j}\right)=-\frac{\partial\overline{p}}{\partial x_i}+2\mu\frac{\partial}{\partial x_i}S_{ij} \tag{5.21}$$

the non-linear advection term, $\overline{v_iv_j}$, is made of filtered velocities, which means that it cannot be computed directly from the filtered variables, and requires to be modeled. The non-linear term can be expanded in the filtered navier-Stoke's equation:

$$\frac{\partial}{\partial t}\left(\rho\overline{v_i}\right)+\frac{\partial}{\partial x_i}\left(\rho\overline{v}_i\overline{v}_j\right)=-\frac{\partial\overline{p}}{\partial x_i}+2\mu\frac{\partial}{\partial x_i}S_{ij}-\frac{\partial\tau_{ij}}{\partial x_j} \tag{5.22}$$

where τ_{ij} is the residual stress tensor and divided into

$$\tau_{ij}=L_{ij}+C_{ij}+R_{ij} \tag{5.23}$$

L_{ij}, C_{ij}, R_{ij}, are the Leonard tensor, Clark tensor, and Reynolds sub-grid tensor, respectively. These terms represents interaction among the large scales, the large and small scales, and the sub-grid scales, respectively. The sub-grid scale stresses can be modeled with the help of a mixing-length based eddy-viscosity approach:

$$\tau_{ij} - \frac{1}{3}\tau_{kk} = -\frac{2\mu_t \overline{S_{ij}}}{\rho} \tag{5.24}$$

where μ_t is the sub-grid scale turbulent viscosity. It can be modeled using various sub-grid scale models *i.e.* Smagorinsky model, WALE, and WMLES.

In this study both these approaches were examined for the Colin et al. (1991) experiments. A circular 3D pipe with diameter of 0.04 m and 2.5 m long was selected as domain. For *k-ε* model, with enhanced wall treatment, the domain is discretized with a total of 400000 cells with wall y^+ of 30-40. Therefore, wall function is used as the near-wall treatment model. For LES, a very finer mesh is required to capture the turbulent eddies. The mesh generated had a total of 3 million nodes with wall $y^+ \approx 1$, $x^* \approx 30$, $r^* \approx 5$, $\theta^* \approx 10$. An O-grid type of mesh was used to eliminate the singularity at the center. The cross-section of the pipe and cells distribution are shown in Figure 5.10. The convergence criterion is set to 1e-5. After the initial converged solution is achieved at steady state, solver is switched to transient. After 1 second, the bubble injections are initiated at the inlet with three sizes of 2, 3, and 4 mm diameter according to the size distribution provided in the paper. After 5th second the sampling of bubbles at the outlet is initiated for the next 3 seconds every 0.5 s. In Figure 5.11, the axial velocity profile from LES is compared to experimental results for similar Reynolds number (Re=41000) in pipe flow from Laufer (1954).

The Bubble Size Distributions (BSD) at the outlet for the two approaches and the LES model are shown in Figure 5.12. The comparison of the results demonstrates the importance of the turbulent dispersion in the coalescence phenomena in bubbly flows. The reason that the results for *k-ε* model are different from experiments significantly is that the turbulent dispersion model implemented in *k-ε* model uses a random fluctuation velocity for each location in domain. However, the liquid velocity fluctuations are not independent spatially. Therefore, in LES model that calculates the velocity fluctuations correctly has a better prediction of the BSD. In *k-ε* model, a proper model for prediction of the dispersion due to turbulence for large bubbles is also required as the bubbles will have a different fluctuation velocity than liquid. The results from the LES model are very close to the experiments showing that the coalescence model implemented is a proper model for our purposes in this study. Therefore, LES model is suggested to be implemented to capture the correct path of the bubbles. However, using LES turbulence model in cavitation model with single processor increases computational time significantly. For example, the calculation time for the modeling of the bubbles coalescence using LES model took about 6 month. This is due to the fact that using the neighbor bubble search method implemented in this study is based on the searching for bubbles in neighbor cells with a distance less than a certain value (1.5 times of the biggest bubble size possible in the domain). Therefore, the neighbor bubble search is grid size dependents which results in increasing the computational time to inapplicable range. Therefore, in this study, *k-ε* with the mentioned turbulent dispersion model is implemented.

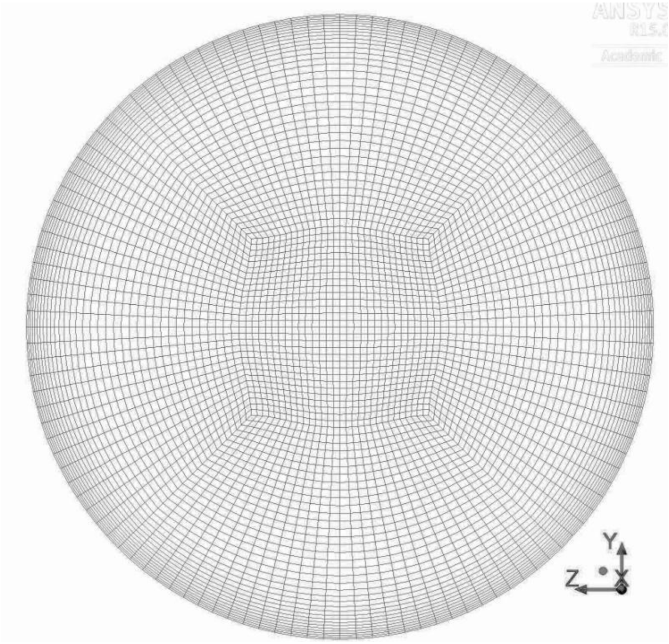

Figure 5.10 Cross-section of the pipe mesh

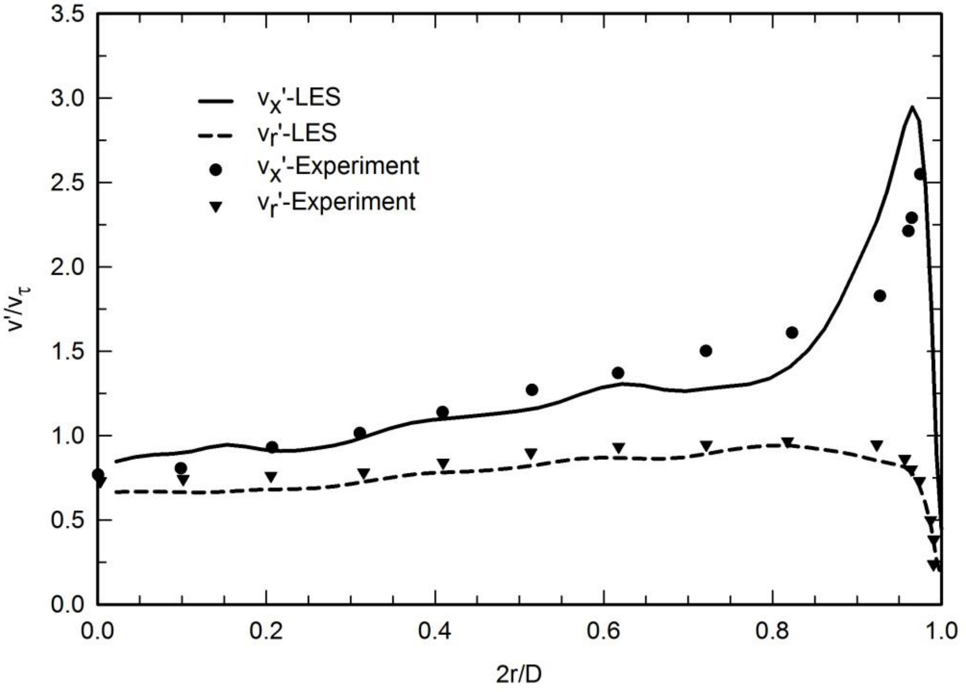

Figure 5.11 RMS values of axial and radial velocity (U_x, U_r) over shear velocity versus the distance from center of the pipe (r) for LES model compared to experiments

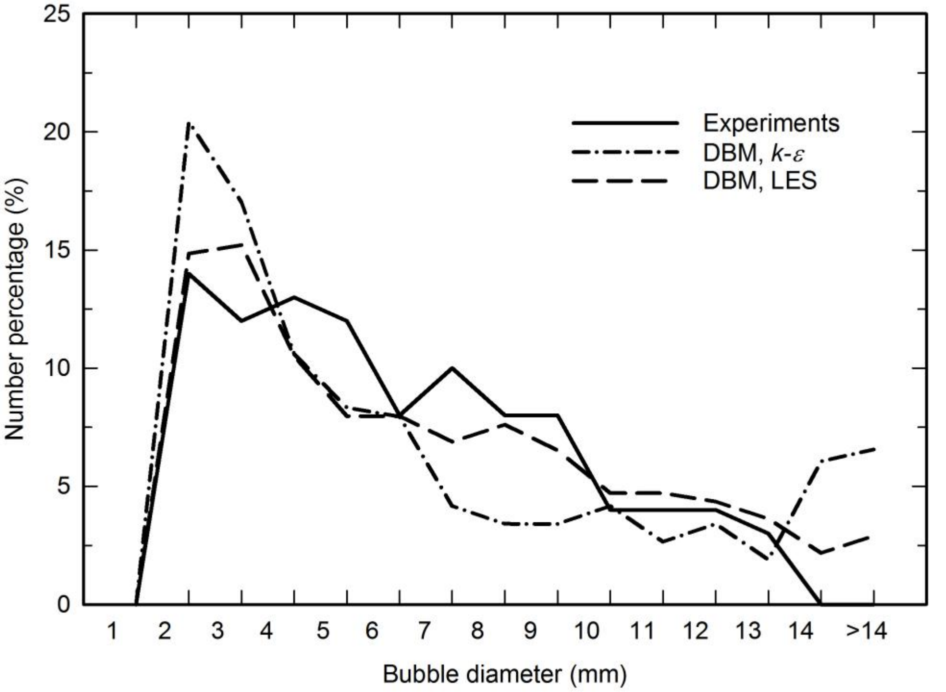

Figure 5.12 Comparison of the BSD at the outlet for DBM and PBM models with the experiments

5.4. Cavitation modeling

In this section, the cavitation inception for different amounts of non-condensable gases dissolved in water is investigated in glass venturi and long orifice used in the experiments from Chapter 2. Gravity was neglected in this section as the Froude number, the ratio of the flow inertia to the external forces (gravity), for the bubbles were always larger than 100 in the experiments. The geometry of the glass venturi and long orifice is reconstructed in Ansys-ICEM. Due to circular shape and symmetry of the venturi a 2-D axisymmetry geometry is used for this study. The meshing of the geometries is done using structured (blocking) mesh, with refinements at the throat and after the throat, where the cavity grows and collapses. The y^+ for first mesh layer is kept less than one for all the runs, and 10-15 layers of mesh exist in the boundary layer for solving the laminar profile in this region. The mesh is denser near the area where cavitation is occurring. Figure 5.13 shows the mesh used in this study for the two geometries. The inlet (left-blue) and outlet (right-red) are 50 mm (12D) away from the throat area. Constant velocity is used for inlet, and the distance from the throat allows the flow to become fully developed before the throat. Constant pressure with zero gradients is used for the outlet. The distance from the throat is required due to the recirculation flow in the expansion area.

Figure 5.13 The mesh used for 2D geometry

To study the grid independence, initially a coarse grid size was produced with specifying low number of divisions per line (such as 6 radial divisions). The y^+ was kept lower than 5 for a valid measurement of near-wall treatment model. For the coarse mesh, total number of 5000 mesh elements was created. Further grid refinement was applied to find the optimum grid size, at a point that the difference between the results of different mesh sizes are small enough. For larger number of the grids, the results converge to a point, and further refinement has negligible effect on the accuracy. Further increase in mesh size would increase the computational requirements. The variable studied was the minimum pressure in the domain because it has the most effect on the results. Figure 5.14 shows the changes of the solution versus grid size for single phase flow at Re=3600. As shown with a mesh of ~11k element the variable studied does not change much by increasing the grid refinement further.

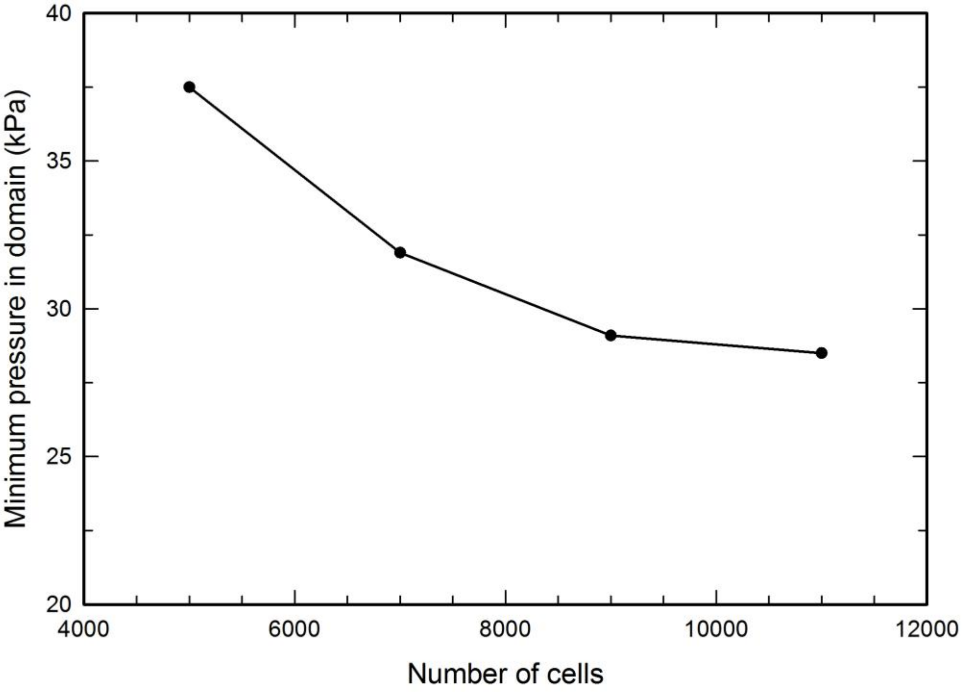

Figure 5.14 Minimum pressure profile in domain at different number of grid cells

5.4.1. Singhal cavitation model

In the first cavitation model, Singhal cavitation model, uniform velocity boundary condition is used for the inlet, and pressure boundary condition is used for the outlet, set at 100 kPa absolute. This pressure can be important as it does affect the cavitation inception i.e. when the minimum pressure in the domain reaches the vapor pressure. Outlet pressure is set to atmospheric pressure (100 kPa ambient pressure) and the pressure drop after the venturi in the pipe before being exposed to atmospheric pressure is negligible. The velocity is calculated from the flowrate of water in each experiment for the 4 mm ID pipe. The mass fraction of NCG for each experiment is calculated based on the solubility of the gas in water at the equilibrium pressure of gas and water before the experiments, i.e. DGW, ASW, and CSW the mass fractions of NCG are 5, 21, 1500 ppm respectively. No slip boundary condition is used for the wall.

Coupled solver with upwind second order discretization is implemented for solving the problem. A pseudo time step of 1e-5 s is implemented for non-cavitating region. In the cavitating region, the problem is set to transient with a time step of 1e-5 and maximum of 30 iterations per time step. Transient solution method is required due the nature of the cavitation model. The pressure at the inlet is tracked as the convergence criteria. The value of pressure oscillates during the time and the amplitude of oscillation is dampened to a final solution and the residuals drop below 1e-5, which is set as convergence criteria. As an example result, Figure 5.15 shows the contours of vapor volume fraction for ASW at inlet Reynolds number of 6000 compared to the experimental result at the same conditions.

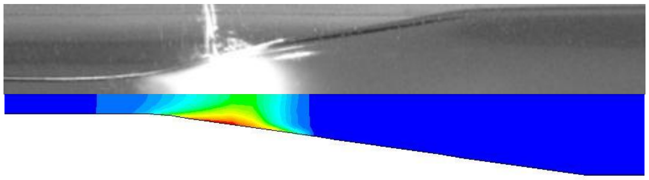

Figure 5.15 Singhal cavitation model results for ASW, vapor volume fraction at Re=6000 (bottom) compared to experiments (top)

To study the ability of the cavitation model to predict the cavitation inception, the results are compared to the experiments for different gas contents. To determine the cavitation inception point in the modeling, the value of the void fraction at the same location as the experiments measurements is recorded (2 mm after the throat). In the Singhal cavitation model the mass fraction of the NCG is converted to the volume fraction and is assumed constant. Therefore, the value of the vapor void fraction is non-zero even in non-cavitating region. Therefore, the void fraction at the inlet is subtracted from the recorded value to get the correct increase of volume fraction due to the pressure decrease in the throat. After investigating the absolute pressure profile, it was found that for the DGW and ASW condition the absolute pressure reaches the vapor pressure. Therefore, the term cavitation inception is correct to be used in this case. However, for the CSW, the minimum absolute pressure does not drop lower than ~20 kPa, which shows that no cavitation occurs in the flow, and the bubbles are only produced due to the expansion of the upstream bubbles. Therefore, cavitation inception in this study represents the production of a measurable amount of gas bubbles in the flow after passing through a low pressure region.

Considering the previous note, the value of the void fraction difference, between the sampling location and the inlet, has a sudden increase at a certain Re number. For DGW and ASW, the reason is that the pressure drops below the vapor pressure and a mass source is inserted into the transport equation for volume fraction (α). For CSW, the gas expands due to the low pressure, and the flow becomes choked flow, the pressure decreases even after the throat, and the vapor volume fraction expands outside the throat. Table 5.2 shows the comparison of the inlet Re numbers at which the cavitation inception occurs for different gas contents in modeling and experiments. This table shows the ability of the cavitation models in predicting the cavitation inception in different water qualities (gas content).

Table 5.2 Comparison of the inlet Re numbers at cavitation inception for different values of gas contents

Estimated gas content (ppm)	Cavitation inception inlet Re number	
	Experiment	Singhal model
5	5200	5000
21	4000	4200
1500	2300	1800

However, the Singhal model contains a major drawback, as it implements the NCG mass fraction in the form of a compressible fluid like gases. In reality, the

NCG is dissolved in the water and the process of the transfer of the NCG dissolved in the liquid to the vapor phase occurs through the nucleation or gas diffusion processes. Therefore, it is recommended to define a model that can represent the physical phenomena happening in a better way. To investigate the shortage of this model the pressure drop caused by the ASW flow passing through the venturi is calculated for different flowrate with single phase and Singhal models and are compared to the experiments. The results are shown in Figure 5.16. The single phase model results are in good accordance to the experimental data in the non-cavitating region (single phase). However, the pressure drop in the cavitating region deviates from the single phase model results. The Singhal cavitation model, can predict the cavitation inception point correctly with a sharp change in the slope. However, the pressure drops predicted are different from the experimental results significantly.

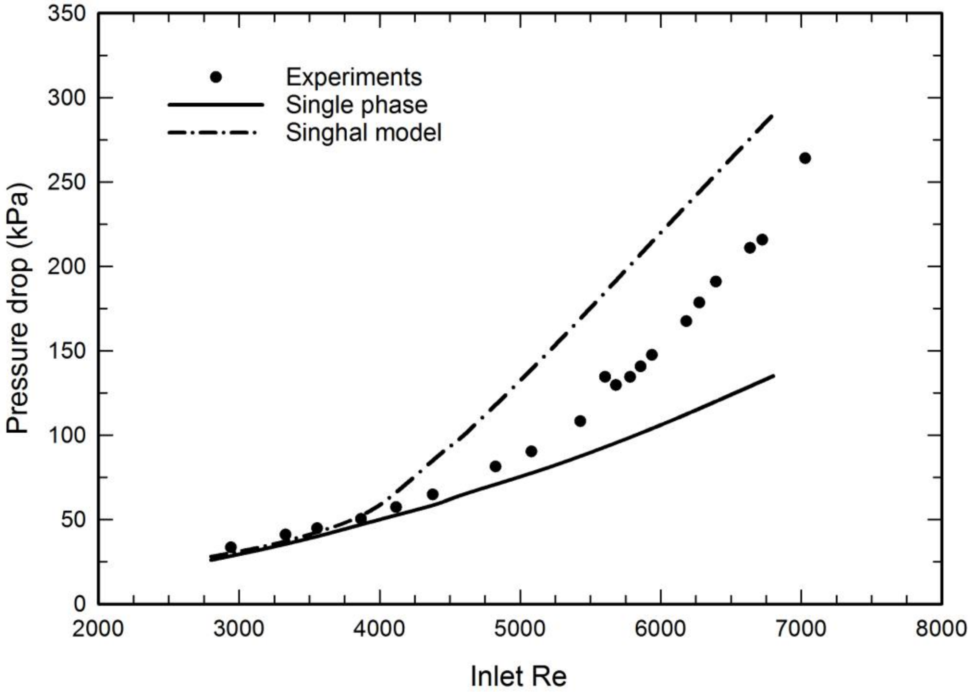

Figure 5.16 Comparison of pressure drop in the venturi for ASW predicted by Singhal mode and single phase model with the experimental results

5.4.2. Population balance model

As shown in Section 5.4.1, the Singhal cavitation model can capture the cavitation inception. Besides the previous mentioned drawbacks for the Singhal cavitation model, another drawback is that it is based on the assumption of constant number density per volume for bubbles. This assumption neglects the gas diffusion, bubbles interactions such as coalescence, and breakage. In this section, to improve the BSD prediction, we propose using the PB model in the compressible form to account for the bubble growth. Moreover, PBM is studied for the cavitation inception and pressure drop prediction in the same geometry as last section besides the comparison of the BSD to the experiments.

For bubble coalescence model, Kamp model, is selected as it was tested before. Due to the fact that there is very small possibility of heterogeneous nucleation on the surface of the glass (because of small contact angle; Li, 2014), no nucleation model was implemented in this study. However, the nucleation can be added to the model as explained in Chapter 4. The bubble is assumed in physical equilibrium and the mass transfer into and from the bubble is calculated using the Higbie penetration model and Blander and Katz (1975). For the solution of the PBM, discrete method is used with 11 bins to cover the bubble size range of 2 μm to 2 mm. For the inlet boundary condition for PB equation, the bin fraction (α_i) for the bin corresponding to bubble diameter of 8e-6 m is set to one. In summary, the inlet flow is mixture of liquid and gas, with total volume fraction of 3e-5 for gas in the form of bubbles with 8 μm diameter. These values are inputs to the model, and are selected from other literatures (Yuan and Schnerr, 2001).

A coupled solver is used for pressure and velocity, and second order upwind is implemented for spatial discretization. Pseudo transient steady state was used with variable time step at various stages of the solution based on the convergence trend. Due to the instability of using Eulerian multiphase model and various forces, mixture models with only drag force applied to the disperse phase is implemented. For convergence criteria, the pressure at inlet and SMD at the outlet are tracked during the iterations. The following procedure is used as solution steps:

1. Domain is initialized with the values from the inlet, except for the volume fraction which is set to zero.
2. Calculation is initializes with time step 1e-3. As the pseudo time step method is implemented, the volume fraction from the inlet marches into the domain. Therefore, an initial single phase profile for pressure and velocity is obtained.
3. After the volume fraction reaches the throat, the time step is decreased to 1e-4 s, and vaporization under-relaxation factor is decreased to 0.01 for the rest of the solution.
4. If required, the solver is set to transient and the flow is averaged over time.

Figure 5.17 shows the contours of SMD and gas volume fraction in and after the throat for Reynolds number of 5200 for ASW flowing through the venturi. From the profiles of SMD and vapor volume fraction, it can be understood that the BSD is significantly dependent on the coalescence. This is because near the wall the SMD of bubbles is much larger than the flow in the center. Therefore, either the gas diffusion or the bubble coalescence are the source of increase in the SMD because the turbulent dissipation rate is at maximum near the wall and is the effective variable in both gas diffusion and collision frequency. As the volume fraction near the wall and center of the flow have similar values, it can be concluded that the coalescence is the source of bigger bubbles formation as coalescence do not affect the vapor volume fraction.

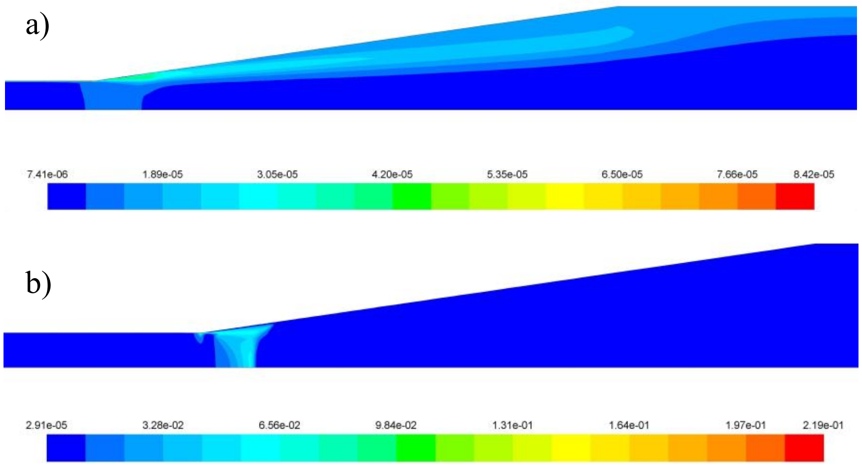

Figure 5.17 a) SMD and b) vapor volume fraction profiles for ASW flow at Re=5200

To compare the pressure drop and BSD to the experimental results, from the solution of the modeling, three values are collected. First, the pressure before and after the throat to calculate the pressure drop; second, the volume fraction and bubble SMD at 10 mm after the throat exit; last, the volume fraction and bubble SMD at a distance of 50 mm from the throat. The pressure drops calculated are compared to the experimental results and the results from Singhal cavitation model are shown in Figure 5.18. It shows a better agreement with the experimental results compared to the Singhal cavitation model. It can be concluded that the volume fraction prediction by the model is over predicted by the Singhal model with the assumption that all the NCG are in the form of gas phase.

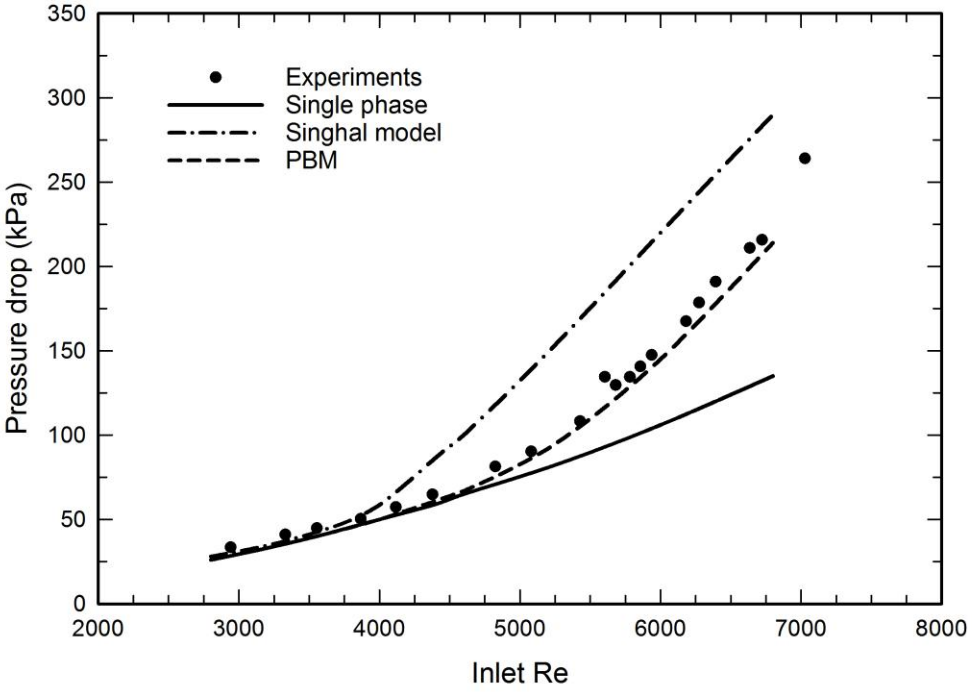

Figure 5.18 Pressure drop calculation from Single phase, Singhal model and PBM compared to the experimental results

Furthermore, the values of IAC for different Reynolds numbers are compared to the results of light transmission method in Chapter 3 (Figure 5.19). The results show that although the values of the modeling and experiment are not exactly matching, but the trends of the changes are predicted well, which represent the coalescence rate between the bubbles increase by the Re number.

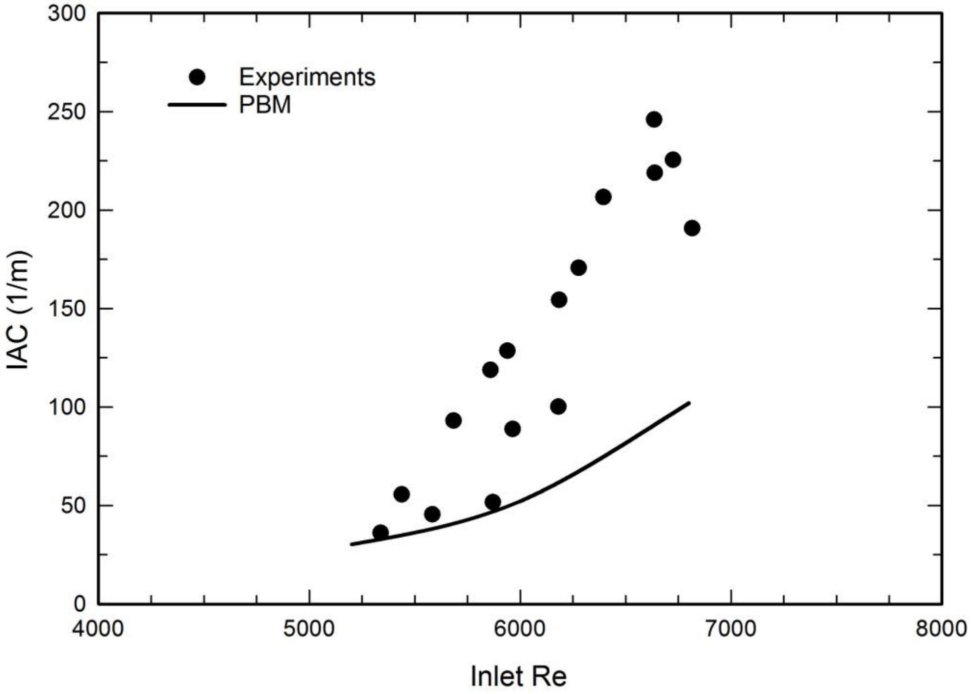

Figure 5.19 Comparison of IAC at 10 mm away from the throat calculated by PBM with the experimental results

Figure 5.20 shows the comparison of the bubble diameter at 50 mm away from the throat for both simulation and experimental results. The comparison again shows a small difference in the bubble diameters between the experiment and simulation, but simulation can predict the increase of the bubble diameter by increasing the Reynolds number.

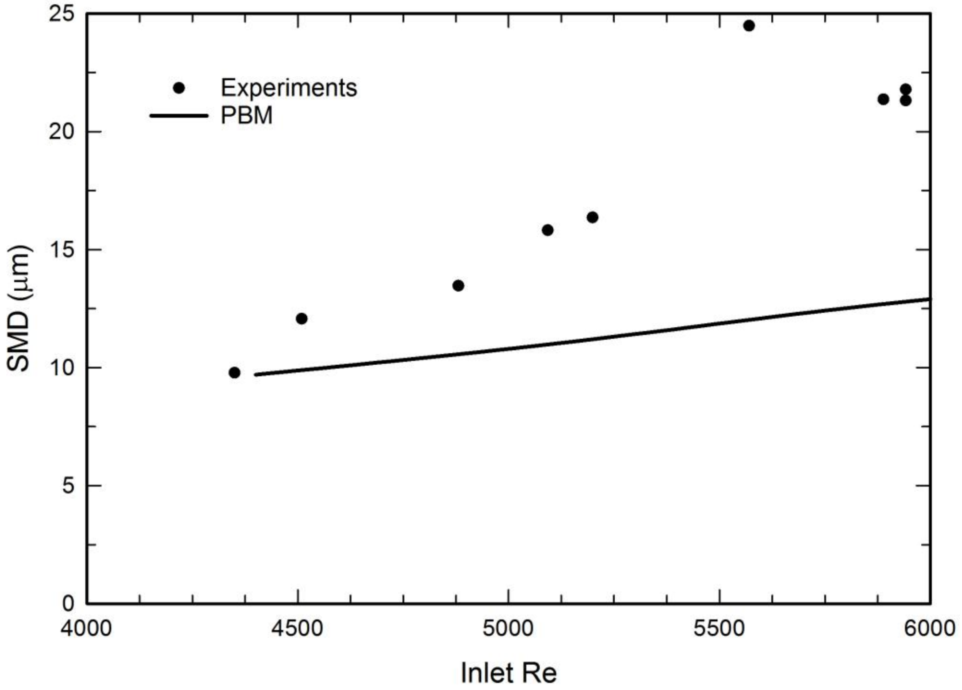

Figure 5.20 Comparison of SMD at 50 mm away from the throat calculated by PBM with the experimental results for ASW

It can be easily interpreted that increasing the flowrate can increase the chance of bubble breakage due to the increase in the shear rate and turbulence. On the other hand, the increase of the velocity will decrease the pressure and increase the bubble sizes and the volume fraction. The increase of bubble radius will result in the higher chance of collision between the bubbles and consequently, higher chance of bubble coalescence would occur. As these two phenomena have opposite effects of each other, three possibilities can happen.

1. Breakage phenomena can be dominant. The result of this case is that the bubble radius decreases, and the number density increases.

2. Coalescence phenomena can be dominant. The result of this case is that the bubble radius increases, and the number density decreases.

3. Coalescence and breakage have the same impact, or negligible effect. In this case the bubble radius and void fraction should not change significantly.

From the results of the simulation it can be concluded that the second case is the one happening in this case study. Therefore, the coalescence is dominant phenomena in the venturi.

In the case of CSW, the bubble size distribution predicted by PBM (Figure 5.21) are very lower (~8 times lower) than the experimental results. This shows the lack of model in correct prediction of the physical phenomena as is happening in the experiments. From the experiments, and observation was that the nucleation process at the beginning of the run is initiated at a higher velocity of the recorded cavitation inception. By reducing the Re number, the nucleation presumes to lower Re at which nucleation initiated. The conclusion that is made based on this observation is that, for the case of CSW, heterogeneous nucleation, i.e. nucleation for a cavity attached to the wall (attached cavity) plays a significant role in the bubble nucleation (Parkin and Kermeen, 1962). Therefore, in our model, except the physical models implemented, a proper model for heterogeneous nucleation is requirement. Unfortunately, due to the lack of proper nucleation model, the PBM cannot be fully representative of the physical phenomena.

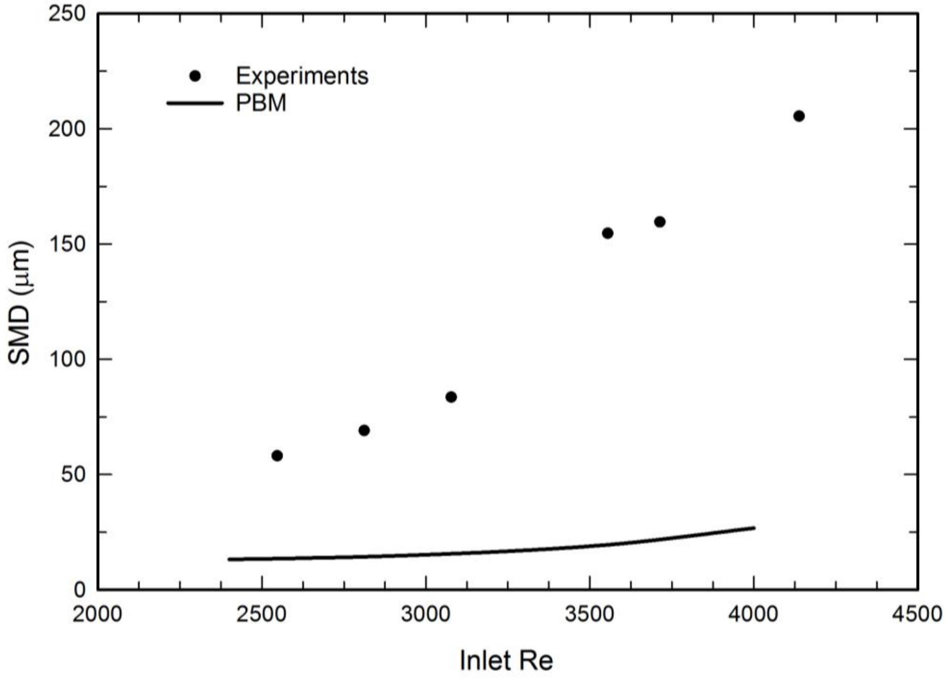

Figure 5.21 Comparison of SMD at 50 mm away from the throat calculated by PBM with the experimental results for CSW

In this section, Population Balance model was implemented to model the bubble coalescence, breakage and growth in case of a cavitation. The Gas diffusion was also included to account the effect of NCG. The results of the simulation were compared with similar cases of experiments, and a good agreement between the results was observed. The difference in BSD comparison can be related to the lack of a proper model for heterogeneous nucleation model. PBM cavitation model can be used in the detail design of any device related to produce micron-size bubbles through the cavitation process, such as a dual bubble generator, HIA cell discussed in Chapter 2. However, for a more detailed study of the fine particle separation using cavitation, we suggest to use the Discrete Bubble Model.

5.4.3. Discrete bubble model

In this model, another approach of studying the cavitation is implemented. Using Lagrangian tracking of the bubbles in the flow, has the advantage of the being able to track each bubble separately and the bubble dynamics can be applied in the most accurate way. Moreover, the particles carrying the nuclei can be marked, and the attachment to the free flotation bubbles can be investigated. On the contrary, the calculation load will be increased significantly depending on the number of bubbles being tracked. The geometry also affects the calculation load as 2D axisymmetry geometry cannot be used because of the collision and coalescence of bubbles being accounted correctly. In the case of coalescence model enables, a 3D mesh of quarter section of the venturi is used (Figure 5.22). Inlet and outlet are quarter circles. Except the inlet, outlet, and wall boundary condition, a symmetry boundary condition is used for the new two planes in the geometry. Therefore, any bubble crossing one of the symmetry planes will enter from the other symmetry plane preserving the momentum. Using symmetry planes, the number of cells and bubbles being tracked are reduced by a factor of 4. This will affect the computational time significantly (~1/16) with negligible effect on the results. To study the effect of grid size on the

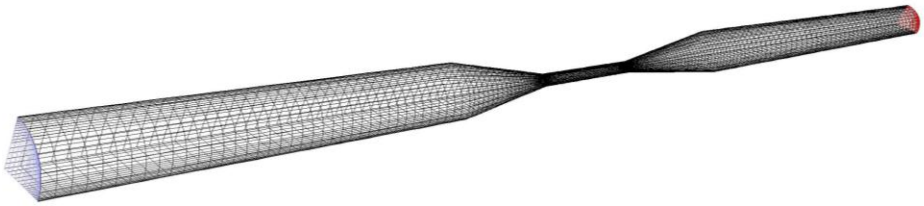

Figure 5.22 3D geometry of the venturi used in DBM

Single phase realizable k-ε turbulence model, with enhanced wall treatment is used for the calculation of the liquid velocity and pressure profiles. Because the coupling the bubbles and the liquid is neglected, to capture the effect of bubbles on the flow, a similar approach to Singhal cavitation model is implemented to compensate this effect on the liquid density and viscosity. Then, the bubbles are released on a plane 10mm before the throat with random distribution on the plane. The bubbles are initialized with the fluid velocity, initial diameter of 10 µm and in physical and chemical equilibrium with the flow. Bubble dynamics, collision/coalescence and breakage models are activated upon the release.

As solution steps, the liquid flow is solved in steady state; then, the solver is switched to transient with Eulerian time step of 1e-2 s. The bubbles injection in to the flow starts at 1s, and a new Eulerian time step of 1e-5s is implemented. The flow is always converged and only one iteration is taken for each time step. The small Eulerian time steps are required as each bubble is marched for the entire Eulerian time step before calculation of the other bubbles path. Therefore, smaller Eulerian time step will increase the accuracy of the bubbles marching together. This is an important criterion when the collision between the bubbles is studied. Each Eulerian time step includes a few Lagrangian time steps for a more accuracy of the bubbles path. Moreover, the bubble dynamics (R-P equation solver) uses a separate time step for accurate calculation of the bubble diameter.

First, it is interesting to study the difference of the various gas diffusion models. Figure 5-23 shows the bubble distribution at the venturi throat, where the lowest pressure exists, for DGW at Re numbers 4800, 5200. The gas diffusion model was disabled. The cavitation inception is observed at Re~5200 with the increase of the bubbles diameter.

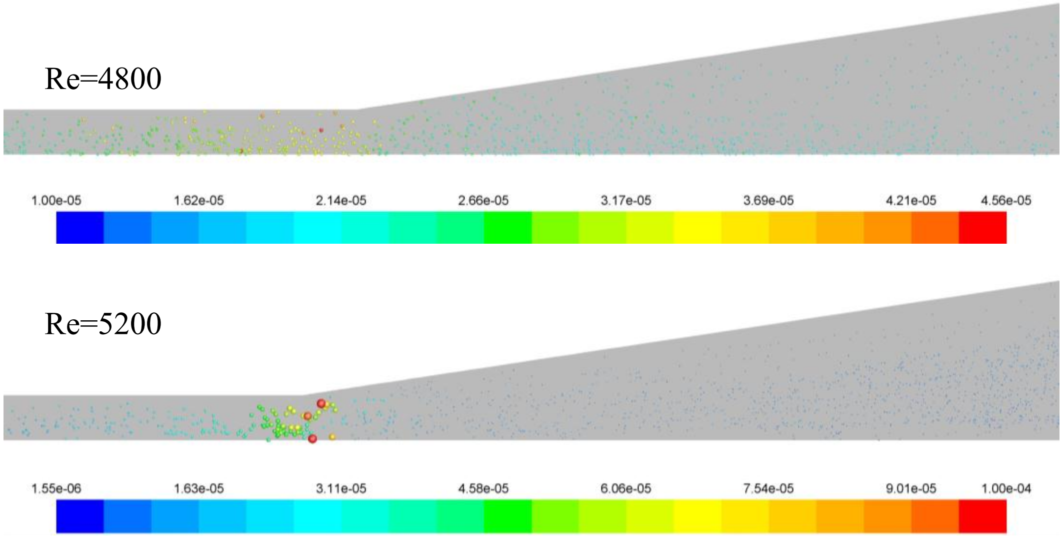

Figure 5.23 Cavitation inception point for DGW in DBM

Next, the BSD from the DBM model was compared with the experimental results for ASW flow. To sample the bubbles after the throat, two sample planes were located 10 and 50 mm after the throat. The diameter and radial location of the bubbles were recorded for 1e-1 s. As the bubbles cross the second sampling plane, they were removed from the domain, to reduce the calculation time. The coupling of the Eulerian liquid phase and Lagrangian gas phase was one-way coupling, i.e. the effect of the liquid flow on the motion of the bubbles was only accounted and the bubbles did not affect the liquid flow. Therefore, the volume fraction is calculated from the sampling plane right after the throat. The volume fraction is calculated as

$$\varepsilon = \frac{\frac{\pi}{6}\sum_{i=1}^{N} D_i^3}{VA\Delta t} \tag{5.25}$$

D_i is the bubble diameter, N is the total number of bubbles crossed the plane, V is the area averaged velocity at the plane, A is the area of the plane, and Δt is the total sampling time. SMD of the sampled bubbles is calculated as

$$\text{SMD} = \frac{\sum_{i=1}^{N} D_i^3}{\sum_{i=1}^{N} D_i^2} \tag{5.26}$$

Similar to the PBM model, the bubbles were injected at initial diameter of 10 µm and total volume fraction of 0.003%. The number of bubbles in the domain was approximately ~2e4, and it could vary depending on the coalescence and breakage frequency. Moreover, the bubbles that were trapped in recirculation flow were removed after 2000 Lagrangian time steps. The IAC and SMD calculated from the sampling plane for ASW are compared to the results from experiments (Figure 5.24 and 5.25).

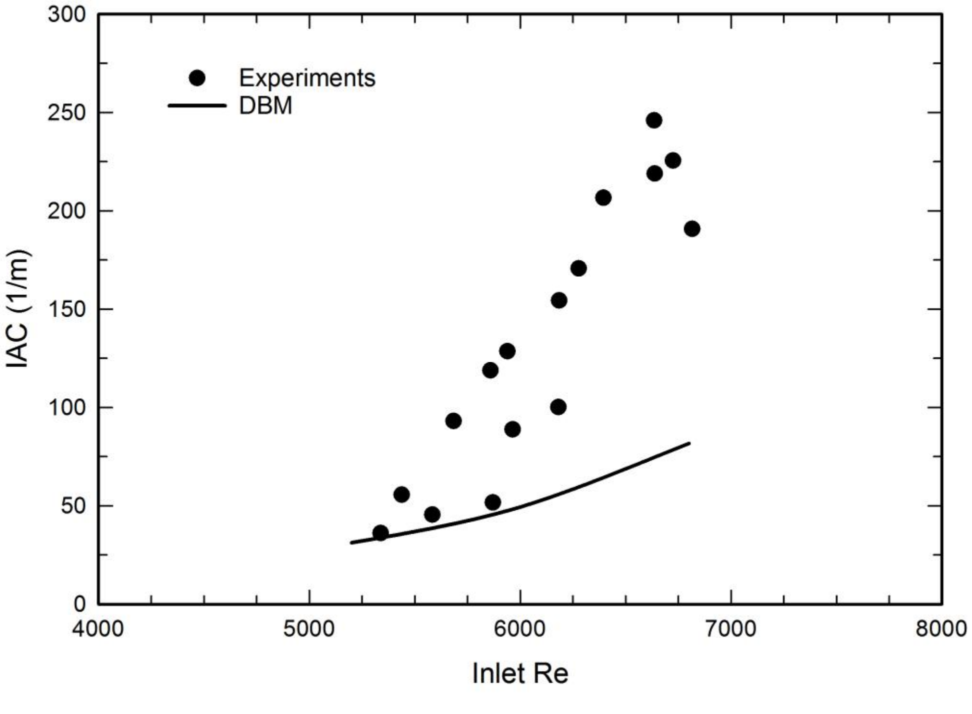

Figure 5.24 Comparison of IAC at 10 mm away from the throat calculated by DBM with the experimental results

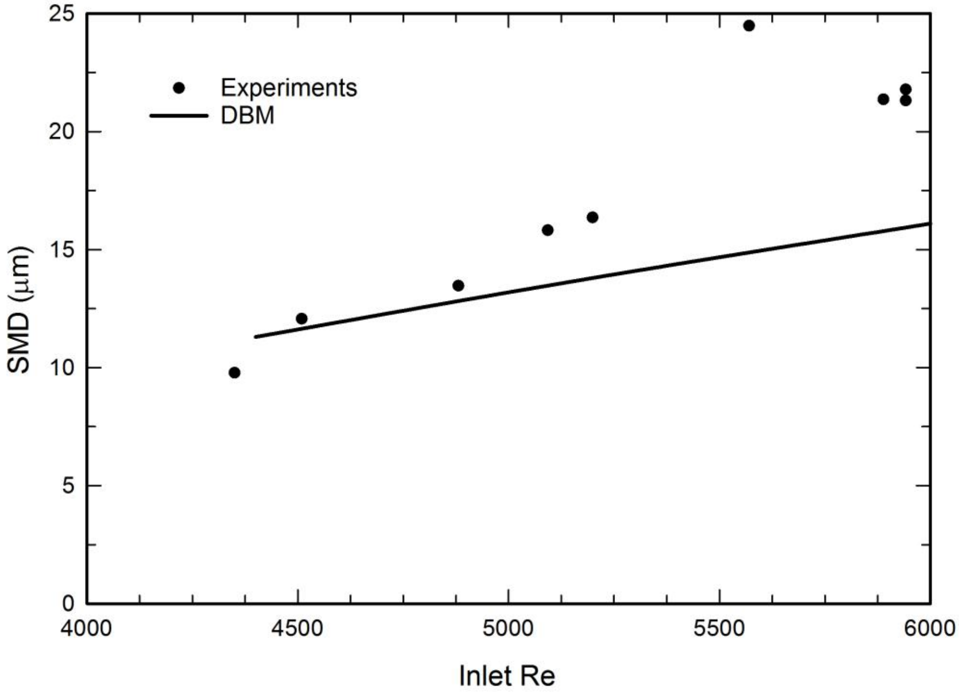

Figure 5.25 Comparison of SMD at 50 mm away from the throat calculated by DBM with the experimental results

The temporal pressure imposed to a bubble and the radius of the bubble are shown in Figure 5.26. It is observed that most of the time of bubble travel is outside the throat at the time. The bubble was released in 0.5 mm away from the wall at ASW water at Re=5200. The gas diffusion rate was calculated from both models used in this study, i.e. numerical solution and Higbie morel. Figure 5.27 shows the comparison of the mass transfer rate calculated from both models. It shows that the magnitude of the gas transfer rate due to the bubble wall velocity can be much higher than the estimated value by the Higbie model.

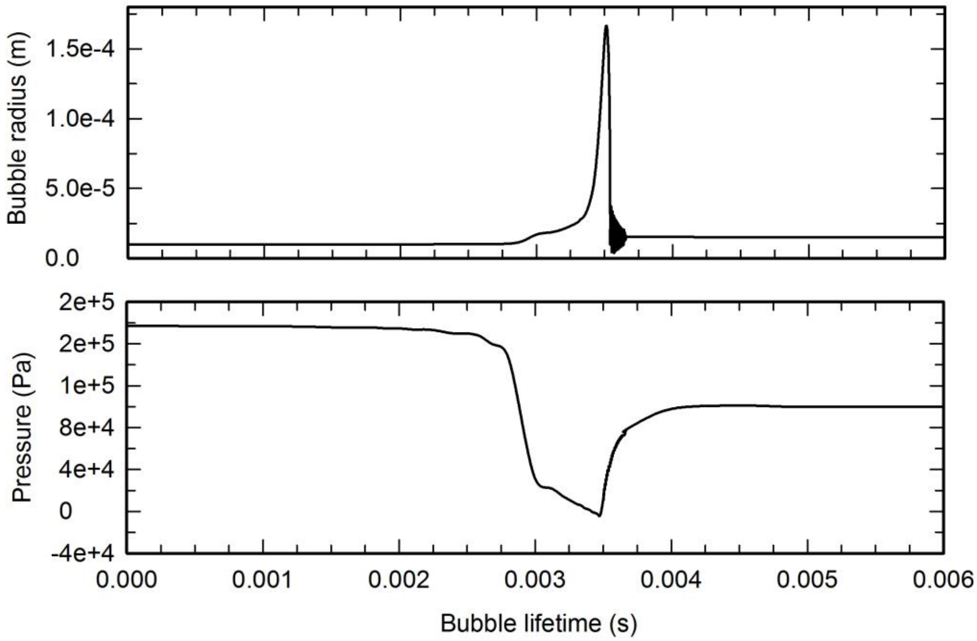

Figure 5.26 Encountered pressure and bubble radius during the flow in the venturi

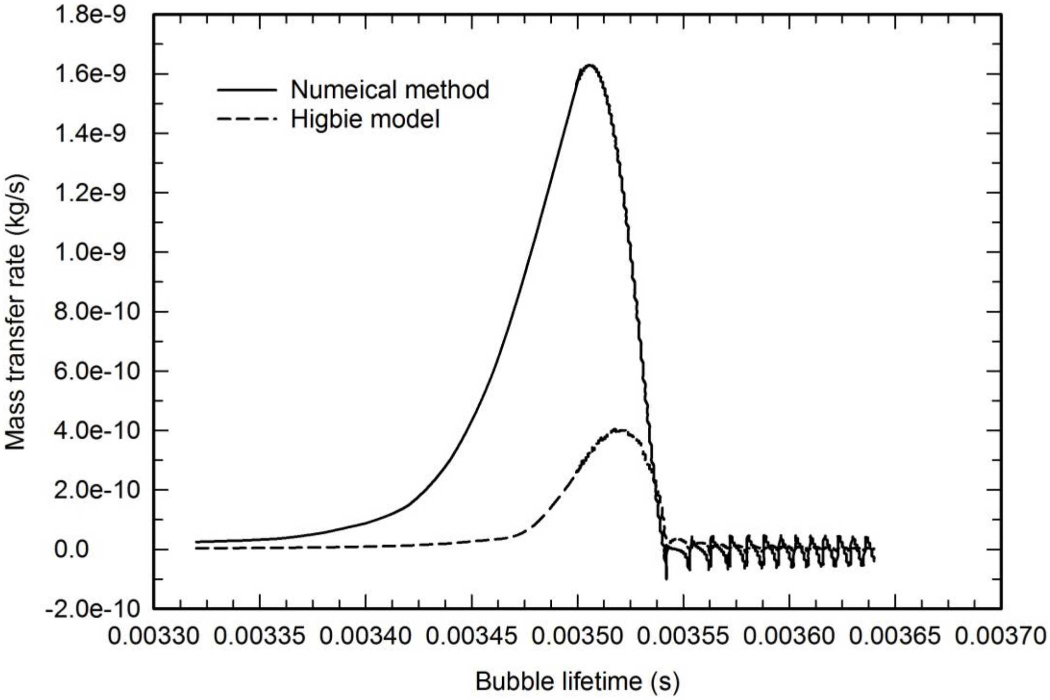

Figure 5.27 Comparison of mass diffusion rates using numerical method and Higbie model

From the DBM results, it is possible to study the coalescence and breakage frequency in the whole domain. The number of coalescence and breakage phenomena were recorded for comparison. Table 5.3 shows the approximate frequency of the coalescence and breakage events occurred during the sampling time. It demonstrates that the coalescence phenomenon was the dominant event in this case study.

Table 5.3 Comparison of the number of coalescence and breakage event frequencies

Re	Event frequency in the domain (1/s)	
	Coalescence	Breakage
4000	~3e3	0
4400	~1e4	~6e2
5200	~2e4	~6e3

5.5. PBM and DBM in dual bubble generator

As discussed in Chapter 1, the intention of this study is to develop a model that can be implemented in the optimization of the design of a device that can enhance the fine particle flotation. In this section, it is interesting to investigate case studies of using the PBM and DBM models developed in this study in the design of a cavitation tube, Dual Bubble Generator (DBG), or High Intensity Agitation (HIA) cell.

As shown in Figure 2.5 in Chapter 2, Tao et al. (2008) proposed the use of a cavitation tube to enhance the fine particle flotation. A cavitation tube was used to grow the bubbles on the surface of the nuclei (carrier bubbles) and cause the bubble to grow. After the carrier bubbles grow in the cavitation tube, they are injected into the flotation column, where the larger flotation size bubbles (free bubbles) exist, and the attachment of the carrier bubbles and free bubbles is related to the recover enhancement. In DBG and HIA cell, similar concept is implemented. The collision rate of the carrier bubbles and the free bubbles can be increased if the free bubbles are injected closer to the region where the carrier bubbles have the maximum diameter. Therefore, in DBG (Figure 5.28), the free bubbles are injected in the venturi instead of using the bubbles in the flotation column.

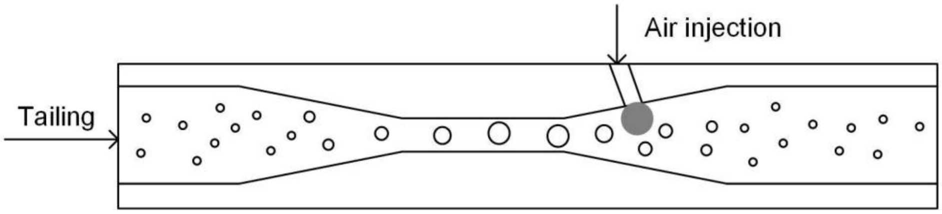

Figure 5.28 Schematic of a dual bubble generator

One of the parameters to be studied in the design of DBG is the location of the air injection to result in maximum particle collection. The proposed PBM and DBM models can be implemented to provide some information regarding this issue. Following, a case study is demonstrated.

In this case study, the same geometry that was used in Section 5.4 was implemented as a hypothetical dimension for DBG. Many parameters such as the length and diameter of the throat, the angle of the expansion region, or the location of the free bubble injection can affect the bubble size distribution at the outlet of the venturi and the probability of the attachment of the free bubbles to the carrier bubbles. As an example, it was investigated to find the best location for injection of free bubbles into the venturi. It is assumed that free bubbles of 200 μm diameter are injected to the venturi at Re=4400.

For every optimization problem, an objective function is defined, and the goal is to maximize the objective function. The probability of coalescence between the injected bubble and the existing bubbles in flow is intended to be calculated according to the Kamp coalescence model as

$$C\left(d,200\mu m\right)=\left(d+200\right)^{2/3}\varepsilon^{1/3}\exp\left(-C_t\left(\frac{d_{eq}}{C_{vm}}\right)^{1/2}\varepsilon^{1/3}\left(d+200\right)^{1/3}\right)\quad(5.27)$$

d is the SMD from the calculations in Section 5.5. All the constant values are removed from the equation. The values of $C(d,200)$ are normalized with the maximum value in the domain. Figure 5.29 shows the contours of the normalized total coalescence efficiency. This figure shows that the maximum value of coalescence efficiency was at the end of the throat. Therefore, it is concluded that the optimum location for the air injection in the venturi is at that location which results the maximum probability of coalescence with the nuclei on the surface of particles flowing from upstream.

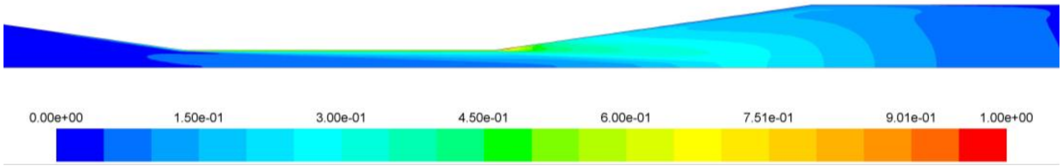

Figure 5.29 Normalized probability of coalescence distribution

For a more detailed study DBM can be implemented to study the path and the coalescence of the carrier and free bubbles as mentioned before. The advantage of DBM is that we can study particles attached to bubbles as nucleation site and study the probability of coalescence with the larger flotation bubbles. Therefore, based on the result of PBM the probability of the coalescence occurring for a 200 μm bubble injected in the flow at the end of the throat, with the bubbles coming from upstream was investigated. At the injection of free bubble, the bubble was assumed in equilibrium with the fluid. For comparison, a bubble was injected 5 mm after the end of the throat on the axis line. For each bubble the number of nuclei (particle carriers) was recorded. The results show that the bubble injected at the end of the throat, coalesced 8 times with the carrier nuclei, and the bubble at 5 mm after the throat coalesced with 3 carrier nuclei. However, at the exit point, the diameter of the bubble released closer to the throat had much smaller diameter than the bubble released further from the throat because the bubble initiated at the throat location

5.6. Summary

In this Chapter, the cavitation models that were explained in Chapter 4 were verified numerically and experimentally. Singhal cavitation model was implemented for water flow through the venturi similar to the Chapter 3 with different gas contents. The model predicted the cavitation inception correctly, although the model lacks justification for the method of implementing the NCG in the model. Then, Population Balance Model was implemented to predict the size distribution of the bubbles that were measured experimentally. The results of BSD were in acceptable range of experiments. Similar results were observed for DBM. At the end of this Chapter, a simple case study as an example of the capabilities of the models for optimizing the DBG design using PBM and DBM was conducted. Although each model has many drawbacks and assumptions that might affect the results, it was shown that current models are capable of predicating major physics involving in the cavitation phenomena with the minimum tuning parameters. Further investigation and validation, certainly, can affect the creditability of the model, which is left for future work.

Chapter 6

Conclusion and Future Work

6.1. Summary and conclusion

The main objective of this study was to develop a CFD model that can be used to investigate the cavitation inception and predict the Bubble Size Distribution (BSD) produced in the cavitation phenomena. The ultimate goal was to use the model in the optimization of cavitation based devices that can enhance the fine particle recovery, based on the concepts discussed in Chapter 2. Because of the complexity, in this project, two phase flow was only studied, and the three phase (including the effect of particles) was left for future studies.

Because of the lack of data on BSD from cavitation in literature, a lab scale experimental setup was prepared. Various methods and commercial devices were tested such as, light intensity measurements method, Mastersizer, FBRM, and ABS. The intention was to estimate the bubble size distribution downstream of cavitation site and the effect of dissolved gases on the BSD. Due to difficulty of this problem, different approaches were examined for comparison. Light transmission method provided the ratio of void fraction over SMD in the measurement volume. The advantage of this method was that it could be used close to the cavitation site. Mastersizer provided the bubble size distribution and the volume fraction of the bubbles with high accuracy (1%). However, the changes in flow pattern might result in change of size distribution originated from the venturi. Moreover, to gain the high accuracy, the volume fraction should be in a certain range. Therefore, it had limited usage in our experiments. FBRM, also, provided the size distribution, but it could not measure the total volume fraction or number density. Because it only measures the size of the bubbles passing close to its window, and counts the number of bubbles per second. Moreover, Acoustic Bubble Spectrometer (ABS), a device to measure BSD based on acoustic principles manufactured by Dynaflow Inc., was tested for in-line measurement of BSD. However, the device was not capable of measuring the BSD because of the noise from collapsing bubbles interfering with the acoustic signals emitted from the device in the flow.

Next the cavitation models that can capture the cavitation inception and BSD were investigated. Singhal cavitation model (Singhal et al., 2001) is the only model that includes the effect of Non-Condensable Gases (NCG). However, Singhal model is only used to predict the vapor volume fraction. Therefore, two available approaches, Eulerian (PBM) and Lagrangian (DBM), were implemented in ANSYS-Fluent, for modeling of cavitation and bubble size distribution. This study is one of the first studies on the development of the cavitation model using PBM. Moreover, Fluent package does not include a cavitation model using the Lagrangian (DBM) approach. Therefore, some of the basic related physical models were incorporated into the software using User Defined Functions (UDF) based on the importance and time limitation. Further improvements are suggested in Section 6.2 as future work. Details of the three discussed models are available in Chapter 4.

In Chapter 5, first, the models that have been implemented in Chapter 4 as UDF were studied in case studies to verify the correct implementation and validate the individual models with the available experiments. In DBM model, the main challenge is the computational time. As the base software (Fluent) used in this study is well advanced in parallel processing, proposed DBM model can speed up in calculations. However, the developed DBM model at this stage can only be executed on single processor. Therefore, it can be applied at small geometries and small number of bubbles. Further information is provided in future work.

In Chapter 5, many challenges and issues were investigated, and best possible solutions were proposed. Some of the findings in this section were:

1. The well-known Rayleigh-Plesset (R-P) equation was found to be a real challenge due to the stiffness of the ODE in the bubble collapse region. An explicit time stepping method was required that could solve the R-P equation with very small time steps (as low as 1e-19s) in the bubble collapse region, and march the bubble at other stages with larger time step (1e-7 s). If the solver could not change the time steps sharply, either the solution would diverge or would take impractical calculation time. A novel method of controlling time step, based on the concept of PID controller, was implemented and optimized to solve the R-P in minimum time steps in the controllable accuracy.
2. Diffusion model for DBM was another challenge, as the solution is time consuming, and increases the computational time for large number of bubbles significantly. Therefore, the two available methods of solution, i.e. solving diffusion equation numerically and Plesset-Zwick (P-Z) approximate analytical solutions, were implemented and the calculation times were studied. It was found that the numerical solution of the diffusion problem with 20 nodes had less than 1% difference with bigger number of nodes, and it was less time-consuming than the P-Z solution for large number of time steps. The solution method was validated with the experimental result in a case of rectified diffusion.
3. The other model that is very important in the cavitation model is the coalescence model. There are few coalescence models available in the literature for different conditions of bubbly flow. A case study was conducted for comparison of the coalescence models with the experimental results from literature. Among the few coalescence models

available from literature, Prince and Blanch (1990), Luo and Svendsen (1996), and Kamp et al. (2001) models were implemented alone in PBM, and were compared to a very simple experiment that included the bubbly flow in straight pipe and coalescence occurring among the bubbles in the system. The results of three models were compared, and Kamp model had better agreement compared to the other two models, which had very similar results. Therefore, the Kamp model was implemented in PBM cavitation model.

4. The same case study for coalescence models in PBM was studied with the DBM. In this case the turbulence model was the subject of study. Initial results from *k-ε* model showed that a turbulent dispersion model is mandatory for the proper study of bubble collisions and coalescence in the flow. The Gosman and Ioannides (1983) random walk model was implemented. The results of the BSD comparison with the experiments were improved compared to *k-ε* standalone model. It was concluded that the instantaneous velocity fluctuation is a crucial parameter in the correct coalescence prediction. For further investigations the LES model was implemented as LES model, after Direct Numerical Simulation (DNS) is the most accurate method of predicting the instantaneous velocity profile and fluctuations. The results were extremely improved and a very good agreement between the numerical results and the experiment was obtained. It was concluded that for the most accuracy of the bubble motion in the liquid, LES model is required.

In the rest of Chapter 5, the results of the full cavitation models were validated with experimental results from in-house setup explained in Chapter 3. The Singhal cavitation model was found to have good prediction of the cavitation inception at different concentrations of NCG. PBM model had the advantage of the better prediction of pressure drop in the studied venturi over the Singhal model. PBM and DBM had acceptable agreement in prediction of Interfacial Area Concentration (IAC) values at different velocities, as the difference increases at higher Re numbers, and predicted correct trend for the Sauter Mean Diameter changes versus the Re numbers. However, the level of changes predicted by the models is different from the experimental results. The reason for this can be related to the challenge number 5 explained in this chapter. As at the higher flowrates, the fluctuations of the bubbles are more intense, and the collision and coalescence rate is strongly affected by the turbulent dispersion model or turbulence model implemented in the problem. Therefore, as the solution for better prediction, we propose that LES turbulent model be implemented in the study of the motion of bubbles in the venturi. Moreover, in this study no heterogeneous nucleation model was implemented because of the reason mentioned before. However, it is suggested that attached cavities to the venturi wall can be a source of bubbles (Brennen, 1195). These cavities can be occasionally or permanently attached to the wall. The growth of these cavities can be results of NCG diffusion or vapor. Based on the comparison of the modeling and experimental results, it can be concluded that the attached cavities are inevitable, especially if the boundary layer separation is close to the low pressure region (which occurs in most cases). In the design of Dual Bubble Generator (DBG), the intention is to nucleate bubbles on the surface of the particles and prevent the formation of attached cavities on the surface of the DBG. We proposed that the location of the attached cavity in DBG can be used as the location of air bubble injections to produce flotation size bubbles. The PBM and DBM were implemented in a case study in Dual Bubble Generator (DBG), for parametric study of the design factors for a DBG. This study was a primary step to our ultimate goal which is to develop a system that is optimized to enhance the attachment of fine particles to bigger flotation bubbles. This study, also, showed that the coalescence of the carrier bubbles with a free bubble is at maximum value in the mentioned location.

6.2. Recommendations

In this section, three major recommendations are proposed to improve the proposed CFD models.

First, as explained in Section 6.1, the turbulence model and turbulent dispersion models are crucial in correct BSD prediction. Therefore, it is interesting to implement the DBM model with LES turbulence model to investigate the improvements of the BSD prediction. However, the challenge is the time requirements for the LES model due to the big grid size required. This challenge can be compensated with the parallel processing available in Fluent and the use of clusters available to the researchers, such as SHARCNET in Canada.

Second, the use of four-way coupling can improve the results and the model can be verified on the available experimental data from literature for pressure profiles in cavitating flows.

Third, a method of averaging can be applied for the bubbles that become bigger than the size of the grid that they are located. Therefore, instead of using the pressure value of the liquid at the center of the bubble, the average of the pressure values at the surface of the bubble can be used. The surface averaging can affect the bubble dynamics, significantly if the bubble is passing through a region with high gradient of pressure and velocity over the length scale of the bubble diameter, such as sharp corners in the geometry.

6.3. Future work

The models that have been proposed in this study can be improved furthermore. Some of the recommendations proposed can have significant improvement on the results. Models at current level are also capable of capturing most of the physics in the cavitation phenomena, and can be implemented in optimization of different cavitation related instruments to enhance the fine particle flotation.

Moreover, a cavitation model was developed theoretically that inherits the PBM method of cavitation modeling and can account the gas diffusion and effect of NCG on the cavitation inception. It implements the gas density in compressible form. In Singhal cavitation model, it accounts the effect of NCG by assuming that the total gas content behaves as gas phase in the solution. However, in reality, the gas content is the amount of gas dissolved in the liquid phase. Therefore, application of gas density to the NCG is a wrong assumption. From the PBM model used in this study, a new cavitation model was interpreted that is interesting to be studied in future. The cavitation model proposed is similar to the cavitation model proposed by Yuan and Schnerr (2001) which uses the R-P equation to evaluate the exchange rate, but it assumes that the number density of bubbles per pure liquid is constant. The difference of this model with Yuan and Schnerr (2012) model is that it does not use the assumption of the constant density for the vapor phase, and considers cavitation occurring from the free nuclei existing in the free stream. Similar to other cavitation models, a mixture model is used as multiphase. The mass transfer rate as shown in Appendix B is calculated as:

$$R_e = \frac{\rho_v \rho_l}{\rho_m} \alpha (1-\alpha) \left(\frac{Dm}{m} \right) \tag{6.1}$$

where D_m is the mass exchange rate to a single bubble with mass m, and includes the mass transfer to a bubble including liquid vapor, and NCG dissolved in the liquid phase. The mass exchange rate for NCG gas diffusion and vaporization of the liquid can be calculated as:

$$Dm_{NCG} = k_{Diff} A (P_0 - P_l) \tag{6.2}$$

$$Dm_{Vap} = k_{Vap} A (P_v - P_l) \tag{6.3}$$

P_0 is the initial saturation pressure of the liquid with NCG, P_l is the local liquid pressure, and P_v is the vapor pressure of the liquid. k_{Diff} is calculated as:

$$k_{Diff} = 0.3\sqrt{D}\left(\frac{\varepsilon}{\nu}\right)^{\frac{1}{4}} HM \tag{6.4}$$

D is the gas diffusion coefficient in the liquid phase, ε is the energy dissipation rate, υ is the kinematic viscosity, H is the Henry constant, and M is the gas molecular weight. k_{Vap} is calculated as:

$$k_{Vap} = \sqrt{\frac{M}{2\pi RT}} \tag{6.5}$$

R is universal gas constant, and T is the temperature.

References

Ahmed, N. and Jameson, G. 1985, "The effect of bubble size on the rate of flotation of fine particles", *International Journal of Mineral Processing,* vol. 14, no. 3, pp. 195-215.

Alehossein, H. and Qin, Z. 2007, "Numerical analysis of Rayleigh-Plesset equation for cavitating water jets", *International Journal for Numerical Methods in Engineering,* vol. 72, no. 7, pp. 780-807.

Alopaeus, V., Koskinen, J., Keskinen, K.I., Majander, J. 2002, "Simulation of the population balances for liquid–liquid systems in a nonideal stirred tank. Part 2-parameter fitting and the use of the multiblock model for dense dispersions", *Chemical Engineering Science,* 57, pp. 1815-1825.

AN, C.M. 1999, "On the breakup of an air bubble injected into a fully developed turbulent flow. Part 1. Breakup frequency", *J.Fluid Mech,* vol. 401, pp. 157-182.

Antal, S., Lahey, R. and Flaherty, J. 1991, "Analysis of phase distribution in fully developed laminar bubbly two-phase flow", *International Journal of Multiphase Flow,* vol. 17, no. 5, pp. 635-652.

Blander, M. and Katz, J.L. 1975, "Bubble nucleation in liquids", *AIChE Journal,* vol. 21, no. 5, pp. 833-848.

BRENNEN, C. 1995, "Cavitation and bubble dynamics", Oxford University Press, New York, USA.

Colin, C., Fabre, J. and Dukler, A. 1991, "Gas-liquid flow at microgravity conditions—I. Dispersed bubble and slug flow", *International Journal of Multiphase Flow,* vol. 17, no. 4, pp. 533-544.

Coulaloglou, C. and Tavlarides, L. 1976, "Drop size distributions and coalescence frequencies of liquid-liquid dispersions in flow vessels", *AIChE Journal,* vol. 22, no. 2, pp. 289-297.

Crum, L.A. 1980, "Air Bubble Growth by Rectified Diffusion".

Dai, Z., Fornasiero, D. and Ralston, J. 2000, "Particle–bubble collision models—a review", *Advances in Colloid and Interface Science,* vol. 85, no. 2, pp. 231-256.

De Bertodano, Martin A Lopez, 1998, "Two fluid model for two-phase turbulent jets", *Nuclear Engineering and Design,* vol. 179, no. 1, pp. 65-74.

Dellanoy, Y. and Kueny, J. 1990, "Two phase flow approach in unsteady cavitation modeling", *Cavitation and Multiphase Flow Forum*, pp. 153.

Epstein, c.e.P. and Plesset, M.S. 1950, "On the Stability of Gas Bubbles in Liquid-Gas Solutions", *The Journal of chemical physics,* vol. 18, no. 11, pp. 1505-1509.

Farrell, K.J. 2003, "Eulerian/Lagrangian analysis for the prediction of cavitation inception", *Journal of fluids engineering,* vol. 125, no. 1, pp. 46-52.

Finch, J. and Hardie, C. 1999, "An example of innovation from the waste management industry: deinking flotation cells", *Minerals Engineering,* vol. 12, no. 5, pp. 467-475.

Fox, F.E. and Herzfeld, K.F., 1954, "Gas bubbles with organic skin as cavitation nuclei", *The Journal of the Acoustical Society of America*, vol. 26. no. 6, pp.984-989.

Franc, J. and Michel, J. 2006, "Fundamentals of cavitation", *Springer Science and Business Media*.

Fuerstenau, M.C., Jameson, G.J. and Yoon, R. 2007, *Froth flotation: a century of innovation,* SME.

Giannadakis, E., Gavaises, M., Roth, H. and Arcoumanis, C. 2004, "Cavitation modelling in single-hole diesel injector based on Eulerian-Lagrangian approach", *Proc. THIESEL International Conference on Thermo-and Fluid Dynamic Processes in Diesel Engines. Valencia, Spain*.

Hairer, E. and Wanner, G. 1996, "Solving ordinary differential equations ii: Stiff and differential-algebraic problems", second edition, Springer series in computational mathematics.

Hart, G., Morgan, S. and Bramall, N. 2002, "Generation of picobubbles in flotation feed—A means to reduce collector use", *Proceedings of Ninth Australian Coal Preparation Conference, ed. by Yeppoon*, pp. 136.

Harvey, E.N., Whiteley, A., McElroy, W., Pease, D. and Barnes, D. 1944, "Bubble formation in animals. II. Gas nuclei and their distribution in blood and tissues", *Journal of Cellular and Comparative Physiology,* vol. 24, no. 1, pp. 23-34.

Holl, J.W. 1970, "Nuclei and cavitation", *Journal of Basic Engineering,* vol. 92, no. 4, pp. 681-688.

Hsiao, C. and Chahine, G. 2004, "Prediction of tip vortex cavitation inception using coupled spherical and nonspherical bubble models and Navier–Stokes computations", *Journal of Marine Science and Technology,* vol. 8, no. 3, pp. 99-108.

HSIAO, C. and Chahine, G.L. 2012, "Effect of a propeller and gas diffusion on bubble nuclei distribution in a liquid", *Journal of Hydrodynamics, Ser.B,* vol. 24, no. 6, pp. 809-822.

Hsiao, C. and Pauley, L.L. 1999, "Study of tip vortex cavitation inception using Navier-Stokes computation and bubble dynamics model", *Journal of fluids engineering,* vol. 121, no. 1, pp. 198-204.

Ilinskii, Y.A., Wilson, P.S. and Hamilton, M.F. 2008, "Bubble growth by rectified diffusion at high gas supersaturation levels", *The Journal of the Acoustical Society of America,* vol. 124, no. 4, pp. 1950-1955.

Jamialahmadi, M., Branch, C. and Müller-Steinhagen, H. 1994, "Terminal bubble rise velocity in liquids", *Chemical engineering research and design,* vol. 72, no. 1, pp. 119-122.

Kail, N., Marquardt, W. and Briesen, H. 2009, "Process analysis by means of focused beam reflectance measurements", *Industrial and Engineering Chemistry Research,* vol. 48, no. 6, pp. 2936-2946.

Kamp, A., Chesters, A., Colin, C. and Fabre, J. 2001, "Bubble coalescence in turbulent flows: a mechanistic model for turbulence-induced coalescence applied to microgravity bubbly pipe flow", *International Journal of Multiphase Flow,* vol. 27, no. 8, pp. 1363-1396.

Kubota, A., Kato, H. and Yamaguchi, H. 1992, "A new modelling of cavitating flows: a numerical study of unsteady cavitation on a hydrofoil section", *Journal of Fluid Mechanics,* vol. 240, pp. 59-96.

Laufer, J. 1954, "The structure of turbulence in fully developed pipe flow".

Li, H. 2014, "Role of Hydrodynamic Cavitation in Fine Particle Flotation." University of Alberta, Edmonton. Master of Science Thesis

Lockett, M. and Safekourdi, A. 1977, "Light transmission through bubble swarms", *AIChE Journal,* vol. 23, no. 3, pp. 395-398.

Löfstedt, R., Barber, B.P. and Putterman, S.J. 1993, "Toward a hydrodynamic theory of sonoluminescence", *Physics of Fluids A: Fluid Dynamics (1989-1993),* vol. 5, no. 11, pp. 2911-2928.

Lubetkin, S.D. 1994, "Bubble nucleation and growth", *Butterworth-Heinemann Ltd, Oxford*, pp. 159-190.

Luo, H. and Svendsen, H.F. 1996, "Theoretical model for drop and bubble breakup in turbulent dispersions", *AIChE Journal,* vol. 42, no. 5, pp. 1225-1233.

Mariaux, S. and Achard, J. 1988, "A light transmittance probe for interfacial area measurements of dispersed two phase flows with small particles", *Experiments in Fluids,* vol. 6, no. 7, pp. 467-476.

Markatos, N. and Singhal, A. 1982, "Numerical analysis of one-dimensional, two-phase flow in a vertical cylindrical passage", *Advances in Engineering Software (1978),* vol. 4, no. 3, pp. 99-106.

MARTÍNEZ-BAZÁN, C., Montanes, J. and Lasheras, J.C. 1999, "On the breakup of an air bubble injected into a fully developed turbulent flow. Part 2. Size PDF of the resulting daughter bubbles", *Journal of Fluid Mechanics,* vol. 401, pp. 183-207.

McLaughlin, C. and Rushton, J. 1973, "Interfacial areas of liquid-liquid dispersions from light transmission measurements", *AIChE Journal,* vol. 19, no. 4, pp. 817-822.

Miettinen, T., Ralston, J. and Fornasiero, D. 2010, "The limits of fine particle flotation", *Minerals Engineering,* vol. 23, no. 5, pp. 420-437.

Narsimhan, G., Gupta, and J.P., Ramkrishna, D. 1979, "A model for transitional breakage probability of droplets in agitated lean liquid–liquid dispersions", *Chemical Engineering Science*, vol. 34, pp. 257–265.

Parkin B. R., and Kermeen R. W. 1963, "The Roles of Convective Air Diffusion and Liquid Tensile Stresses During Cavitation Inception", *Proc. IAHR Symp. on Cav. and Hyd. Mach.*, Sendai, Japan.

Plesset, M. and Zwick, S.A. 1954, "The growth of vapor bubbles in superheated liquids", *Journal of Applied Physics,* vol. 25, no. 4, pp. 493-500.

Prince, M.J. and Blanch, H.W. 1990, "Bubble coalescence and break-up in air-sparged bubble columns", *AIChE Journal,* vol. 36, no. 10, pp. 1485-1499.

Qi, Y., Klausner, J.F. and Mei, R. 2004, "Role of surface structure in heterogeneous nucleation", *International Journal of Heat and Mass Transfer,* vol. 47, no. 14, pp. 3097-3107.

Rodrigues, R.T. and Rubio, J. 2007, "DAF–dissolved air flotation: Potential applications in the mining and mineral processing industry", *International Journal of Mineral Processing,* vol. 82, no. 1, pp. 1-13.

Ryan, W.L. and Hemmingsen, E.A. 1993, "Bubble formation in water at smooth hydrophobic surfaces", *Journal of colloid and interface science,* vol. 157, no. 2, pp. 312-317.

Schiller, L., Naumann, A. 1933, "Uber die grundlegenden berechungen bei der schwerkraftaufbereitung", *Vereines Deutscher Ingenieure* 77, 318–320.

Schmidt, D.P., Rutland, C.J. and Corradini, M.L. 1999, "A fully compressible, two-dimensional model of small, high-speed, cavitating nozzles", *Atomization and sprays,* vol. 9, no. 3.

Schmidt, D.P., Rutland, C.J. and Corradini, M. 1997, "A numerical study of cavitating flow through various nozzle shapes", (No. 971597). SAE Technical Paper

Senocak, I. and Shyy, W. 2004, "Interfacial dynamics-based modelling of turbulent cavitating ows, Part-1: Model development and steady-state computations", *International Journal for Numerical Methods in Fluids,* vol. 44, pp. 975-995.

Shams, E., Finn, J. and Apte, S.V. 2011, "A numerical scheme for Euler–Lagrange simulation of bubbly flows in complex systems", *International Journal for Numerical Methods in Fluids*, 67(12), pp.1865-1898.

Sigsbee, R. and Pound, G. 1967, "Heterogeneous nucleation from the vapor." *Advances in Colloid and Interface Science,* 1 (3): 335-390.

Singh, R., Subba Rao, S., Maulik, S. and Chakravorty, N. 1997, "Fine particles flotation-Recent trends", *Transactions of the Indian Institute of Metals,* vol. 50, no. 5, pp. 407-419.

Singhal, A.K., Athavale, M.M., Li, H. and Jiang, Y. 2002, "Mathematical basis and validation of the full cavitation model", *Journal of fluids engineering,* vol. 124, no. 3, pp. 617-624.

Song, S., Lopez-Valdivieso, A., Reyes-Bahena, J. and Lara-Valenzuela, C. 2001, "Floc flotation of galena and sphalerite fines", *Minerals Engineering,* vol. 14, no. 1, pp. 87-98.

Song, S., Lopez-Valdivieso, A. and Reyes-Bahena, J. 1999, "Hydrophobic flocculation applied to fine mineral and coal processing", *XXIII Congress AIMMGM*, pp. 1.

Subrahmanyam, T. and Forssberg, K.E. 1990, "Fine particles processing: shear-flocculation and carrier flotation—a review", *International Journal of Mineral Processing,* vol. 30, no. 3, pp. 265-286.

Tao, D. 2005, "Role of bubble size in flotation of coarse and fine particles—a review", *Separation Science and Technology,* vol. 39, no. 4, pp. 741-760.

Tao, D., Yu, S., Zhou, X., Honaker, R. and Parekh, B. 2008, "Picobubble column flotation of fine coal", *International Journal of Coal Preparation and Utilization,* vol. 28, no. 1, pp. 1-14.

Tao, Y., Liu, J., Yu, S. and Tao, D. 2006, "Picobubble enhanced fine coal flotation", *Separation Science and Technology,* vol. 41, no. 16, pp. 3597-3607.

Trahar, W. and Warren, L. 1976, "The flotability of very fine particles—a review", *International Journal of Mineral Processing,* vol. 3, no. 2, pp. 103-131.

Venneker, B.C., Derksen, J.J. and Van den Akker, Harrie E.A. 2002, "Population balance modeling of aerated stirred vessels based on CFD", *AIChE Journal,* vol. 48, no. 4, pp. 673-685.

Wang, G. and Ostoja-Starzewski, M. 2007, "Large eddy simulation of a sheet/cloud cavitation on a NACA0015 hydrofoil", *Applied Mathematical Modelling,* vol. 31, no. 3, pp. 417-447.

Ward, C., Balakrishnan, A. and Hooper, F. 1970, "On the thermodynamics of nucleation in weak gas-liquid solutions", *Journal of Basic Engineering,* vol. 92, no. 4, pp. 695-701.

Warren, L.J. 1975, "Shear-flocculation of ultrafine scheelite in sodium oleate solutions", *Journal of colloid and interface science,* vol. 50, no. 2, pp. 307-318.

Weber, M. and Paddock, D. 1983, "Interceptional and gravitational collision efficiencies for single collectors at intermediate Reynolds numbers", *Journal of colloid and interface science,* vol. 94, no. 2, pp. 328-335.

Wei, S., Hu, Y., Dai, J. and Liu, R. 2006, "Observation of fine particle aggregating behavior induced by high intensity conditioning using high speed CCD", *Transactions of Nonferrous Metals Society of China,* vol. 16, no. 1, pp. 198-202.

Wilt, P. 1986, "Nucleation rates and bubble stability in water-carbon dioxide solutions", *Journal of colloid and interface science,* vol. 112, no. 2, pp. 530-538.

Wu, C., Nesset, K., Masliyah, J. and Xu, Z. 2012, "Generation and characterization of submicron size bubbles", *Advances in Colloid and Interface Science,* vol. 179, pp. 123-132.

Yang, J., Duan, J., Fornasiero, D. and Ralston, J. 2003, "Very small bubble formation at the solid-water interface", *The Journal of Physical Chemistry B,* vol. 107, no. 25, pp. 6139-6147.

Yoon, R. 1993, "Microbubble flotation", *Minerals Engineering,* vol. 6, no. 6, pp. 619-630.

Yoon, R. and Luttrell, G. 1986, "The effect of bubble size on fine coal flotation", *Coal Preparation,* vol. 2, no. 3, pp. 179-192.

Yuan, W., Sauer, J. and Schnerr, G.H. 2001, "Modeling and computation of unsteady cavitation flows in injection nozzles", *Mécanique and industries,* vol. 2, no. 5, pp. 383-394.

Zhou, Z., Xu, Z., Finch, J., Hu, H. and Rao, S. 1997, "Role of hydrodynamic cavitation in fine particle flotation", *International Journal of Mineral Processing,* vol. 51, no. 1, pp. 139-149.

Zhou, Z., Xu, Z., Finch, J., Masliyah, J. and Chow, R. 2009, "On the role of cavitation in particle collection in flotation–A critical review. II", *Minerals Engineering,* vol. 22, no. 5, pp. 419-433.

Appendix A

For four-way coupling, the liquid volume fraction at each cell is calculated, and is implemented in the density and viscosity of the liquid in continuity, momentum and turbulence equations. Therefore, the density and viscosity of the liquid will be replaced by the fractional value i.e.

$$\rho_l \to \alpha_l \rho_l \, , \mu_l \to \alpha_l \mu_l \tag{7.1}$$

The volume fraction of the liquid in each cell is the subtraction of the volume occupied by the bubbles from the cell volume. Therefore, if there are n_{Bub} number of bubbles in a control volume of V_{cv} the liquid volume fraction can be calculated as:

$$\alpha_l = 1 - \frac{1}{\Delta t_E V_{cv}} \sum_{t}^{t+\Delta t_E} \sum_{i=1}^{n_{Bub}} \frac{4}{3} \pi R_{i,\tau}^3 \Delta t_L \tag{7.2}$$

where Δt_L and Δt_E are the Lagrangian and Eulerian time steps, respectively. If the bubble volume is larger than volume of the control volume, the bubble volume is distributed among the neighbor cells. The volume fraction of the cell occupied by the bubbles is calculated using the following function based on the distance of center of the cell to the center of the bubble:

$$\alpha_g = \frac{1}{1 + \left| \dfrac{X}{R_b} \right|^a} \tag{7.3}$$

where X is the distance between the centers of the bubble and the cell, R_b is the bubble radius, and a is a constant which controls the slope of the function at R_b, set to 100. The accuracy of this function to conserve the mass of the bubble in the domain depends on the ratio of the bubble radius to the cell length scale and the slope of the function at $X=R_b$.

The momentum source is the integration of forces imposed on the liquid from the bubbles. Therefore, the source term for each cell is calculated by integrating the forces on the bubbles inside each cell along time as:

$$\overline{S}_{mom} = \frac{-1}{\Delta t_E V_{cv}} \sum_{t}^{t+\Delta t_E} \sum_{i=1}^{n_{Bub}} M_{i,\tau} \frac{dv_b}{dt} \Delta t_L \tag{7.4}$$

where $M_{i,\tau}$ is the i^{th} bubble mass at time τ, and v_b is the bubble velocity. The bar sign for the source term indicates temporal averaging. The source terms for k and ε can be calculated as:

$$S_k = \overline{u_g . S_{mom}} - v_l . \overline{S_{mom}} \tag{7.5}$$

$$S_\varepsilon = C_\varepsilon \frac{\varepsilon_l}{k_l} S_k \tag{7.6}$$

In case the bubbles are bigger than the cell, the source terms are distributed among the neighbor cells as:

$$S_{cv} = \frac{S_T}{V_b} \alpha_g \tag{7.7}$$

where S_T is the total source term calculated for the cell that bubble exist, V_b is the bubble volume, and α_g is the gas (bubble) volume fraction in neighbor cells.

The solution of Eulerian and Lagrangian phase includes the following steps:

1. New bubbles are initiated in the domain.
2. The fluid is iterated to a converged solution at time t+ΔtE.
3. The forces on the bubbles are estimated, and time step is calculated as Δt=min(Δtmax, τb), where τb is bubble relaxation time, and Δtmax is set to 1e-6 s.
4. The bubble new position and velocity is calculated.

5. Bubble dynamics, breakage, coalescence wall boundary condition calculations are executed. For bubble dynamics, a novel adaptive time stepping method is implemented to integrate the R-P equation in the Lagrangian time step (ΔtL).
6. The liquid volume fraction and source terms are computed.
7. The Lagrangian steps (3-6) are repeated to reach the fluid time.
8. The new volume fraction and source terms are imported in to the fluid transport equations.

Appendix B

In the proposed model, similar to Singhal cavitation model, two transport equations for each phase are written as:

$$\frac{\partial}{\partial t}\left(\alpha_v \rho_v\right)+\nabla.\left(\alpha_v \rho_v \vec{v}_v\right)=R \quad (8.1)$$

$$\frac{\partial}{\partial t}\left(\alpha_l \rho_l\right)+\nabla.\left(\alpha_l \rho_l \vec{v}_l\right)=-R \quad (8.2)$$

where α_l=1-α_v. For the gas phase the equation can be expanded as:

$$\rho_v \frac{\partial \alpha_v}{\partial t}+\alpha_v \frac{\partial \rho_v}{\partial t}+\alpha_v \rho_v \nabla.\left(\vec{v}_v\right)+\alpha_v \vec{v}_v \nabla.\left(\rho_v\right)+\rho_v \vec{v}_v \nabla.\left(\alpha_v\right)=R \quad (8.3)$$

and written as:

$$\rho_v \frac{D \alpha_v}{D t}+\alpha_v \frac{D \rho_v}{D t}+\alpha_v \rho_v \nabla.\left(\vec{v}_v\right)=R \quad (8.4)$$

Similarly for liquid phase with the assumption of constant density, Eq. 8.2 can be written as:

$$\frac{D \alpha_v}{D t}+\left(1-\alpha_v\right) \nabla.\left(\vec{v}_l\right)=\frac{-R}{\rho_l} \quad (8.5)$$

From Eq. 8.5, $\nabla.\left(\vec{v}_l\right)$ is calculated and replaced in Eq. 8.4 assuming a homogeneous flow of liquid-vapor mixture.

$$\rho_v \frac{D \alpha_v}{D t}+\alpha_v \frac{D \rho_v}{D t}+\frac{\alpha_v \rho_v}{1-\alpha_v}\left(-\frac{R}{\rho_l}+\frac{D \alpha_v}{D t}\right)=R \quad (8.6)$$

With further simplification, *m'* can be calculated as:

$$R=\frac{\rho_l \rho_v}{\rho}\left(\frac{D \alpha_v}{D t}+\frac{\alpha_v\left(1-\alpha_v\right)}{\rho_v} \frac{D \rho_v}{D t}\right)=\frac{\rho_l \rho_v}{\rho} \alpha_v\left(1-\alpha_v\right)\left(\frac{D m}{m}\right) \quad (8.7)$$

where *m* and *Dm* are the mass of and the mass transfer rate to a single bubble.